12-2013

Development of Polarization Analysis of Resonant Inelastic X-Ray Scattering

Xuan Gao
Western Michigan University, gaoxuan2631@hotmail.com

DEVELOPMENT OF POLARIZATION ANALYSIS SYSTEM OF RESONANT INELASTIC X-RAY SCATTERING

by

Xuan Gao

A dissertation submitted to the Graduate College
in partial fulfillment of the requirements
for the degree of Doctor of Philosophy
Department of Physics
Western Michigan University
December 2013

Doctoral Committee:

Clement Burns, Ph.D., Chair
Diego Casa, Ph.D.
Arthur Mcgurn, Ph.D.
Lisa Paulius, Ph.D.

DEVELOPMENT OF POLARIZATION ANALYSIS OF RESONANT INELASTIC X-RAY SCATTERING

Xuan Gao, Ph.D.

Western Michigan University, 2013

Resonant inelastic x-ray scattering (RIXS) is a powerful technique in condensed matter physics for studying the electronic excitations in novel materials of interest. In currently operating hard x-ray RIXS instruments the energy and momentum transfers are measured while the outgoing polarization is not measured due to significant technical challenges. But the outgoing polarization of the scattered photons provides valuable information (excitation symmetry) about the states involved in the scattering which is difficult to determine without polarization analysis. Polarization analysis has proved extremely valuable in soft x-ray RIXS, and so a polarization analysis system is being developed to fill the technical void at higher energies.

A polarization analyzer is designed to reflect the scattered photons from the main analyzer by about 90 degrees. At this reflecting angle, the in-plane polarization is naturally eliminated by the polarization factor so that the scattered photons perpendicular to the reflection plane are fully obtained. Therefore it can separate the two orthogonal polarizations (named 'π' and 'σ') by rotating the system by 90 degrees.

The research in this dissertation is about the development of an outgoing

polarization analysis system complementing for the current RIXS instrument at Advanced Photon Source (APS). The polarization analysis system developed includes the x-ray polarization analyzer and the mechanics attached to the RIXS spectrometers and for aligning the polarization analyzer. A variety of diffraction-based polarization analyzers are being developed for different x-ray absorption edges. A polarization analyzer for Cu *K*-edge has been developed, and one for the Ir L_3-edge has also been developed.

By separating the outgoing polarization, the strong polarization dependent electron excitations, e.g. the spin-orbital excitations in iridates can be measured by the polarization analysis system. Further, the system enables us to separate and study the transverse and longitudinal magnons in Sr_2IrO_4, demonstrating a new capability for the RIXS technique.

ACKNOWLEDGMENTS

Pursuing a doctoral degree in the US was an unforgettable journey in my entire life. I wish to dedicate the dissertation to my parents with their love and spiritual support, and especially to my lovely wife, Yangzi Zhu. Without her company, support, love, without her sharing the happiness and sorrow, I could not reach the end and touch my goal. I would like to thank for all she did for me and for my PhD study.

To meet a good advisor is a great gift that one cannot take for granted. I would like to thank my academic advisor, Dr. Clement Burns, for his generous support and advising to my PhD project and dissertation. Thanks for his offering a great opportunity to me to work at the APS in Argonne National Laboratory. There I met Dr. Diego Casa, my onsite advisor, who gave invaluable help and knowledge that I cannot obtain on campus. I also want to thank all the scientists in the inelastic x-ray scattering group at the APS, who are Dr. Thomas Gog, Dr. Ayman Said, Dr. Mary Upton, Dr. Jungho Kim and Dr. Yang Ding, for their valuable help and communications. And I would like to thank all the scientists and technicians who help in various aspects of my dissertation project at the APS.

I would like to thank my dissertation committee, Dr. Arthur McGurn, Dr. Lisa Paulius, for their help and guidance on my PhD dissertation. I am grateful for the all the support from Department of Physics and Western Michigan University that help me complete the PhD degree. I want to thank my friends for sharing the spare time,

my classmates for the help in physics classes, my colleagues that ever help me in my PhD project.

Finally, I would like to share the accomplishment of my dissertation and PhD journey with all the people that I thanked.

Xuan Gao

TABLE OF CONTENTS

Table of Contents - continued

CHAPTER

Table of Contents - continued

CHAPTER

Table of Contents - continued

CHAPTER

LIST OF TABLES

LIST OF FIGURES

CHAPTER 1

INTRODUCTION

The work of this dissertation is divided into three main parts. The first part is the development of an outgoing polarization analysis system for current resonant inelastic x-ray scattering (RIXS) instruments. The calculations and ray tracing simulations are presented for the prototype of the polarization analyzer (PA). A graphite-based PA was designed and tested at the Cu *K*-edge to study the scattered polarization dependence in the superconducting parent cuprates. For the second part, we designed and fabricated a new type of bent single crystal Si PA for the study of strongly spin-orbit coupled and magnetic excitations in iridium based 5*d* transition metal compounds (iridates) at the Ir L_3 absorption edge. Finally, for the third part, studies of excitations in the 2D-layered system Sr_2IrO_4, and the quasi-1D system $BaIrO_3$ are presented.

Development of polarization analysis for RIXS is important because the current RIXS spectrometers measure the changes in energy and momentum of the photons scattered by the sample, but they cannot measure the polarization components of the scattered photons which contain the information of excitation symmetry. By achieving a polarization analysis system, the future RIXS spectrometers can measure all the key factors (energy, momentum and polarization) in the double differential scattering cross-section which relate the initial state to a final state during scattering.

Since the polarization analysis system is developed based on the RIXS spectrometer, in this introductory chapter, a review of inelastic x-ray scattering (IXS)

technique, especially the RIXS technique, is presented and their capabilities. Hereafter, the importance and benefits of polarization analysis are exhibited which impels us to the work of this dissertation.

1.1 Inelastic x-ray scattering

Standard X-ray scattering is an analytical technique which reveals information about the crystal structure and physical properties of materials of interest. In operating x-ray instruments, incident photons incident on the sample are scattered with different angles and energies. The scattered photons are typically measured as a function of incident and scattered angle.

Inelastic x-ray scattering (IXS) is an experimental technique that measures the changes of the momentum and energy between the incident and scattered photons. The momentum and energy transfers during the scattering process provide the crucial information on the excitations of interest. In the typical x-ray scattering process schematically shown in Figure 1.1, the incident beam hits the sample and is scattered in different spatial directions (different q values). The intensity as a function of the frequency change (energy loss) of the scattered beam at a certain q value is measured. The scattered beam spectrum includes the contributions of elastic scattering ($\omega_2 = \omega_1$), energy transferred to the sample ($\omega_2 < \omega_1$), and energy transferred from the sample ($\omega_2 > \omega_1$). We are interested in the spectrum of scattered photons as a function of energy transferred $\hbar(\omega_1 - \omega_2)$ and momentum transferred ($\boldsymbol{q}$) (Plakida, 2003).

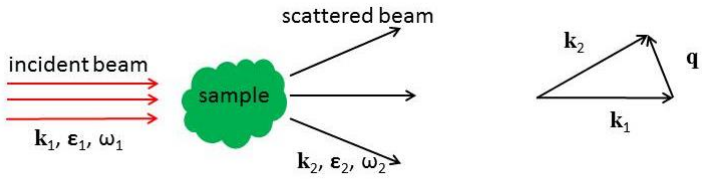

Figure 1.1 X-ray scattering process. $\boldsymbol{k}_1$, ε_1, ω_1 ($\boldsymbol{k}_2$, ε_2, ω_2) are wave vector, polarization, and frequency of the incident (scattered) beam, respectively. Momentum transferred $\boldsymbol{q}$ is defined by $\boldsymbol{q} = \boldsymbol{k}_2 - \boldsymbol{k}_1$.

IXS technique is generally divided into two branches depending on whether the incident photon energy is at a resonance. When the incident energy is off any resonance, this case is called non-resonant inelastic x-ray scattering (NIXS). If the incident energy is close to or at the absorption edge of interest, the scattering is called RIXS.

In RIXS, the Kramers-Heisenberg formula is the key formula for the double differential scattering cross section. But to get into that, first, we need to consider the Hamiltonian that describes the interaction between the incident electromagnetic field and the electrons in the material. Then, by applying the first-order perturbation treatment on the interaction Hamiltonian, the double differential cross section of NIXS can be obtained. Accordingly, in the next section, double differential cross section of RIXS can be derived using the second-order perturbation treatment. The electron Hamiltonian H can be split into two terms, the non-interacting term H_o and the interacting term H_i (Beaurepaire *et al.*, 2010).

$$H = H_o + H_i \tag{1.1}$$

$$H_o = \sum_j \frac{1}{2m} \boldsymbol{p}_j^2 + \sum_{jj'} V(r_{jj'}) \tag{1.2}$$

$$H_i = \sum_j -\frac{e}{mc}\mathbf{A}(\boldsymbol{r}_j)\cdot \boldsymbol{p}_j + \sum_j \frac{e^2}{2mc^2}\mathbf{A}^2(\boldsymbol{r}_j) \tag{1.3}$$

H_o is the sum of the kinetic energy and potential energy of the electrons. H_i expresses the interaction between electrons and electromagnetic field. $\mathbf{A}(\boldsymbol{r})$ is the operator of the vector potential of the electromagnetic wave at the position $\boldsymbol{r}$ of the electron and $\boldsymbol{p}$ is the momentum operator. This treatment omits the spin-dependent contributions since they are smaller by a factor of $\hbar\omega/mc^2$ than the spin-independent ones (Schülke, 2007). In the interaction Hamiltonian, the term that is linear in **A**, needs a second-order perturbation treatment and the term that is quadratic in **A** is appropriate for first-order perturbation calculation. By applying the Fermi Golden rule on the interacting Hamiltonian H_i to the second-order perturbation, the transition probability between the ground state and final state can be obtained,

$$w_{i\to f} = \frac{1}{\hbar}\left|\langle f|H_i|i\rangle + \sum_n \frac{\langle f|H_i|n\rangle\langle n|H_i|i\rangle}{E_n - E_i}\right|^2 \delta(E_f - E_i) \tag{1.4}$$

Since **A** linearly contains the photon creation and annihilation operators, the quadratic term of **A** contains the product of creation operator and annihilation operator, which is suitable for a two-step scattering process. Under the first-order perturbation, substituting H_i by the terms of $\mathbf{A}^2$, the double differential cross section for NIXS is obtained (Rueff *et al.*, 2010),

$$\frac{\mathrm{d}^2\sigma}{\mathrm{d}\Omega\mathrm{d}\omega_2} = \frac{\omega_2}{\omega_1}\left(\frac{e^2}{mc^2}\right)^2(\boldsymbol{\varepsilon}_1\cdot\boldsymbol{\varepsilon}_2^*)^2\sum_{i,f}\left|\langle f|\sum_j \exp(\mathrm{i}\boldsymbol{q}\cdot\boldsymbol{r})|i\rangle\right|^2 \times\delta(E_f - E_i - \hbar\omega) \tag{1.5}$$

where the last sum is usually expressed as the dynamic structure factor S ($\boldsymbol{q}$, ω),

$$
\begin{aligned}
S(\mathbf{q},\omega) &= \sum_{i,f}\left|\langle f|\sum_{j}\exp(i\mathbf{q}\cdot\mathbf{r})|i\rangle\right|^{2}\times\delta(E_f-E_i-\hbar\omega) \\
&= \frac{1}{2\pi}\int_{-\infty}^{\infty} dt\, e^{-i\omega t}\langle i|\sum_{jj'} e^{-i\mathbf{q}\cdot\mathbf{r}_{j'}(t)} e^{i\mathbf{q}\cdot\mathbf{r}_{j}(0)}|i\rangle
\end{aligned}
\tag{1.6}
$$

The dynamic structure factor depends only on the energy and momentum transferred to the system independent of the incident photon energy and wave vector. The dynamic structure factor represents the total scattering from all atomic sites in the solid from the ground state to all the excited final states obeying the conservation of energy and momentum. It is widely used in non-resonant IXS to study phonon excitations.

1.2 Resonant inelastic x-ray scattering

Resonant inelastic x-ray scattering (RIXS) is distinguished from NIXS by its incident energy selection. When tuning the incident photon energy close to an absorption edge of interest, the inelastic signal is significantly enhanced; therefore the atomically selective and weak scattering excitations can be measured at the resonance. The energy and momentum transferred during the scattering are measured to study the nature of intrinsic excitations and to reveal information on the ground state of materials of interest. RIXS is a powerful and unique technique requiring third generation synchrotron radiation sources with high photon intense and high energy resolution and is widely used in various scientific fields.

1.2.1 RIXS double differential cross section

Resonance happens when the incident photon energy is close to or at the energy of the absorption edge of interest. At the resonance, the interaction between

the incident electromagnetic field and the electrons in the material is strongly enhanced. Thus, the term $\mathbf{A}\cdot\boldsymbol{p}$ is dominant in the interacting Hamiltonian H_i. By applying the second-order perturbation to the expression (1.2), in $|\ldots|^2$, the first term (non-resonant part) is negligible compared to the second term (resonant part) when the incident energy $\hbar\omega_1 = E_i - E_n$ (Rueff, 2010). At this condition, the dominator of the resonant term approaches zero and the scattering is dominated and enhanced by the resonant scattering term. Then the famous Kramers-Heisenberg formula (Kramers *et al.*, 1925) at the resonance is the following,

$$\frac{d^2\sigma}{d\Omega d\hbar\omega_2} = r_0^2\left(\frac{\omega_2}{\omega_1}\right)\sum_f \left| \left(\frac{\hbar}{m}\right)\sum_n \frac{\langle f|(\boldsymbol{\varepsilon}_2^* \cdot \boldsymbol{p}_j)e^{-i\mathbf{k}_2\cdot\mathbf{r}_j}|n\rangle\langle n|(\boldsymbol{\varepsilon}_1 \cdot \boldsymbol{p}_{j'})e^{i\mathbf{k}_1\cdot\mathbf{r}_{j'}}|i\rangle}{E_i - E_n + \hbar\omega_1 - i\Gamma_n/2} \right|^2 \times \delta(E_i - E_f + \hbar\omega) \quad (1.7)$$

where $\hbar\omega_1$ and $\hbar\omega_2$ are incident and scattered photon energy which direction of $\boldsymbol{k}_1$ and $\boldsymbol{k}_2$; $|i\rangle$, $|n\rangle$, $|f\rangle$ are the initial, intermediate and final states of the system with energy E_i, E_n, E_f respectively; the sum is over the intermediate and final states; $\boldsymbol{\varepsilon}_1$ and $\boldsymbol{\varepsilon}_2$ are the incident and scattered photon polarizations; Γ_n is the energy broadening of the intermediate state. The formula represents the probability of the scattered photons in the solid angle $d\Omega$ with an energy bandwidth of $d\hbar\omega_2$.

1.2.2 Physical process in RIXS

RIXS can be explained as a two-step process which includes the system absorption of an incoming x-ray and emission of an x-ray by the system. By the absorption of incoming x-rays, an electron in the core level is knocked out into an empty state. The excitation is created by the complex electron interactions between the core hole and valence band which is called the core hole potential. This excitation

typically occurs from an occupied valence state to an unoccupied valence state. Then the core hole is filled by the decay of an electron by the emission of an x-ray. There are two different RIXS processes which are known as direct and indirect RIXS.

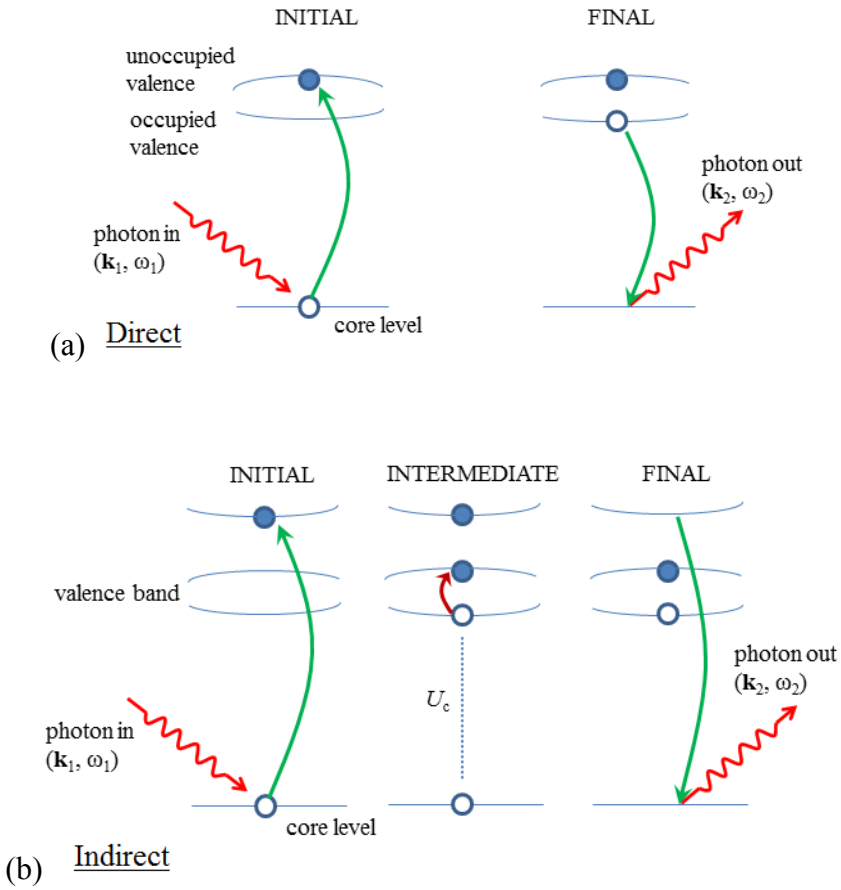

Figure 1.2 (a) Direct RIXS process. An electron is knocked out from a core level into the empty valence band by the incoming x-rays. The core hole is filled by an electron from occupied states by the emission of an x-ray. The excitation occurs in the valence with the change of momentum $\hbar(\boldsymbol{k}_2 - \boldsymbol{k}_1)$ and change of energy $\hbar(\omega_2 - \omega_1)$. (b) Indirect RIXS process. An electron is knocked out from core level into the valence shell by the incoming x-rays. An electron is excited to the empty valence under the Coulomb interaction between core hole and valence electrons. The core hole is filled by the electron decay from valence shell by the emission of an x-ray. The

excitation is created with change of momentum $\hbar(\boldsymbol{k}_2 - \boldsymbol{k}_1)$ and change of energy $\hbar(\omega_2 - \omega_1)$.

Direct RIXS. For direct RIXS, as shown in Figure 1.2a, the electron in the deep-lying core level is excited by the incoming x-ray into an empty valence state. Then an electron in the valence state decays and fills the core hole by the emission of an x-ray. The excitation is the electron transition from the occupied valence band to the empty valence band. This excitation is created with a momentum change $\hbar(\boldsymbol{k}_2 - \boldsymbol{k}_1)$ and an energy change $\hbar(\omega_2 - \omega_1)$. In 5*d* transition-metal (TM) oxide Sr_2IrO_4, the electron is knocked out from 2*p* to 5*d* state by the absorption of incoming x-rays. Then the electron decays from 5*d* to 2*p* core hole. The absorption and emission give direct information of the empty valence state and occupied valence state (Ament *et al.*, 2011a).

Indirect RIXS. A most interesting example is TM Cu *K*-edge RIXS (1*s*→4*p*). In indirect RIXS, as shown in Figure 1.2b, the electron is excited by the incoming x-ray to a valence shell (4*p* state), leaving a core hole in the system. The intermediate state with a core hole creates a strong Coulomb potential with the 3*d* valence electrons, which creates an electron excitation in the valence band. As the electron decays to the core hole (4*p*→1*s*), the system emits an outgoing x-ray, leaving an electron-hole excitation behind. Excitations in indirect RIXS typically suffer from much weaker inelastic signals than the elastic scattering resulting in the difficulty to observe low energy excitations. However, in direct RIXS, e.g. *L*-edge RIXS, since the electron is knocked out directly to the state of the final excitation, a large inelastic signal, sometimes even stronger than the elastic scattering, arises in the spectrum (Ishii *et al.*, 2011a).

RIXS has more strict conditions compared to NIXS. The resonance requires

the incident energy to be the electron transition energy from core level to the specific valence shell on the atomic site of interest. In RIXS experiments, one needs to tune the incident energy to different positions in the fluorescence yield to knock the core electron to different unoccupied states, screening a core-hole potential environment in the immediate state, therefore inducing a certain excitation of interest after the core hole is filled by the electron's decay. However, a NIXS experiment is more straight forward since one can set the incident energy to any value, which is usually chosen to improve energy resolution.

1.2.3 Excitations which can be probed with RIXS

A. Charge transfer excitations

In condensed matter systems, a charge transfer (CT) excitation phenomenon happens when an electron moves from one site to another. In TM oxides, charge transfers were well explained by Hubbard model (Hubbard, 1964). The Hubbard Hamiltonian described the charge transfers as the electron 'hopping integral t' between sites (e.g. from a ligand site to a metal site) and the on-site Coulomb repulsion U. The correlated system can be classified by the relation between t and U, which represents the metallic property and insulating property, respectively. For the half-filled band, if $U/t = 0$ the system is metallic and if $U/t = \infty$, each electron is most likely standing on different site and unfavorable standing on same site, so the electrons are fully localized. Such a system is called Mott insulator. RIXS is a powerful probe to study the several CT features, e.g. electron transfers between ligand state and metal state. The CT is localized or dispersive through lattice and may depend on temperature or pressure, etc. The metal-insulator boundary was

theoretically classified described in (Zaanen *et al.*, 1985). The CT excitations in manganites (Grenier *et al.*, 2005; Weber *et al.*, 2010) and in nickelates and cuprates (Wakimoto *et al.*, 2009) have been studied by metal *K*-edge RIXS at the APS.

B. Orbital excitations

RIXS is currently in wide use to understand the valence electrons properties in many strong correlated systems. The orbital degree of freedom which is coupled to the other (charge, spin) degrees of freedom is one of the most interesting subjects to understand the natures of the solid. The orbital levels of an ion of interest are split to different energy levels in the crystal field produced by the surrounding charge distribution (anion neighbors). For example, in TM cuprates, there are five-fold degenerate *d*-orbitals. These orbitals are d_z^2 and $d_{x^2-y^2}$ orbitals in the higher energy levels and d_{xy}, d_{xz} and d_{yz} orbitals in lower energy. The electron transitions between different *d* orbitals are called *d-d* transitions. *d-d* transitions in many correlated systems had been studied by RIXS to understand the orbital ground states in the crystal field. There is another orbital excitation called orbitons or orbital waves dispersing through the crystal lattice which differ from the local *d-d* transition. *d-d* orbital excitations in NiO (Huotari *et al.*, 2008), and cuprates (Kim *et al.*, 2004b) have been studied by direct RIXS. The orbiton was predicted as one quasi-particle that behaves similar to the holon and spinon. The observation of dispersing orbital excitations is a hot topic (Saitoh *et al.*, 2001; Tokura *et al.*, 2000). RIXS contributes to measuring the orbitons since it is sensitive to the dipole forbidden *d-d* excitations and has momentum capture through the Brillouin zone (Ament *et al.*, 2011b).

C. Magnetic excitations-magnons

Recently, RIXS has shown the ability to study the magnetic excitations in transition metal oxides (TMO), especially the ability of *L*-edge RIXS to probe the single magnon excitations, which the *K*-edge RIXS cannot probe due to the selection rules. Magnetic excitations have been studied by RIXS in the soft x-ray region. For example, the magnetic excitations in one dimensional system $Sr_{14}Cu_{24}O_{41}$ at the Cu L_3-edge (Schlappa *et al.*, 2009), single magnon in two dimensional La_2CuO_4 at the Cu *L*-edge (Braicovich *et al.*, 2010a), and magnon dispersion in 2D antiferromagnetic insulator $Sr_2CuO_2Cl_2$ (SCOC)(Guarise *et al.*, 2010). Magnon excitation is a collective excitation phenomenon related to the superposition of electrons' 'spin-flip' at equivalent sites, carrying a fixed amount of energy and lattice momentum in the crystal lattice. The 5*d* elements, such as Ir, are attracting attention with its interesting features. Unlike the 3*d* TMO that has a strong Coulomb interaction and narrow *d*-band, the 5*d* orbitals are extended in space with very weak Coulomb interaction but it is a Mott insulating ground state system due to the strong spin-orbital coupling. For example, the 2D layered 5d system, Sr_2IrO_4, is believed to be described by a $J_{eff} = 1/2$ ground state. The strong spin-orbital coupling splits the t_{2g} state to the $J_{eff} = 3/2$ quartet with lower energy and a singly occupied $J_{eff} = 1/2$ doublet near the Fermi level, driving the system into a Mott insulating ground state instead of a metallic state. In the direct RIXS process, e.g. *L*-edge RIXS, the single spin-flip (~200 meV) occurs when the electron is excited from $2p \rightarrow 3d$ due to the strong spin-orbital coupling (Ishii *et al.*, 2011c; Kim *et al.*, 2012b). However, in the indirect RIXS process, e.g. *K*-edge RIXS ($1s \rightarrow 4p$), two-magnon excitations ($\Delta S_z = 0$) are allowed by both experimental observation and theoretically understanding (Brink, 2007).

1.3 RIXS instrumentation

RIXS spectrometer is operating with the high flux and the resolution incident energy tuned to the absorption edge of an atom of interest, which can enhance certain excitations during the scattering event. Scattered photons with various energies from the sample are analyzed by the analyzer at a certain momentum transfer angle that related to the reciprocal lattice space of the solid. Information of energy and momentum transferred are measured.

In the first part of the project, a polarization analysis system based on HOPG graphite-based was developed and tested at 30-ID based on MERIX instrument. For the second part of the project, a bent Si PA and its control system was being developed at 9-ID where the rotation of the polarization of incident photons had been achieved by the insertion of diamond phase plate (Lang *et al.*, 1995). With the outgoing polarization analysis system, 9-ID will be the first RIXS beamline in the world which can measure both incident and scattered polarization.

The project of this thesis is carried out at the Advanced Photon Source (APS), Argonne National Lab shown Figure 1.3. The IXS technique is allocated at three sectors, 3-ID, 9-ID, and 30-ID according to different experimental requirements. The medium energy resolution resonant IXS (MERIX) and high energy resolution resonant IXS (HERIX) are located at 30-ID to study a wide variety of complex materials. MERIX is a RIXS instrument with overall energy resolution of ~30−600 meV depending on the x-ray monochromators and analyzer used in the experiment. HERIX is a NIXS instrument with extremely high energy resolution (1~3 meV) and large Rowland circle diameter (9 m), taking the duty of doing the phonon related experiments in solids and liquids. A similar type of instrument as MERIX is at 9-ID for doing medium energy resolution RIXS experiment. 3-ID includes the nuclear

resonant scattering and does 2.6 meV resolution measurements.

Figure 1.3 Advanced Photon Source, Argonne National Lab, IL, USA. This is a high-brilliance synchrotron radiation light source. High speed electrons are injected into a 1.1km circumference storage ring. On the tangent direction, the storage ring is divided by 35 beamlines for a variety of x-ray techniques and scientific fields.

The mechanics of the graphite-based polarization analysis system were designed based on the MERIX instrument and the outgoing polarization analyzed RIXS data of $CuGeO_3$ was carried out there as well. Then a modified system with bent Si PA was developed based on the instrument at 9ID. As an example of RIXS instrument, a detail description of instrument at 9ID from upstream to downstream is presented Figure 1.4.

Undulator. 9ID is an undulator insertion device beamline. Electrons in the storage ring are propagating tangentially into the undulator, which is a series set of magnets with antiparallel magnetic fields so that it forces the electrons to oscillate in many small periods. At each oscillation x-ray are emitted and added up coherently in

from the beginning to the end of the undulator. Therefore, the radiation contribution generates a very intense beam with a small divergence and a horizontally linear polarization (Jens Als-Nielsen, 2001). Brilliance is an important quality of x-ray which is defined as photons/s/mm^2/mrad^2/0.1%bandwith. Undulator devices are widely used in third-generation synchrotron radiation sources and a factor of ~10^{12} brighter that the early lab sources.

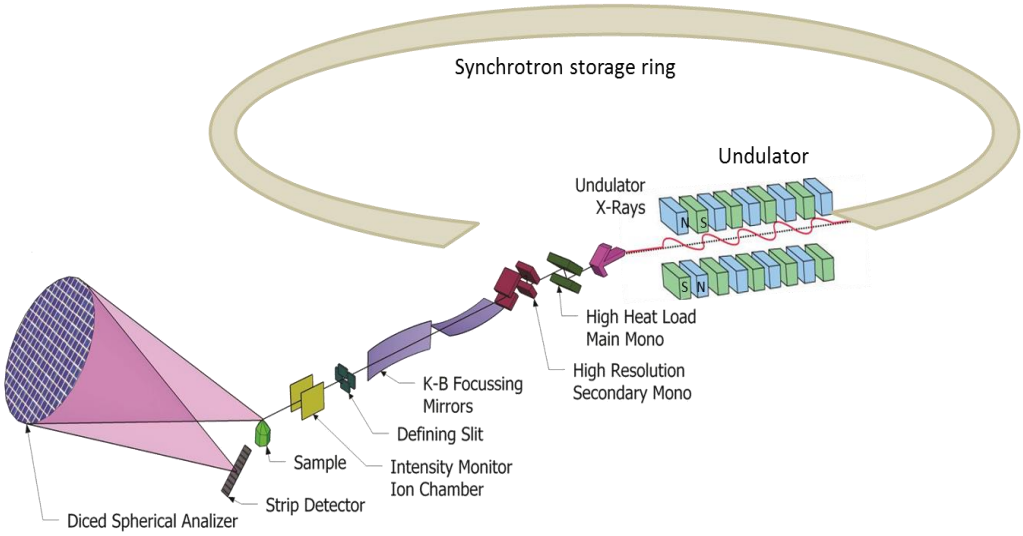

Figure 1.4 Schematic of RIXS beamline at 9ID-B, APS. From the upstream to down-stream is the undulator, first and second monochromator, focusing mirrors, sample, analyzer and detector.

Monochromators. The monochromator of hard-x ray is the first optics at the upstream of the beamline to choose the reference working energy and energy bandwith of the incident photon. It is typically a set of flat perfect crystals (e.g. Si, Ge) with a two- or four-bounce geometry, which diffracts the x-ray following the famous Bragg Law, given by:

$$n\lambda = 2d \cdot \sin\theta \tag{1.8}$$

where λ is the wavelength of the incident photon, d is the lattice spacing of the diffraction plane respect to the certain Bragg reflection, and θ is the angle between incident beam and diffraction plane, n is an integer. Differentiating the Bragg Law, the relation between the energy resolution after the diffraction and so-called rocking curve width (in rad) can be derived:

$$\frac{\Delta E}{E} = \frac{\Delta\lambda}{\lambda} = -\cot\theta \cdot \Delta\theta \tag{1.9}$$

For an ideal source, Δθ is an intrinsic factor, depending on the crystal quality, crystal structure, and the Bragg reflection index. In practice, it needs to be combined with the real source features at APS, such as beam divergence and bandwidth. In 9ID as shown in Figure 1.4, high intense polarized x-rays are produced by a periodic undulator followed by a cryogenically cooled Si (111) crystals (first monochromator) and a four-bounce high-resolution monochromator. A set of K-B focusing mirrors focus the beam to the sample position with a small beam size.

Analyzer. The analyzer for RIXS experiments is for analyzing the energies in scattered photons from the sample at a certain 2θ angle with respect to the beam. The sample, analyzer, and detector are on the so-called "Rowland circle" geometry. Rowland circle is the circle tangent to the analyzer whose radius of curvature is half of the bending radius of the analyzer, which the divergent source (sample), center of analyzer and focus are all located on. The RIXS experiments require an incident energy fixed at the resonance to enhance certain excitations in solids. The analyzer is a spherical diced bent crystal working at near-backing scattering configuration, collecting and focusing the scattered photons to an one dimensional strip detector

(Huotari *et al.*, 2006). Each pixel of the analyzer can be treated approximately as an unstrained perfect flat crystal. Based on the Bragg law, scattered photons from the sample with different energies are separated by their different incident and outgoing angles on the analyzer crystals and geometrically illuminated on different channels on the detector. The energy resolution from the analyzer depends on Eq. 1.9 as well. The total energy resolution can be expressed approximately as the square sum of incident bandwidth ΔE_{in} from the first and second monochromator, intrinsic analyzer resolution ΔE_{an}, and geometry factor ΔE_{ge}. ΔE_{ge} is the called geometry term, affected by the spatial geometry contributions from the sample and detector, which depends on the foot print on the sample and pixel size of the detector (Gog *et al.*, 2012). The total energy resolution ΔE_{tot} is:

$$\Delta E_{tot} = \sqrt{\Delta E_{in}^2 + \Delta E_{an}^2 + \Delta E_{ge}^2} \tag{1.10}$$

A series of options for first and second monochromator, analyzers respect to the absorption edge of an element can be found at the Sec 30 website with their energy and angular resolutions theoretically (Gog *et al.*, 2012). The polarization analyzer is a complement additional analysis component which is placed after the focus of the energy analyzer as a secondary analyzing and focusing optics. More detail of polarization analyzer will be introduced in latter sections.

1.4 Energy and momentum dependence in RIXS

1.4.1 Energy dependence

The incident energy dependence is the most important fact in the RIXS experiment. Based on the resonant cross-section, the intensities of energy loss, often

called inelastic peaks, are enhanced when the incident energy is tuned to the vicinity of a certain absorption edge. Different excitation is emphasized for different incident energy region at the x-ray absorption spectrum (XAS), which depends on the energy level that the core electron is excited into and the intermediate state under electron-core hole interaction.

In RIXS experiment, one chose a fixed incident energy that enhances the inelastic peak of interest, and then scans the emission radiation from the sample to obtain the relative emitted energy spectrum. For example, at *K*-edge RIXS, at the pre-edge region, the core electron is directly excited into a 3d state, which is the case of *d*-*d* excitations are assigned. And at the resonant edge, the excitations are usually dominated by the charge-transfer (CT) excitations. At the region beyond the absorption edge, for example of Cu *K*-edge RIXS for $CuGeO_3$ shown in Figure 1.5, the inelastic peaks at ~7 eV are dominated by the CT excitations which do not appear at lower incident energies. The 2 eV elastic peak appears when the incident energy is at pre-edge region.

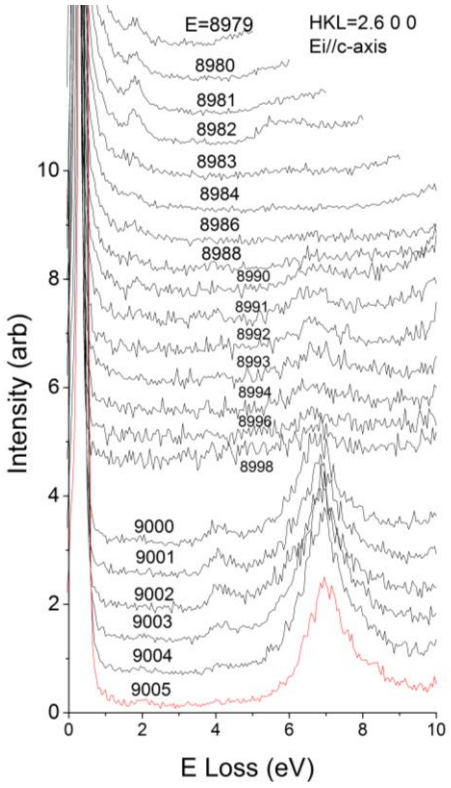

Figure 1.5 Cu *K*-edge RIXS data set of $CuGeO_3$ for different incident energies.

1.4.2 Momentum dependence

The cross section of RIXS also shows the momentum transfer dependence of the electronic excitations. RIXS measurement can be utilized to probe the different positions within any one Brillouin zone since the momentum can be always reduced to the first Brillouin zone by the periodical feature. Sometimes RIXS experiments are measured at high reciprocal vectors in the horizontal geometry configuration, tuning the angle between the in-plane polarizations of reflected and incident beam to nearly 90°, largely reducing the huge elastic line to detect the low energy loss features, such as magnons. An example of *K*-edge RIXS of 1D cuprates in the Figure 1.6 shows the

dispersive feature between 2 ~ 4 eV interpreted to be in the form of spinons and holons, and the non-dispersive is assigned to be the CT excitation. RIXS as a powerful technique shows its wide use and can that it can probe the momentum within the entire Brillouin zone, which is an advantage compared to the small momentum transferred by optical measurements ($q \approx 0$).

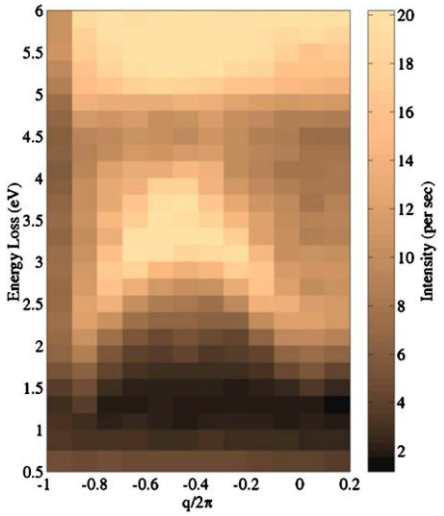

Figure 1.6 Image plot of Cu *K*-edge RIXS of $SrCuO_2$, as a function of momentum and energy transfer. 3.5 eV peak disperses in the entire Brillouin zone and is interpreted as a charge density wave. Non-dispersive feature ~6eV is attributed to a local CT excitation (Kim *et al.*, 2004a).

1.5 Polarization in RIXS

1.5.1 Polarization of scattered photon

X-ray is a transverse electromagnetic wave that can be either linear polarized (the electric field oriented in one direction, perpendicular to the propagating

direction), circular polarized (the electric field rotates as time changes) or elliptically polarized (the combination of linear and circular polarization). The polarization can be therefore determined by three parameters (P_1, P_2, P_3) called Stokes-Poincaré parameters (Shen *et al.*, 1993), which are related to (σ and π) linear polarization, ± 45°-tilted linear polarization, and the left- and right-hand circular polarization, respectively. If the beam is 100% polarized, the relation between the Poincaré-Stokes parameters is $\sqrt{P_1^2 + P_2^2 + P_3^2} = 1$. As shown in Figure 1.7, linear polarization has two orthogonal components (ε_1 and ε_2) propagating in phase (phase difference is zero) and the amplitude ratio remains constant, so that the total vector is a line projection on the polarization plane. By contrast, the circular polarization always have the two components with a phase difference of $\pi/2$ but the two component have same amplitude, so that the projection is a circle on the polarization plane.

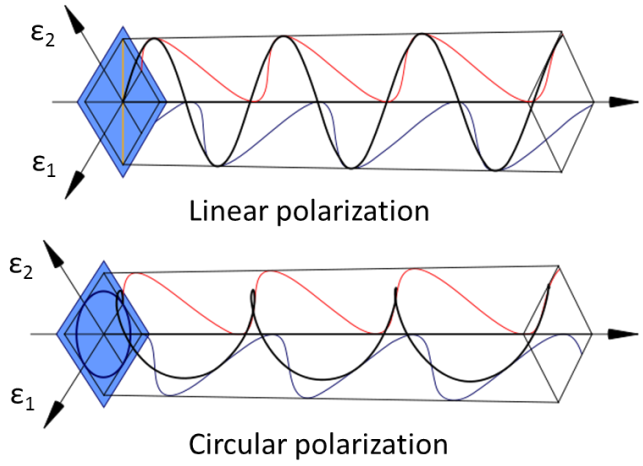

Figure 1.7 Linear and circular polarized beam propagation. Two orthogonal components oscillate separately in the color of red and blue. The black wave is the combination of the two components. Linear polarization has a projection of a straight line; circular polarization has a circle projection.

The electric field of a plane wave with a wave vector $\boldsymbol{k}$ and energy $\hbar\omega$ can be written

as the form of:

$$\boldsymbol{E}(\boldsymbol{r},\mathrm{t}) = \begin{pmatrix} \mathrm{a}_1 \cdot \cos(\boldsymbol{k}\mathrm{z} - \omega t) \\ \mathrm{a}_2 \cdot \cos(\boldsymbol{k}\mathrm{z} - \omega t + \varphi) \\ 0 \end{pmatrix} \tag{1.11}$$

a_1 and a_2 are the amplitude of two components in $\boldsymbol{\varepsilon}_1$ and $\boldsymbol{\varepsilon}_2$ direction, respectively. φ is the relative phase difference between them. The amplitude and phase information can be conveniently represented by the Jones vector,

$$\boldsymbol{A} = \begin{bmatrix} A_1 \\ A_2 \end{bmatrix} = \begin{bmatrix} a_1 \cdot e^{i\theta_1} \\ a_2 \cdot e^{i\theta_2} \end{bmatrix} \tag{1.12}$$

A polarization ellipse shown in Figure 1.8 describes the projection of the electric field on the plane perpendicular to the wave propagation direction as time passes.

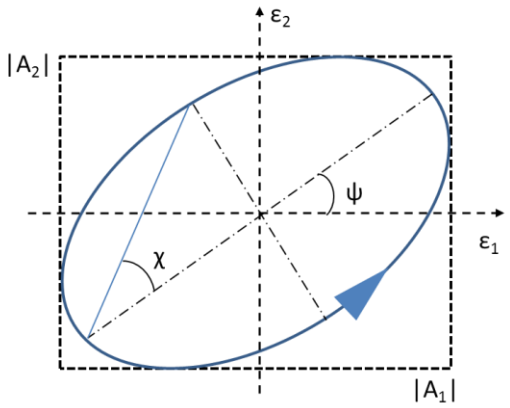

Figure 1.8 The polarization ellipse of an elliptical beam, combining the linear polarization and circular polarization. The counterclockwise is the positive P_3 direction when looking into the source (Detlefs et al., 2012).

The Poincaré-Stokes vector **P** (P_1, P_2, P_3) is defined as (Blume *et al.*, 1988; Detlefs *et al.*, 2012):

$$P_1 = \frac{|A_1|^2 - |A_2|^2}{|A_1|^2 + |A_2|^2} = \cos(2\psi)\cos(2\chi)$$

$$P_2 = \frac{|A_1 + A_2|^2 - \|A_1 - A_2\|^2}{2(|A_1|^2 + |A_2|^2)} = \sin(2\psi)\cos(2\chi) \qquad (1.13)$$

$$P_3 = \frac{|A_1 - iA_2|^2 - |A_1 + iA_2|^2}{2(|A_1|^2 + |A_2|^2)} = \sin(2\chi)$$

There are several special polarization cases:

(1) When the beam is circular polarized, $a_1 = a_2$, and $\chi = \pm\ 45°$, corresponds the relative phase difference $\phi = \theta_2 - \theta_1 = \pm 90°$. Therefore $P_3 = 1$ (left-handed circular polarization) or $P_3 = -1$ (right-handed circular polarization).

(2) When the beam is linearly polarized, the ellipticity χ is zero, so the circular portion $P_3 = 0$; $P_1 \neq 0$, $P_2 \neq 0$, so that the beam is oriented at arbitrary direction.

(3) If the beam is linear polarized, and the polarization is along the horizontal direction ($\boldsymbol{\varepsilon}_1$), $\psi = 0$; then $P_1 = 1$, and $P_2 = P_3 = 0$; this polarization is called σ-polarization.

(4) When the linear polarization is along vertical direction ($\boldsymbol{\varepsilon}_2$), $\psi = 90°$; then $P_1 = -1$, and $P_2 = P_3 = 0$; this polarization is called π-polarization.

The polarization analyzer is a crystal to analyze the polarization components (σ and π) in the scattered photons from the real sample. Here σ is the polarization

perpendicular to the scattering plane of the polarization analyzer and π is the polarization within the scattering plane as shown in Figure 1.9.

Kinematically, the intensity of a Bragg diffraction of a linear polarized is (Shen *et al.*, 1993):

$$I(\chi) = \frac{I_0}{2}\left[\left(1+\cos^2 2\theta\right)+\sin^2 2\theta\cdot\left(\mathrm{P}_1\cos 2\chi+\mathrm{P}_2\sin 2\chi\right)\right] \qquad (1.14)$$

where the I_0 is the incident intensity; θ is an arbitrary Bragg angle of the diffraction of reflector; χ is the angle between the normal of the diffraction plane and the incident σ polarization as the reference. P_1 and P_2 are given by:

$$\mathrm{P}_1 = \frac{1+\cos^2 2\theta}{\sin^2 2\theta}\cdot\frac{I(0°)-I(90°)}{I(0°)+I(90°)}$$

$$\mathrm{P}_2 = \frac{1+\cos^2 2\theta}{\sin^2 2\theta}\cdot\frac{I(45°)-I(-45°)}{I(45°)+I(-45°)} \qquad (1.15)$$

They can be obtained by measuring the intensities in different scattering planes of the polarization analyzer with a nonzero Bragg angle θ. The linear (σ, π) polarization parameter P_1 can be obtained by the measurement of scattered intensities on the vertical and horizontal plane and P_2 can be obtained by measuring the intensities at the plane respect to incident σ polarization to $\pm 45°$. In practices, the normalization of I(0°) (I(45°)) to I(90°)(I(−45°)) is necessary to cancel to signal to noise ratio and the overall reflectivity of the polarization analyzer.

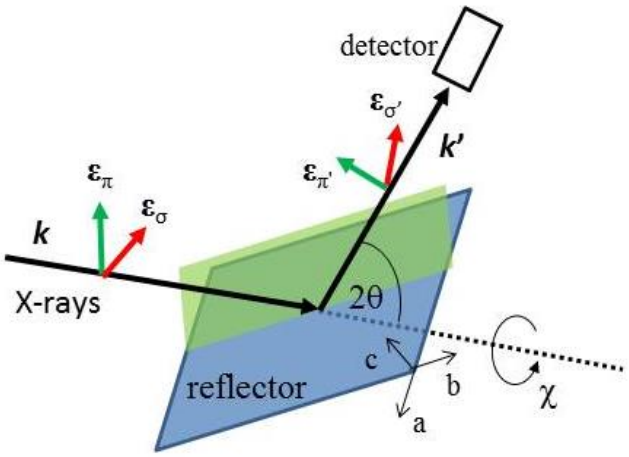

Figure 1.9 Incident polarization and scattered polarization with respect to the reflector (polarization analyzer crystal). Here the incident x-rays (with ***k*** vector) are related to the polarization analyzer diffraction process, but these are the scattered photons from the real sample.

The intensity of $I(\chi)$ reveals the crucial point of the scattered polarization analysis. When the incident x-rays respective to the polarization analyzer crystal is pure σ polarization, ($P_1 = 1$, $P_2 = P_3 = 0$) and the diffraction plane is vertical, $\chi = 0$, the intensity detected is always a constant and independent on the scattering angle 2θ, given by (only consider polarization effect on the scattering intensity and ignore the dynamic process of scattering):

$$I = \frac{I_0}{2}\left[\left(1+\cos^2 2\theta\right)+\sin^2 2\theta\right] = I_0 \tag{1.16}$$

If the incident x-rays respective to the polarization analyzer crystal are pure π polarization, ($P_1 = -1$, $P_2 = P_3 = 0$) and the diffraction plane is vertical, the intensity is:

$$I = \frac{I_0}{2}\left[\left(1+\cos^2 2\theta\right)-\sin^2 2\theta\right] = I_0 \cos^2 2\theta \tag{1.17}$$

The term of $\cos^2 2\theta$ is called polarization factor for the in-plane polarization. This is

the reason that polarization analyzer is ideally designed to have $2\theta = 90°$ ($\cos^2 2\theta = 0$) to eliminate the in-plane π polarization and fully preserve out of plane σ polarization, therefore, separate the two orthogonal components in the scattered photons from the sample. One also can eliminate the π polarization and preserve σ polarization by rotating the diffraction plane of polarization analyzer to $\chi = 90°$. This polarization separation in the scattered photons can help improve the signal-noise ratio which many experiments usually suffer during the data collection. This is especially helpful for the study of the low energy excitations in RIXS. For instance, for the magnetic scattering in π polarization channel, after the diffraction of polarization analyzer, the σ polarization channel signal (Thomson scattering or elastic line remains) is largely reduced nearly to zero, then the low energy inelastic peaks 'survive' from the tail of elastic peak. Multiple inelastic peaks with close energy loss positions overlap to show one broad peak. If they are in different polarization directions, they can be distinguished by polarization analysis.

The scattering angle 2θ may not be $90°$ exactly, only approximately, since the selection of a desired d-spacing of polarization analyzer crystal that satisfies the Bragg condition for $90°$ with the energy at a certain absorption edge does not always exist. This increases the difficulty of developing the polarization analyzers. Polarization analyzers made by different crystals will work for different resonances, similar to the conventional energy analyzer in RIXS. One needs to consider the channel leakage related to the Bragg angle to the polarization when processing the polarization analyzed data, especially when the analyzer is removed from $90°$.

1.5.2 Importance of polarization dependence in RIXS

The polarization dependence is one of the most important factors in the RIXS

technique as can be seen in the RIXS cross section Eq.(1.7). RIXS is a second-order process where the selection rules involve both polarizations of incident and scattered photons. The incident and scattered polarization are compared to the orientation of the sample and provide valuable symmetry information of the excitation states involved during the scattering. The polarization of the incident photons is in the plane of the synchrotron radiation ring and perpendicular to the propagation direction which is often called "σ" polarization. RIXS experiments are favorably performed in horizontal scattering geometry so that the intense elastic scattering can be largely reduced by the polarization factor $\cos^2(2\theta)$, when the scattering angle between incident and outgoing beam 2θ is close to 90° shown in Figure 1.10, which helps to measure the low energy excitation closed to the elastic line.

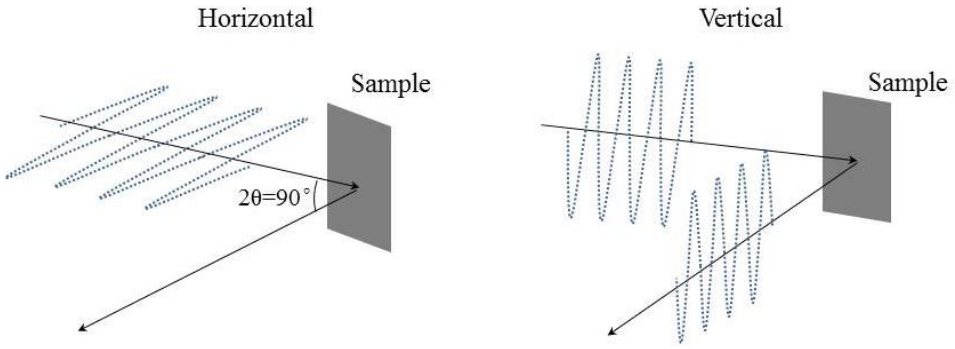

Figure 1.10 Horizontal geometry and vertical geometry with different polarization of incident beam respect to the scattering plane. In the horizontal geometry, incident polarization and outgoing polarization are near perpendicular to largely reduce the elastic scattering from the sample.

Rotating the incident polarization relative to sample orientation can be performed by using the phase retarder (Lang *et al*., 1995) or by rotating the crystal itself. In current experiments, there is no setup for the measurements of this

polarization. Therefore, a polarization analysis of the scattered photons is required to a complete determination of excitation symmetry for both technical and scientific point of view (Gog *et al.*, 2009), which is the work of this dissertation.

The symmetry selectivity strongly related to scattered polarization dependence had been discussed by (Schülke, 2007) in the square matrix element between the intermediate state and final state:

$$\left|M_{\mathrm{n,f}}\right| = \left|\sum_{\mathrm{j}} \left\langle f \left| \boldsymbol{e}_2 \cdot \frac{\boldsymbol{p}_{\mathrm{j}}}{\hbar} \cdot \mathrm{e}^{-i\boldsymbol{k}_2 \cdot \boldsymbol{r}_{\mathrm{j}}} \right| n \right\rangle \right|^2 \tag{1.18}$$

which can be treated by dipole one-electron system approximation:

$$\left|M_{\mathrm{n,f}}\right| \sim \left|\sum_{\mathrm{j}} \left\langle f \left| \boldsymbol{e}_2 \cdot \boldsymbol{r} \right| n \right\rangle \right|^2 \sim \boldsymbol{e} \cdot \mathbf{T} \cdot \boldsymbol{e} \tag{1.19}$$

with a tensor **T** , $\mathbf{e}_2$ is the scattered polarization vector with respect to the principle crystal axes, $|n\rangle$ ($|f\rangle$) is the intermediate state (final state). The tensor **T** can be written in the diagonal matrix elements by the principle coordinate:

$$\mathrm{T}_{\eta} = \left|\left\langle f \left| \eta \right| n \right\rangle\right|^2 \tag{1.20}$$

where η = x, y, z are the coordinates of the principle axes of the tensor. The principle square matrix element is determined by the tensor component and scattered polarization vector. Therefore by scattered polarization analysis one can assign the excitation nature by the symmetry arguments qualitatively to avoid the complexity of solving the theoretical models.

1.5.3 Polarization dependence of orbital excitations

As a good example of polarization analysis, the orbital excitation in Cu-K

edge of $KCuF_3$ by RIXS had been studied by polarization analysis on the scattered photons (Ishii *et al.*, 2011b). This is currently the only work of hard RIXS with polarization analysis. But the broad energy resolution (~600 meV) and the low efficiency of the flat graphite necessitated long integration times. A more efficient analyzer concept is needed to enable widespread usage. $KCuF_3$ has cubic symmetry with hole orbitals $3d_{y^2-z^2}$ and $3d_{y^2-z^2}$ (e_g state) on neighboring Cu sites. The *d-d* excitation which is the transition between 3*d* orbitals can be the transition between two-fold e_g orbitals (e_g excitation) or from the three-fold t_{2g} orbital to e_g orbital (t_{2g} excitation). With the outgoing polarization analysis the e_g excitation is distinguished from t_{2g} excitation by the symmetry arguments. The selection rules for RIXS can be expressed as the product representation $\Gamma_i \times \Gamma_j \times \xi_i \times \xi_j$, where Γ_i, Γ_j are initial and final state, ξ_i , ξ_j are incident and outgoing polarization. The possible excitation occurs if the product representation $\Gamma_i \times \xi_i \times \xi_j$ contains the same symmetry as the final state Γ_j.

$KCuF_3$ sample has D_{4h} group symmetry. The symmetry determined by the polarization configuration shows the possible symmetry of the excitation. e_g excitation requires the B_{1g} symmetry which only appears on the (a), (b) ,(d) configuration only at $\pi \rightarrow \pi$' channel. To compare the experimental results in Figure 1.11, t_{2g} excitation shows up in (c) configuration on both π' and σ' channels, so the spectrums in both channels are almost identical, and the e_g excitation is symmetry forbidden. In the other three polarization configurations both e_g and t_{2g} excitations contribute to the spectrum in both scattered polarization channels. By analyzing the spectrum weight, the e_g excitation is distinguished from the t_{2g} excitation at the energy about 1eV instead of 1.3eV.

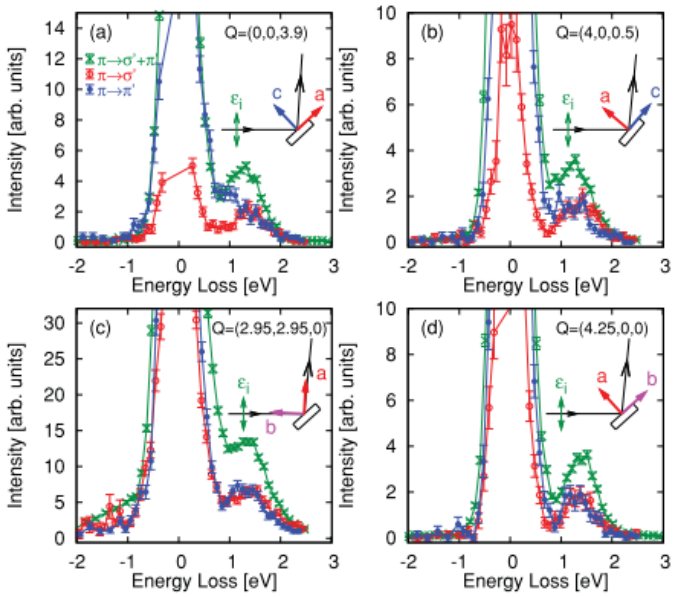

Figure 1.11 Polarization analyzed RIXS spectra of $KCuF_3$. (Ishii *et al.*, 2011b)

The polarization analyzed spectra are obtained from a flat graphite polarization analyzer with a low overall efficiency, which is largely reduced by ratio of the mosaic of the graphite crystal and the divergence of scattered photon from the main energy analyzer. We had developed a graphite polarization analyzer with a curved surface for Cu *K*-edge RIXS with a reasonable efficiency and energy resolution, which will be introduced in a later chapter.

1.5.4 Polarization in magnetic excitations

RIXS has recently shown its ability to study the magnetic excitations. Some experiments have shown good results with dispersing magnetic excitations at Cu L_3-edge (Braicovich *et al.*, 2010b; Schlappa *et al.*, 2009) and Ir L_3-edge (Kim *et al.*, 2012a; Kim *et al.*, 2012b). The magnetic excitations in *L*-edge RIXS are easier to detect with about two orders of magnitude stronger signal than *K*-edge RIXS due to

the direct projection of the core electron to the *d*-state rather than the indirect process of *K*-edge RIXS. X-ray carries only angular momentum L, unlike neutrons that carry magnetic spin half to directly produce the spin-flip excitations. The magnetic excitations in RIXS, therefore, are the spin-flips due to the strong interaction between the spin and orbital (spin-orbital coupling) with presence of the core-hole state. With strong spin-orbital coupling, the total angular momentum is now the good quantum number instead of spin and orbit angular momentum themself. Photons can transfer $\Delta L = 0, 1, 2$ to the system which will cause the single magnon excitation with $\Delta S=1$ or two-magnon with $\Delta S=2$ under conservation of the total angular momentum (Ament *et al.*, 2011b).

A fast collision approximation made by Luo (Luo *et al.*, 1993) to express the magnetic scattering when the lifetime of core electron excited in the system and decay to the core level leaving a excited state is fast and can be neglected. The cross section of RIXS for magnetic excitations can be expressed by factoring the low-energy effective scattering operator that includes the creation and annihilation of the core hole, leaving the system in a low-energy excited state. The effective low-energy operator represents the magnetic excitation with a strong transferred momentum and incident and scattered polarization dependence (Haverkort, 2010). The effective scattering operator given by(van Veenendaal, 2006) that is an exact form for magnetic excitation in RIXS:

$$\begin{aligned} \mathrm{R}_{\omega_i,j}^{\varepsilon_i \varepsilon_o} &= \sigma^{(0)} \varepsilon_{\mathrm{i}} \cdot \varepsilon_{\mathrm{o}}^{*} + \frac{\sigma^{(1)}}{s} \varepsilon_{\mathrm{o}}^{*} \times \varepsilon_{\mathrm{i}} \cdot S_j + \\ &\frac{\sigma^{(2)}}{s(2s-1)} \times \left(\varepsilon_{\mathrm{i}} \cdot S_j \varepsilon_{\mathrm{o}}^{*} \cdot S_j + \varepsilon_{\mathrm{o}}^{*} \cdot S_j \varepsilon_{\mathrm{i}} \cdot S_j - \frac{2}{3} \varepsilon_{\mathrm{i}} \cdot \varepsilon_{\mathrm{o}}^{*} \cdot S_j^{2} \right) \end{aligned} \tag{1.21}$$

Where the S_j is the spin operator at site j, with the expectation value s. $\sigma^{(0)}$, $\sigma^{(1)}$, $\sigma^{(2)}$is

the isotropic, magnetic circular dichroic and magnetic linear dichroic spectral functions. ε_i and ε_o are the incident polarization and outgoing polarization. To clarify the polarization dependence of the incident and outgoing polarization, the scattering operator for spin 1/2, tetragonal, D_{4h} point group system can be written as form of 3 × 3 tensor and polarization vectors:

$$\mathrm{R}_{\omega_i,j}^{\varepsilon_i \varepsilon_o} = \varepsilon_{\mathrm{o}}^{*} \cdot \begin{pmatrix} \sigma_{\mathrm{a}_{\mathrm{B_{1g}}}}^{(0)} & 2S_z\sigma_{\mathrm{a}_{\mathrm{2u}}}^{(1)} & -2S_y\sigma_{\mathrm{e_u}}^{(1)} \\ -2S_z\sigma_{\mathrm{a}_{\mathrm{2u}}}^{(1)} & \sigma_{\mathrm{a}_{\mathrm{B_{1g}}}}^{(0)} & 2S_x\sigma_{\mathrm{e_u}}^{(1)} \\ 2S_y\sigma_{\mathrm{e_u}}^{(1)} & -2S_x\sigma_{\mathrm{e_u}}^{(1)} & \sigma_{\mathrm{a}_{\mathrm{A_{1g}}}}^{(0)} \end{pmatrix} \cdot \varepsilon_{\mathrm{i}} \qquad (1.22)$$

Magnon dispersions for several systems with different crystal structures has calculated theoretically (van Veenendaal, 2006). In practice, the symmetry arguments to the transition operator cannot be made completely if there is missing information of the scattered polarization vectors. Utilizing a polarization analysis system, magnetic excitation components in different polarization channels can be separated, so the transverse and longitudinal magnon wave related to exact spin-flip directions can be detected which has not been studied experimentally. The polarization analysis system developed for studying the magnetic excitations in iridates at Ir L_3-edge will be introduced later in this thesis.

CHAPTER 2

DESIGN OF GRAPHITE-BASED POLARIZATION ANALYZER

The energy analyzer is an important part of the RIXS instruments that has been introduced in the previous chapter. In this chapter a secondary crystal analyzer whose function is to analyze the outgoing polarization is presented. We name the conventional energy analyzer and the secondary analyzer as "main analyzer" and "polarization analyzer (PA)", respectively. The main analyzers of RIXS are made by perfect crystals wafers (e.g. Ge or Si) diced and then spherically bent (Huotari *et al.*, 2006). The main analyzer, sample and detector are all placed on the Rowland circle as shown in Figure 2.1a, working at the near-back scattering conditions (Bragg angle is near 90°) to achieve the best energy resolution. The crystal wafer is diced to small perfect crystals to effectively eliminate the strain which broadens the intrinsic resolution (Collart *et al.*, 2005). The bending radius of main analyzer equals the diameter of the Rowland circle which is typically called Johann geometry. The PA is an additional optic added to the current RIXS spectrometers to obtain the polarization information of outgoing photons. The PA is designed to diffract the scattered photons from the main analyzer at a Bragg angle near 45° ($2\theta \simeq 90°$, polarization factor $\cos^2 2\theta \simeq 0$, to separate the two polarization components) as shown in Figure 2.1.

In this chapter, design of a highly oriented pyrolytic graphite (HOPG) (Arkadiev *et al.*, 2007; Grigorieva *et al.*, 2003; Tuffanelli *et al.*, 1999) prototype PA is presented with its shape and estimation of the reflection and focus features, based on the analytical model and numerical ray tracing model (Monte-Carlo simulation). A PA with toroidal surface turns out to be the option under the consideration of

compromising the best energy resolution (smallest focus size) and best efficiency. Comparison of the focus features of programmed model and the results from the x-ray ray tracing software "SHADOW" (Sanchez del Rio *et al.*, 2011) is presented. This optic is matched to the Cu *K*-edge energy to help reveal symmetry information for excitations in RIXS studies of parent compounds of superconducting copper oxides. Characterizations of PA at Cu *K*-edge RIXS and preliminary polarization analyzed RIXS data of $CuGeO_3$ are displayed.

2.1 Geometry of RIXS with polarization analysis

In current hard RIXS spectrometers, sample, main analyzer and detector are all on the Rowland circle. The dispersed scattered rays from the main analyzer are analyzed and focused to a point-like spot on a one dimensional strip detector. Position sensitive detector is placed at the focus of main analyzer to capture varies energies that hit on different channels on the detector. On the MERIX spectrometer (Sector 30, APS), the detector is placed at a distance of 1 m away from the center of the main analyzer. The details of the sample/analyzer/detector are shown in Figure 2.1a.

Once removing the detector, the scattered beam from main analyzer converges to the focus and diverges spatially. The polarization analysis system is placed after the focus of main analyzer (named "primary focus") to refocus the divergent beam to the focus of PA (named "secondary focus") where the detector is relocated to.

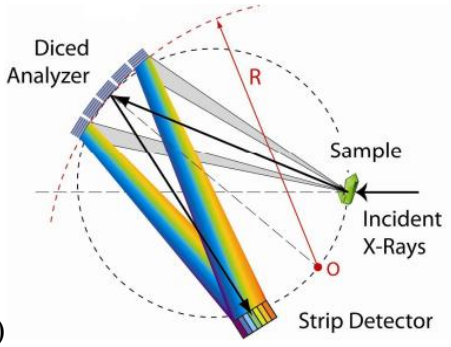

(a)

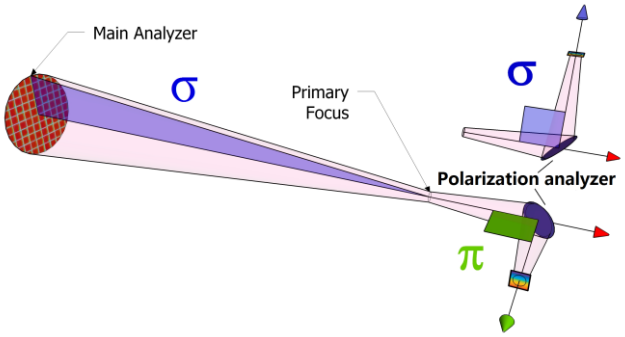

(b)

Figure 2.1 (a) Configuration of RIXS spectrometer. The scattering plane of the primary analyzer is shown. The strip detector is at the primary focus. Energy dispersion from the primary analyzer due to the flat diced crystal elements is shown by rainbow color. R is the radius of the primary analyzer. (b) Refocusing scheme with polarization analyzer. The blue triangle pointing left represents the scattering plane of the primary analyzer, as shown in Fig.2.1a. The strip detector is replaced with a polarization analyzer located behind the primary focus in one of two configurations. The strip detector is now placed at the focus of the polarization analyzer, the secondary focus. The two different configurations are named 'π' and 'σ'. In the configuration the scattering plane of the polarization analyzer (green square) is perpendicular to the primary scattering plane. In the configuration the scattering plane of the polarization analyzer (blue square) is in the same plane as the primary scattering plane.

The polarization analyzer is mounted on the detector arm of the RIXS

instrument after the main analyzer focus and results in a new sample/analyzer/analyzer (polarization analyzer)/detector pattern. As shown in Figure 2.1b, the photons scattered from the main analyzer can be separated to have a polarization perpendicular and a polarization parallel to the analyzer scattering plane (blue triangle). PA is mounted downstream of the focal point of main analyzer. The polarization component parallel to the main analyzer scattering plane can be eliminated by mounting the polarization analyzer to have the same scattering plane (blue rectangle) as the main analyzer. The polarization component perpendicular to the main analyzer scattering plane can be eliminated by mounting the polarization analyzer to have a perpendicular scattering plane (green rectangle) to the main analyzer's. These two configurations are named as "σ-σ" and "σ-π", corresponded to obtain the outgoing polarization in σ and π channel, respectively.

2.2 Flat graphite polarization analyzer

A preliminary test was utilized by a flat PA with Graphite (0 0 6) diffraction. PA was placed 3 mm before the primary focus Figure 2.1b. The advantage of this design is that all rays converge to the original focus in the case of flat reflector on the path of ray. SPI-1, SPI-2 and SPI-3 grades flat graphite were tested in the experiment. SPI-1, -2, and -3 have mosaicity of 0.4º, 0.7º and 1.0º, respectively. Flat analyzers was tested and found to have a very low overall efficiency (<0.1%) due to its angular acceptance limitation. The reflectivity in principle is on the order of 10 times larger. Although the large mosaicity in some sense increases the angular acceptance, the mosaicity are small compared to the beam convergence (~5.8º) from the main analyzer. Therefore, a more sophisticated polarization analyzer must be designed that captures all incident x-rays and images the x-ray spot from the primary focus with

high fidelity into a secondary focus at the detector. This can only be accomplished by a concave reflective optic placed behind the primary focus (Gao *et al.*, 2011).

2.3 Calculation of polarization analyzer surface

The scattered photons from the main analyzer within a certain solid angle (determined by the size and radius of curvature of the main analyzer) are reflected by PA symmetrically about the primary focus-detector axis. Therefore the optimization of the surface of PA can be simplified onto a two dimensional plane which contains the primary focus, PA and secondary focus. Once obtaining the optimized two-dimensional curve, the surface of PA is then the revolution of the curve about the axis trough the primary and secondary focus.

The 2D analytical model assumes that x-rays from the primary focus are a monochromatic point source, with an angular spread of 5.8° (cotangent of a 4 inches analyzer size and 1m radius of curvature). PA is placed at a constant distance (OA = 5cm,) from the source (0, 0) (primary focus of main analyzer) as shown in Figure 2.2. The reference ray OA is on the x-axis. φ ($-2.9° \leq \varphi \leq 2.9°$) represents angular divergence of the main analyzer. Spot size on the one dimensional detector plane is defined by the function $f(\varphi)$.

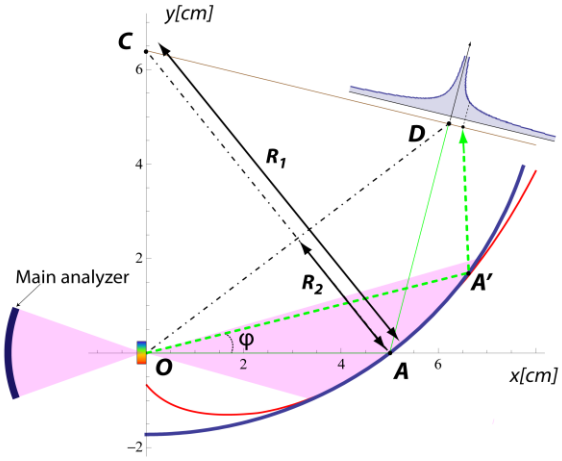

Figure 2.2 Polarization analyzer scattering plane. The beam from the energy selective analyzer (on the left) is shown schematically, with the rainbow indicating the position dependent spread of energies in the beam. The logarithmic spiral is shown in red. The blue curve is the circular approximation, of radius R_1 ($R_1 = |OA|/\sin(\theta_0)$), centered at C, to the logarithmic spiral around point A and represents the shape of the polarization analyzer. The polarization analyzer surface is generated by rotating the circular approximation about the OD axis by radius R_2 ($R_2 = R_1\sin^2(\theta_0)$). The photon source is positioned at O. A generic ray, in green, impinges on the polarization analyzer at A' and is reflected to the detector near the secondary focus, D. The curve at D represents the intensity distribution from a point source at O and is used to calculate the image broadening. From (Gao *et al.*, 2011).

There are two important factors which provide information to determine whether the PA surface is valuable. The first is the incident angular spread. For a monochromatic beam, each local point treated as a flat crystal on the surface reflects the x-ray that can be described by a rocking curve with a FWHM width $\delta\theta$ and peak reflectivity R_{max}. Ideally, one desire every ray hits on the PA surface with same incident angle (θ_B) under Bragg conditions, thus to be reflected by maximal reflectivity of the crystal. Then the overall efficiency is the peak reflectivity R_{max} independent on the incident angle. This is the case of PA with the surface of the

revolution of logarithmic spiral which will be introduced next. The other key factor is the spot size at the secondary focus. The position sensitive detector (Huotari *et al.*, 2005) detects energies of x-rays by pixel positions the x-rays hit. The detector has an intrinsic energy resolution broadening that depends on the pixel size. The spot size on the detector directly affects the overall energy resolution of the system. Large spot size corresponds to poor resolution. Therefore a successful design of PA surface is to have smallest focal size with reasonable overall efficiency.

2.3.1 Logarithmic spiral

Logarithmic spiral by its mathematical definition, has the property that the angle between the tangent and radial line at every point on the spiral is a constant (Hemenway, 2005). The curve of logarithmic spiral in polar coordinates is given by

$$\rho(\varphi) = \mathrm{a} \cdot \mathrm{e}^{\mathrm{b}\cdot\varphi} \tag{1.23}$$

Where ρ is the distance from origin, a and b are constants, φ is the angle from x-axis as shown in Figure 2.3. The angle ψ between tangent and radial line can be derived from the equation

$$\tan(\psi) = \frac{\rho \mathrm{d}\varphi}{\mathrm{d}\rho} = \rho / \left(\frac{\mathrm{d}\rho}{\mathrm{d}\varphi} \right) = \frac{1}{\mathrm{b}} \tag{1.24}$$

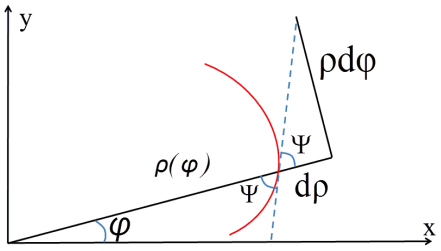

Figure 2.3 Schematic diagram of a logarithmic spiral.

Thus, $\psi = \cot^{-1}(b)$ is a constant. So by the mathematical definition, a logarithmic spiral is the optimal curve for collecting the entire divergent cone from an ideal point source to increase the point reflectivity (Suortti *et al.*, 1986b), since all the rays would have the same incident angle (θ_B) at every point on the diffractor surface. However, the focal spot size from a logarithmic spiral is not as good as the approximated shape (exact comparison will be shown later) (Wittry *et al.*, 1993). Thus, one approximated shape that have a much better focus without losing too much reflectivity can satisfy the requirements. As a good approximation about reference point P in Figure 2.2b, an osculating circle that has same tangent and curvature at point P as logarithmic spiral, indicates better focusing and manufacturing convenience. Therefore, we have chosen to work with a toroid shape, which is expected to be reasonable compromise for both focusing and meeting the Bragg condition (Wittry *et al.*, 1990).

2.3.2 Osculating circle

The osculating circle of a curve at a given point (point A, in Figure 2.2) is the circle that has the same tangent as well as the same curvature as the curve at point A. The osculating circle is the best circle that approximates the curve at A (Elsa Abbena, 2006). The radius of curvature is the length of AC shown as in Figure 2.2. The coordinates of center of the osculating circle C, can be derived from the parametric coordinates of the logarithmic spiral ($m(\varphi)$, $n(\varphi)$) as defined by Eq.2.1. The coordinates of the center C is given by:

$$x_c = m - \frac{(m'^2 + n'^2)n'}{m'n'' - m''n'}\bigg|_{\varphi=0}$$

$$y_c = n + \frac{(m'^2 + n'^2)m'}{m'n'' - m''n'}\bigg|_{\varphi=0} \tag{1.25}$$

As shown in Figure 2.2, a section of the osculating circle in the color of blue and the curve of logarithmic spiral in red have a good approximation in the vicinity of point A. In 3D space, a revolution of the osculating circle about the symmetric axis OD is a double-concave toroidal surface with minor and major radii of curvature R_1, R_2, respectively-*this is the design of PA surface*.

2.4 Calculations and results of important impact parameters

2.4.1 Incident angle $\theta(\varphi)$ on polarization analyzer surface

The logarithmic spiral and osculating circle in polar coordinates are given by

$$\text{logarithmic spiral}: \quad \rho(\varphi) = |\mathrm{OA}| \cdot \exp(\mathrm{b} \cdot \varphi) \tag{1.26}$$

$$\text{osculating circle}: \quad \rho(\varphi) = \mathrm{b} \cdot \sin(\varphi) + \sqrt{\mathrm{b}^2 \sin(\varphi)^2 + 1} \tag{1.27}$$

where b is the cotangent value of the Bragg angle θ_0, b = cot (θ_0). $\theta_0 = 38.2°$ is the Bragg angle for the graphite (0 0 6) reflection with the energy at the Cu *K*-edge. Here φ is the angle between a random ray and the reference ray as in Figure 2.2. The incident Bragg angle $\theta(\varphi)$ on the polarization analyzer surface can be calculated as the angle between the curve of osculating circle and every random ray:

$$\theta(\varphi) = -\varphi - \arctan\left(\frac{(\mathrm{b}\sin(\varphi) + \sqrt{\mathrm{b}^2\sin(\varphi)^2 + 1})\cos(\varphi)}{\mathrm{b}\sin(\varphi)^2 + \sin(\varphi)\sqrt{\mathrm{b}^2\sin(\varphi)^2 + 1} - \mathrm{b}}\right) \tag{1.28}$$

This expression can be approximated to a second order expansion of $\theta(\varphi)$ about the reference ray ($\varphi = 0$):

$$\theta(\varphi) \sim \theta_0 + \frac{1}{2}\varphi^2\mathrm{b} + \mathrm{O}\left(\varphi^4\right) \tag{1.29}$$

This parabola is a symmetric function about the reference ray, which is desired for good focusing. The function of incident angular spread is showed by the insert plot in Figure 2.4.

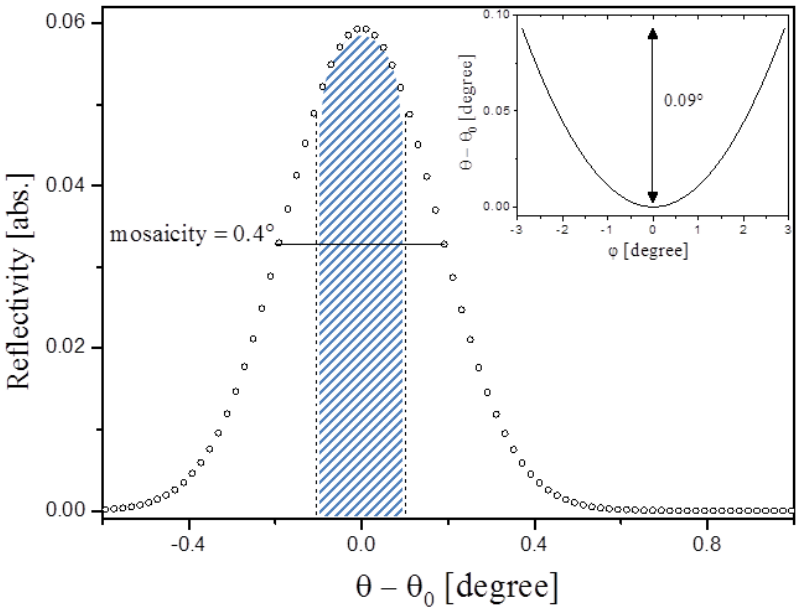

Figure 2.4 Rocking curve of graphite (006) diffraction at energy of E=8980.5 eV (Cu *K*-edge). Data were taken from software "XOP" (Sanchez del Rio *et al.*, 2004). Mosaicity of 0.4° (Gaussian width) is marked by the line on the curve. Peak reflectivity is 0.06. The insertion is the incident angle variation from Bragg angle as a function of the source divergence.

Incident angular has a range of 0.09° indicated by the shaded area in the rocking curve.

Calculation shows that the incident Bragg angle on the graphite reflector is 38 ° ± 0.09 °. Compared to the large crystal mosaicity ~0.4° of the graphite, this deviation caused by the shape approximation is certainly acceptable without losing too much reflectivity.

2.4.2 Average reflectivity

The relevant reflectivity of the graphite PA is a function of φ, given by:

$$\mathrm{R}(\varphi) = \exp\left(-\frac{1}{2} \frac{(\theta(\varphi) - \theta_0)^2}{\Delta\theta^2} \right) \tag{1.30}$$

Thus, the average relevant reflectivity of the graphite diffractor can be calculated by the integral of the reflectivity curve. The result is $R_{ave} = 0.9945$ for $\Delta\theta = 0.4°$.

$$\int_{\varphi_-}^{\varphi_+} (\varphi_+ - \varphi_-)^{-1} \mathrm{R}(\varphi) \mathrm{d}\varphi \tag{1.31}$$

where φ_+, φ_- is the upper bound and lower bound of the scattered beam from main analyzer, respectively. The relevant reflectivity as a function of the beam cone is shown in Figure 2.5.

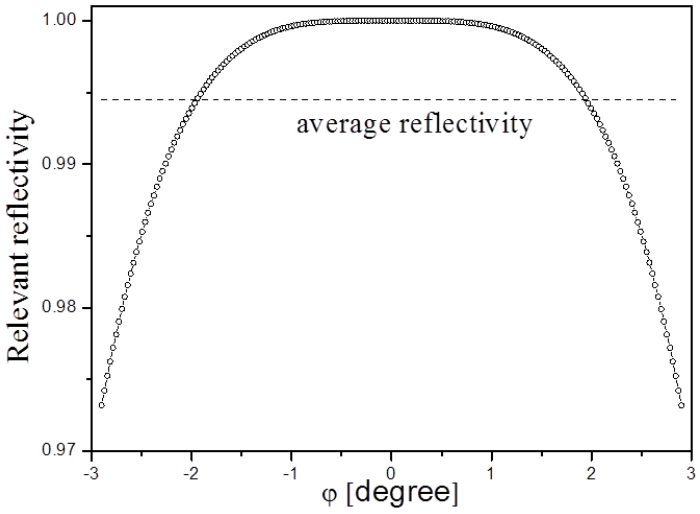

Figure 2.5 Plot of relevant reflectivity as a function of φ. The average reflectivity is 99.45% relative to the peak reflectivity of the rocking curve of graphite Figure 2.4.

2.4.3 Polarization factor

Linear polarization components of an x-ray beam can be separated by in and out of plane Bragg reflections with a Bragg angle close to 45 °. The purpose of the PA is to measure the inelastic signal after the elimination of one linear polarization component. The success of this endeavor can be expressed by the polarization factor, $PF = \cos^2(2\theta)$, where θ is the Bragg angle. A perfect PA, with $\theta = 45$ °, will have PF = 0. For our analyzer, which uses the (0 0 6) reflection of HOPG, the Bragg angle is 38.2° at the Cu *K*-edge. The effective polarization factor is 0.05801, which integrates polarization factor $\cos^2(2\theta)$ over the whole surface, so that ~94.2% of the linear polarization component parallel to the scattering plane of the polarization analyzer is eliminated.

2.4.4 Focal spot size

Focal spot size function f(φ) is a function of beam divergence φ from the main analyzer which represents the distance deviation from the reference focal point. The function is given by:

$$f(\varphi) = -5\left(1-\rho(\varphi)\sin(\varphi)\right)\cot\left(-\varphi-2\theta(\varphi)\right)+5\rho(\varphi)\cos(\varphi) \qquad (1.32)$$

This focusing is not as perfect as the point to point focusing generated by the ellipse optics but a reasonable approach. Focal spot size at the secondary focus with 5cm focusing distance is ~78 μm for a primary monochromatic point source, which is an acceptable broadening compared to the 350 μm for a 100 meV wide beam (this is the overall energy resolution from using main analyzer Ge (3 3 7) in regular RIXS scheme). Without a detailed calculation, one can approximately estimate the overall resolution is broadened to 122 meV by the imperfect focusing.

Energy resolution is an important factor in RIXS experiment so that an analyzer with a relatively large broadening is not practical. The energy resolution broadens when the x-ray spot imaged from the primary focus to the secondary focus. To study these effects further we carried out ray tracing of our optics using Monte Carlo methods. We generate the appropriate source at the primary focus and trace the rays to the detector (secondary focus). Given our configuration, a source with a Gaussian profile will be broadened by ~33% at the secondary focus shown in the Figure 2.6. This corresponds to a calculated decrease in the energy resolution from 100 meV to 133 meV. With a revolution logarithmic spiral the resolution would increase to 200 meV.

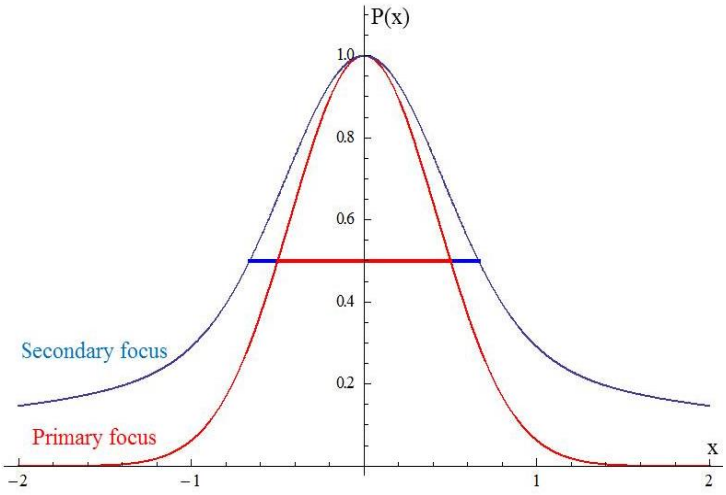

Figure 2.6 Spot size broadening of circle is a comparison by a Gaussian distribution at the primary focus (red curve) and the distribution at the secondary focus (blue curve) convoluted with the distribution from optics. x is the size of the spot, normalizing the FWHM of red curve to 1. The FWHM of the blue curve is about 1.33 so that the broadening effect from the PA is 33%.

2.4.4 Mosaicity vs reflectivity

A non-perfect crystal with a mosaicity can be thought to be built-up by many crystalline blocks inside the crystal. Each block is treated a perfect crystal. The mosaic blocks are not exactly oriented as the diffraction direction, but oriented as a Gaussian distribution around the reference direction within a certain mosaicity, which is usually in a range of 0.1~1 degree. An important consideration of mosaic crystal is the secondary extinction depth that represents the x-ray penetration inside the crystal. Once the thickness of the crystal is thinner than the distinction depth, the total thickness is penetrated by x-ray and the throughput (reflectivity) is reduced. As following the conceptual model of mosaic crystal (del Rio *et al.*, 1992), the reflectivity of a mosaic crystal is given by

$$R(\theta-\theta_B)=\frac{a}{1+a+\sqrt{1+2a}\coth(\frac{\mu t}{\sin\theta_B}\sqrt{1+2a})} \tag{1.33}$$

With

$$a=\frac{(\delta\sqrt{2\pi})^{-1}\exp\left(-(\theta-\theta_B)^2/2\delta^2\right)Q_s}{\mu} \tag{1.34}$$

Where μ is the linear absorption coefficient, t is the thickness, θ_B is the Bragg angle, and δ is the mosaic spread. Q_s is a constant related to structure factor, and incident wavelength for σ polarization. We calculated the integrated intensities versus mosaicities of graphite crystal to estimate the mosaic effect on crystal reflectivity for thin and thick crystals. The result is shown in Figure 2.7

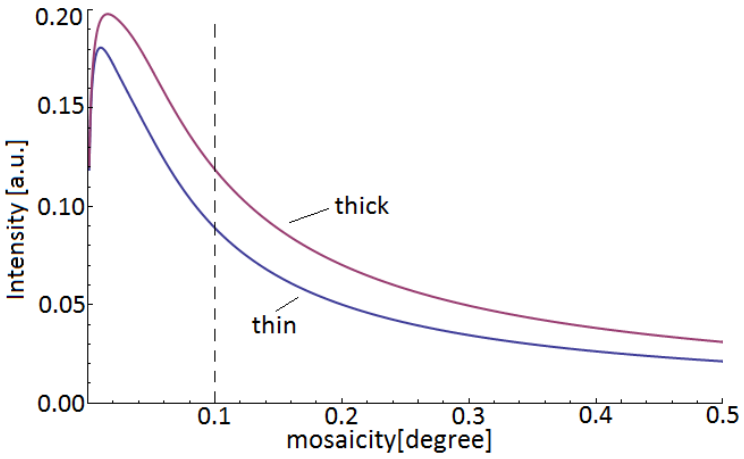

Figure 2.7 Integrated intensity vs crystal mosaicity for graphite. The red curve is for a thick crystal, thickness = 7 mm; the blue curve is for a thin crystal, thickness = 0.5 mm. The calculation combines the angular spread in our model and the crystal mosaicity (W. H. Zachariasen, 1967). The calculation covers all the mosaic values, but the region below the dashed line is beyond the fabrication limit of mosaic graphite crystal.

The 0.5 mm and the 0.4° were the respective limits for the maximum thickness and smallest mosaic that could be coated onto our substrate by the manufacturer. As shown in Figure 2.7, the desired mosaic value is under 0.1°, but the best graphite commercially available for this application has a mosaic of $\sim 0.4°$ which gives a total throughput of 15% of the maximum in the ideal. The secondary extinction depth for PA is about 4.7mm in our case. By comparing two integrated reflectivity curves, for the PA with 0.5mm thickness, at the $0.4°$ mosaicity the integrated reflectivity of the polarization analyzer is reduced by 31%.

2.5 Monte Carlo simulation−3D ray tracing of an analyzer with a toroidal shape

To further evaluate the quality of PA, we used Monte-Carlo method in a 3D space to simulate the real ray traces of PA, which matches the 2D analytic model. The ray tracing model includes three important parts: source, optical element (surface of PA in our case) and image which are shown in Figure 2.8. We simply the source features as geometric source: each ray is a ray vector that has several parameters of interest, for instance, $\mathbf{ray}_i$ (x_{i0}, z_{i0}, V_{ix}, V_{iy}, V_{iz}, I_i, e_i) has a starting origin (x_{i0}, z_{i0}, y coordinate is assumed to be zero), incoming direction vector (V_{ix}, V_{iy}, V_{iz}), intensity I_i and an energy of e_i. Once a ray is generated, based on the direction of the ray and analytical function of the optical element surface, the incident path can be calculated. Therefore, the intersection point and normal vector at the intersection point can be obtained. Then the outgoing vector can be obtained by the intersection point and normal vector based on the reflection relation shown in Figure 2.8. Finally, the intersection point with image/detector plane can be obtained depending on the focusing distance and outgoing vector. Furthermore, since the optical element

graphite is not a simple mirror, the local reflectivity information related to the crystal rocking curve needs to be included for each intersection point on the optical element surface.

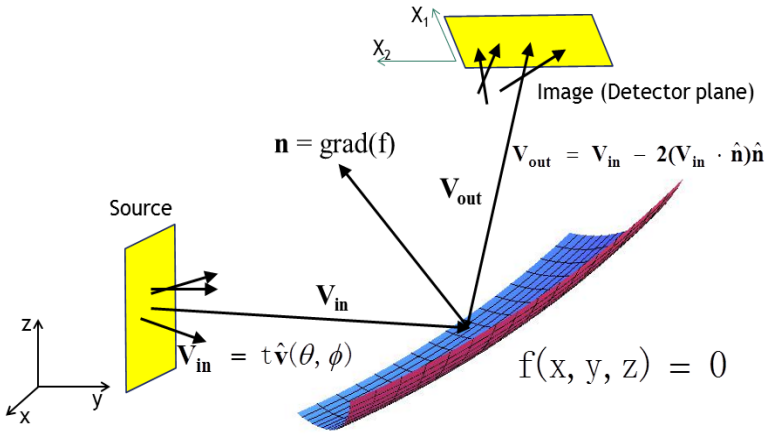

Figure 2.8 Schematic ray tracing model. A ray vector generated on the source plane with an incident vector $\mathbf{V}_{in}$ is reflected at the PA surface based on Braggs law. Each reflected ray is recorded at the 2D detector plane.

2.5.1 Monte Carlo loop

Monte Carlo ray tracing simulation can be achieved by tracing the path of a single ray from the source to the image plane and repeating the trace loop for thousands of rays randomly generated at the source to simulate the real diffraction process and obtain the full information at the image plane. The details for each step in the loop are shown in Figure 2.9.

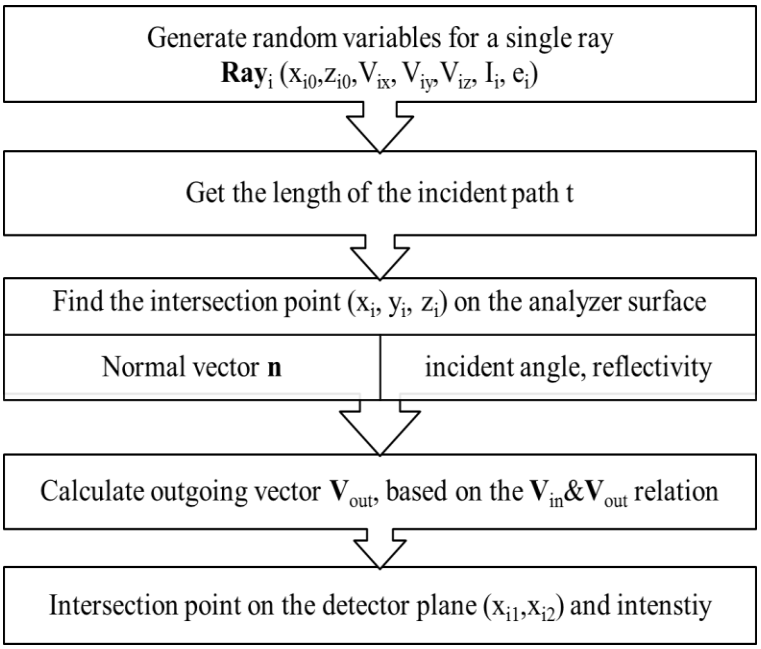

Figure 2.9 Flow chart of the ray tracing loop of Monte Carlo simulation. This process is not only specified for the PA case, but also generally used for different source contributions and optical elements of interest.

After running the ray tracing loop, all the information of the diffracted beam at the detector plane is seperately stored in different columns in the output data file, e.g. reflected path, coordinates at the image plane, intensity, and energy. For plotting the result, one can choose two or three columns to get the 2D or 3D graph of different parameters of interest.

2.5.2 Results at the image plane

The simplest case is for a monochromatic point source at the origin. The 3D focus feature is shown in Figure 2.10a compared with the image of the focus

calculated from SHADOW1.04 shown in Figure 2.10b. Both results are showing a 'butterfly'-like focus for a point source on a toroidal surface. The major and minor radius of the toroid is 3.08 cm and 8.12 cm and the incident Bragg angle is 38.2°. Source-plane distance and image-plane distance are both 5 cm. The local reflectivity is based in the Gaussian reflectivity curve of graphite (006) at Cu *K*-edge from XOP2.3.

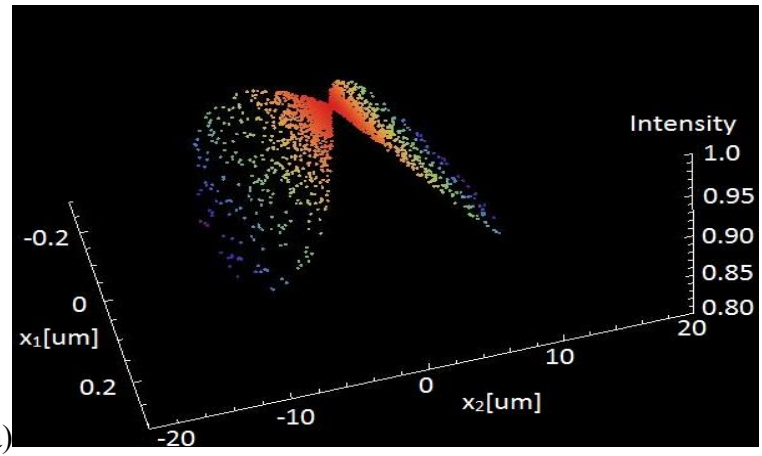

(a)

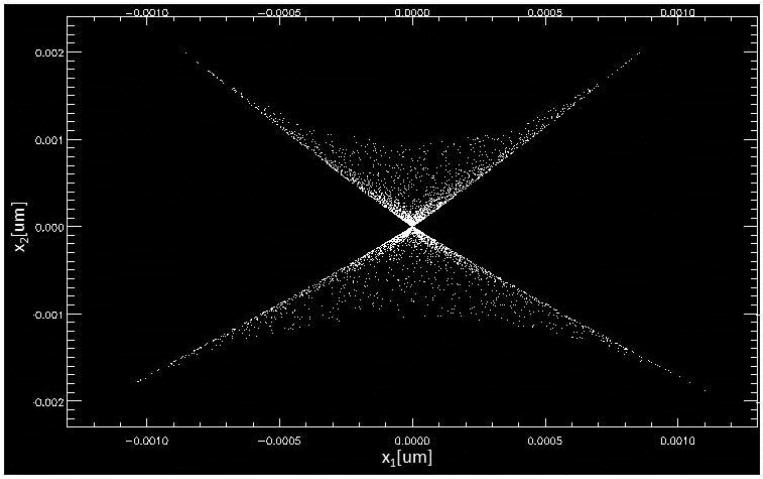

(b)

Figure 2.10 (a) 3D image at the detector plane of a monochromatic point source calculated by the simulation model. Simulation programmed in Mathematica 8.0 (Wolfram, 2009). (b) 2D focal image calculated by SHADOW for the same input parameters as the Monte Carlo model.

Considering the real case, the main analyzer that is diced to 1.5×1.5 mm^2 pixels collects the photons within a certain solid angle from the sample and focus the beam to a 3 mm spot (twice of the pixel size) on the detector. Therefore, a ray tracing model of a finite source with a size of 3×3 mm^2 is simulated to have a focus profile shown in Figure 2.11a. The most interesting character of an analyzer is the energy resolution broadening at the focus. The calculated energy resolution function at the secondary focus is shown in Figure 2.11b, considering the energy distribution is linearly distributed at the primary focus with a bandwidth of 100 meV, which is the overall energy resolution after a Ge (3 3 7) main analyzer at incident energy of Cu *K*-edge.

(a) 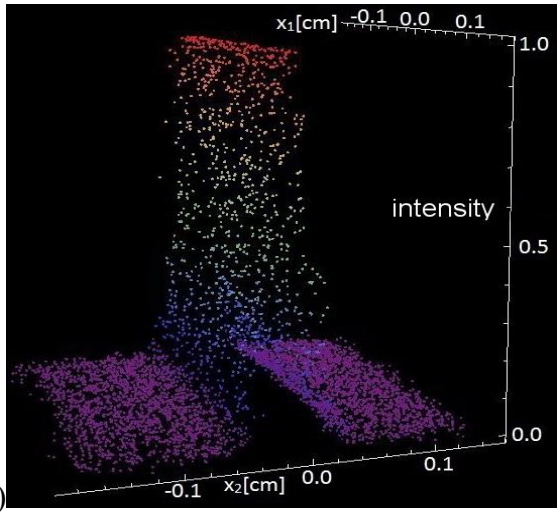

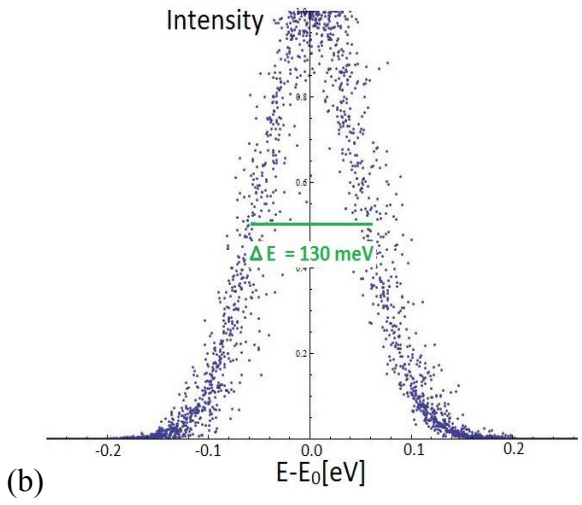

(b)

Figure 2.11 (a) Focus of a finite source. Simulation is from the ray tracing model programmed by Mathematica 8.0. (b) Energy resolution at the secondary focus.

The estimated energy resolution at the secondary focus is enlarged by a factor of 30% of the primary focus, which coincides with increment of the FWHM of the real focal spot size at the secondary focus as shown in Figure 2.6.

2.6 Prototype of HOPG polarization analyzer

The polarization analyzer is a HOPG (0 0 6) reflection. For resonant studies with incident energy near the Cu *K*-edge the graphite has a Bragg angle of about 38.2°. The angular spread on the polarization analyzer is 5.8° due to the size and radius of curvature of main analyzer. To gather the entire cone, one has to shape the crystal, since the crystal mosaicity (0.4°) of flat graphite is relatively small compared to the angular spread. Instead an appropriate shape of the HOPG surface is designed in the 2D reflection plane. The shape is toroid-like due to symmetry about the optical axis. The two toroidal radii used are R_1 = 3.08 cm and R_2 = 8.12 cm based on the

calculation from the ray tracing model. The polarization analyzer is designed to work at 5 cm focusing distance for both σ and π reflection direction. After the shape was machined, it was coated with graphite with a thickness of 500 μm. A thicker layer would benefit the overall efficiency due to the penetration of the incident x-rays, but this is the maximum thickness that the manufacturer (Optigraph GmbH, Germany) can offer without increasing slope error. The numerical surface of PA and the actual PA coated by HOPG are shown in Figure 2.12.

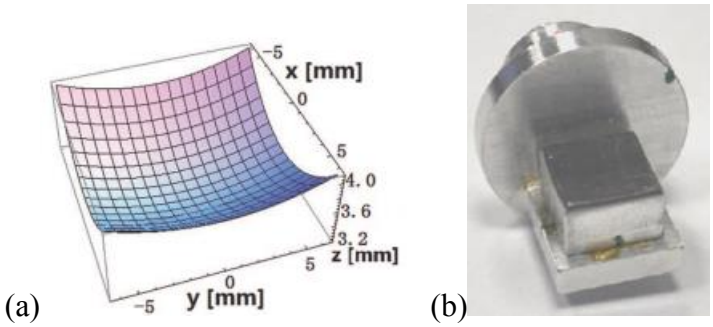

Figure 2.12 (a) Numerical double-concave surface. (b) HOPG polarization analyzer coating on a toroidal aluminum substrate (manufactured by Optigraph GmbH).

2.7 Experimental results

The PA designed for the hard RIXS at Cu *K*-edge was characterized at Sector 30, APS. The details for experimental setup, alignment of polarization analysis system, resolution function of with polarization analysis system are described in this section. The full characterization of HOPG PA and the polarization analyzed RIXS data of $CuGeO_3$ are presented as well.

2.7.1 Experiment setup and alignment

As in a standard RIXS setup, the main analyzer provides the energy and momentum analysis. The beam reflected from the main analyzer contains both σ and π polarization components.

The PA is placed 5 cm beyond the focal point of the main analyzer (Ge (3 3 7)). The PA reflects the outgoing beam from the main analyzer at $2\theta = 76.4°$ giving predominantly σ or π polarizations. The polarization factor for this reflection is given by $\cos^2(2\theta)$ or about 6% contamination from the other polarization direction. The PA refocuses the scattered photons onto the position sensitive strip detector (MYTHEN) which is placed 5 cm away from the PA at the appropriate 2θ value.

The PA was mounted on the detector arm of MERIX instrument in two different configurations σ and π, as shown in Figure 2.1b. After removing the detector in the conventional RIXS setup, PA is placed 5 cm beyond the primary focus and strip detector is placed 5 cm away as well to coincide with the secondary focus.

The polarization analysis system is roughly aligned putting the direct beam on the primary analyzer. The primary and polarization analyzer are then aligned so that the Bragg reflection of the primary analyzer impinges on the polarization analyzer at its Bragg angle. Next, 3M Magic 810 Tape, a fairly uniform elastic scatterer, was placed in the sample position and the primary analyzer was moved to the peak of the elastic structure factor for the tape (about 20° away from the direct beam). The main analyzer was in the same position for measurements of both polarization directions and the same tape sample was used. Elastic scattering from the tape will have the same polarization as the incident beam (σ). The fine alignment is performed in this configuration. The fine alignment is the adjustment of the polarization analyzer distance from the primary focus, the distance of the detector from the polarization

analyzer, and the polarization analyzer angle. Since the synchrotron does not produce π polarized x-rays, alignment for scattered π polarization relies on the small amount (6%) of the σ scattering present since the scattering angle is not exactly 45°.

2.7.2 Characterization of polarization analyzer

In the standard RIXS operation without polarization analysis, the spot size at the primary focus is about 350 μm on the detector, which corresponds to a 100 meV energy bandwidth. The energy resolution function of elastic scattering measured from a tape standard without PA is shown in blue in Figure 2.13. The polarization of elastic line is σ which is the same as the incident polarization of the synchrotron.

The energy resolution function of PA in σ-σ polarization configuration is shown in the Figure 2.13a. With polarization analysis, the FWHM of elastic scattering broadens from the 100 meV at the primary focus to 175 meV at the secondary focus. The broadening comes from the inexact focus of the polarization analyzer, the mosaic spread of the HOPG, and the finite penetration depth of the HOPG.

The resolution function in σ-π configuration is shown in Figure 2.13b. The weak elastic scattering comes from the 6% remnant of the σ polarization. In the ideal case of polarization analysis, the elastic scattering is eliminated by the PF = 0, and is very difficult to align upon the elastic scattering of the system. But aligning the polarization analysis system in σ-π configuration by the intense inelastic signal from a well-known sample is a reasonable solution.

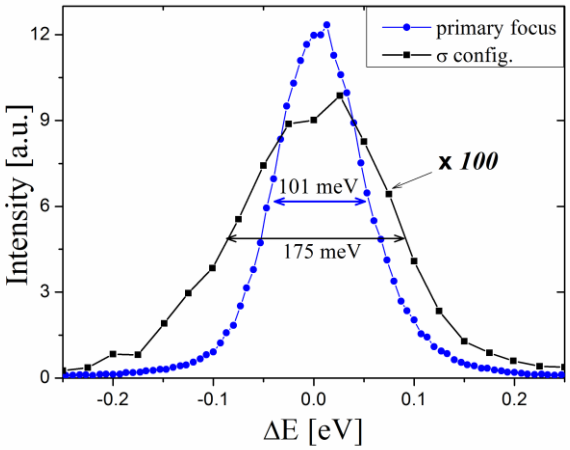

a)

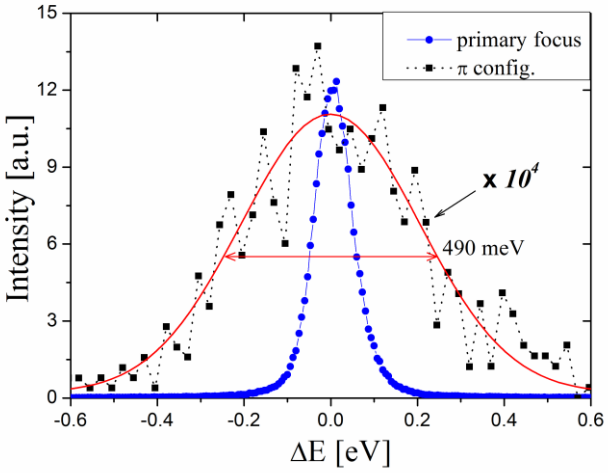

(b)

Figure 2.13 Elastic scattering from the tape standard. (a) σ-configuration. (b) π configuration. The scattering at the primary focus, without polarization analysis, is shown in blue. The polarization analyzed signals are shown in black.

The efficiency of the PA can be estimated by integrating the two energy resolution curves at the primary and secondary focus in σ-σ configuration. The ratio of

integrated intensities is ~0.014. This is about four times less than the peak reflectivity of 0.5 mm HOPG with a mosaicity of 0.4° which is 0.06. The efficiency of an ideal PA with should be same as the peak reflectivity since all the rays are reflected at exact Bragg angle. The ratio of the integrated intensities in σ-π configuration is about 4.0e-4 This ratio, when normalized by the measured efficiency, should be equal to the polarization factor. The integrated intensity is about half of the expected number, suggesting there are additional efficiency losses in the π configuration.

The elastic line width in the π configuration is unexpectedly large, 490 meV. The precise reason for this broadening is not known but may result from fabrication errors in the polarization analyzer. Since the detector position is flipped in the π direction compared to the σ direction while the polarization analyzer is not, the two reflections are affected differently by fabrication errors. Full characterizations of the PA are tested and shown in Table 2.1.

Table 2.1

Characteristic values of HOPG polarization analyzer

Average reflectivity	0.059	
Bragg angle θ	38.2 °	
Effective polarization factor	0.05801	
Efficiency η	1.36%	
Polarization Configuration	Measured Relative Integrated Intensity	Measured Relative Energy Width
None	1	1
σ	1.4E-2	1.75
π	4.0E-4	4.86

2.7.3 Polarization analyzed inelastic spectrum of $CuGeO_3$

A preliminary measurement of a superconducting parent cuprate $CuGeO_3$ with polarization analysis system was carried out after the characterization of the PA. $CuGeO_3$ is a good candidate as an initial polarization analysis measurements since it is well characterized and studied by conventional RIXS measurements (Suga *et al.*, 2005). Two spectra (with and without polarization analysis) from $CuGeO_3$ are displayed in Figure 2.14. Both spectra are measured at momentum transferred Q = (2.6 0 0) in reciprocal space using the spectrometer in horizontal geometry. The incident polarization was normal to the crystal c-axis. The black spectrum was measured with a polarization analyzer in the σ configuration. In both cases the well-known 6.5 eV charge transfer feature is shown.

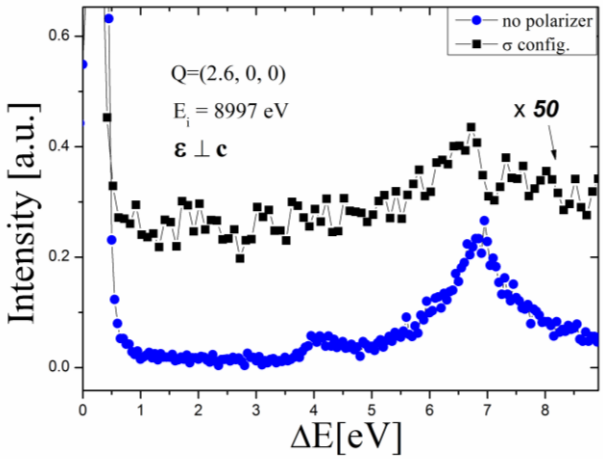

Figure 2.14 RIXS spectra of $CuGeO_3$. Blue: without polarization analyzer. Black: with polarization analyzer in the σ configuration.

With polarization analysis the broad inelastic peak around 7 eV is separated to a sharper bump on left shoulder to some extent. The preliminary measurement is to

emphasize the ability to detect inelastic signals with sufficient count rate and energy resolution with the PA. More detailed understanding of the underlying physics of the sample and other cuprate systems needs more polarization analyzed measurements in the future.

CHAPTER 3

SILICON-BASED POLARIZATION ANALYZER

In the previous chapter, the low count rate of the scattered polarization from the HOPG polarization analysis system requires us to develop a more efficient polarization analyzer working in the same outgoing polarization configuration. A HOPG PA with mosaicity of 0.4° was characterized to have an overall efficiency of 1.36%. The reflectivity as a function of mosaicity indicates the maximal reflectivity is at a mosaicity ~0.01° as shown in Figure 2.7., which can provide the integrated efficiency about 7 times the efficiency of the crystal with 0.4° mosaic. This leads us to develop a new type of PA using a bent perfect crystal such as Si or Ge, to improve the efficiency of PA since the reflectivity width of a bent perfect crystal is in the same order as 0.01°.

Since we developed the first bent crystal PA, much current research about the role of spin-orbit coupling in transition metals systems using RIXS at Ir *L*-edge (E = 11.215 keV for Ir L_3-edge) have been carried out (Hirata *et al.*, 2013) and these systems are attracting more interest (Boseggia *et al.*, 2013). Interesting excitations, e.g. single and two magnons excitations are being studied and can be reasonably explained by theoretical models (Haverkort, 2010). The magnetic excitations involve polarization dependence (Hannon *et al.*, 1988), but they are not currently measured in a way that allows polarization analysis. With polarization analysis, the nature of magnetic excitations can be revealed by symmetry arguments (Ishihara *et al.*, 2008) instead of the theoretical complexities. These issues encouraged us to develop the PA at Ir *L*-edge.

Ir L_3-edge RIXS is currently a hot topic, which is a direct RIXS process to the 5*d* states related to exotic magnetic properties of material, having stronger inelastic signal than Cu *K*-edge that benefits throughput of the optics. We developed a bent Si (444) polarization analyzer bent to a double-concave shape working at the Ir L_3-edge. This analyzer works at a Bragg angle θ_B of ~45° meaning it can totally eliminate the in-plane reflection by polarization factor; therefore obtaining a nearly pure polarization component of scattered photons. The RIXS process in TM *L*-edge is a direct transition rather than the indirect process in *K*-edge RIXS. The inelastic throughput at *L*-edge is orders of magnitude larger than at the Cu *K*-edge. The count rate at Ir *L*-edge is on the order of hundreds of counts per second compared to a count per second at the Cu *K*-edge, so the polarization analysis at the Ir *L*-edge will yield reasonable signal rates with the expected efficiency of PA.

In this chapter, the features of a bent Si PA based on the strong bending theory of a perfect crystal, the fabrication of the bent Si PA to a double-concave shape, and the characterizations with different method such as metrology, topography, etc. of the PA are presented respectively. The bent Si PA was preliminary tested at the 9ID with the polarization analyzed RIXS data of Sr_2IrO_4.

3.1 Features of strongly bent Silicon

Perfect crystals such as Si or Ge, are the ideal material to fabricate the analyzer for hard RIXS experiment because of their high reflectivity and narrow intrinsic Darwin width. The analyzers for RIXS experiments are typically spherical, diced and placed on the Rowland circle working at near backscattering configuration (Blasdell *et al.*, 1995; Verbeni *et al.*, 2005). Each Si pixel on the analyzer is a small flat crystal that reflects the x-ray at different solid angle. The closer the Bragg angle is

approaching to 90 degrees the higher energy resolution. The diced bent analyzer is generally treated as a perfect crystal but does not act like a bent crystal since the diced cubes are separated and can be accurately treated as perfect crystals without any distortions. The bent crystal is typically a wafer bent to a curved surface without dicing. The polarization analyzer aims to reflect the outing beam at ~45 degrees to obtain photons in one polarization direction and eliminate the photons with the orthogonal polarization direction. This requires larger angular acceptance of the polarization analyzer. The bent shape of bent Si PA satisfies the criteria of strong bending. The criterion for judging whether a bent crystal has a small or large deformation depends on the ratio of the maximum deflection and crystal thickness (Krisch *et al.*, 1991). The diffraction of crystal under deformation no longer follows the dynamical theory but moves to the kinematical region.

The diffraction profile of bent crystals compresses the rocking curve of a flat crystal perfect crystal by increasing the reflection width and decreasing the peak reflectivity. The general diffraction theory of a distorted crystal can be explained by the Takagi-Taupin (TT) equations (Takagi, 1969; Taupin, 1964) which describe the diffraction by electromagnetic wave propagation inside the crystal. Solving the Maxwell equations completely to obtain an analytical solution is limited to some special cases, and even the numerical solution cannot work for general bent cases. Especially for our case of biaxial bending, finding a diffraction profile by TT equations is not practical. The multi-lamellar (ML) method (White, 1950) is a good approximation to calculate the diffraction profile which decomposes the crystal into many crystallographic atomic planes; each plane acts as perfect crystal, but with a certain tilted angle between neighboring layers (Sanchez del Rio *et al.*, 1997). This method can be used from the small deformation to strong bending to a radius of

curvature of a few cm and was used to optimize the monochromator for inelastic scattering (Erola *et al.*, 1990; Suortti *et al.*, 1986a) and bent crystal analyzer for fusion plasma diagnostics (Caciuffo *et al.*, 1990).

Bending Si about a unique axis (called cylindrical bending as well) would enlarge the reflection width and reduce the peak reflectivity due to the distortion of crystal planes generated during the bending. This bending effect on the rocking curve of bent crystal for different radii of curvature is shown in Figure 3.1a, which is calculated by XOP2.3 (Sanchez del Rio *et al.*, 2004) according to multi-lamellar code (Caciuffo *et al.*, 1990).

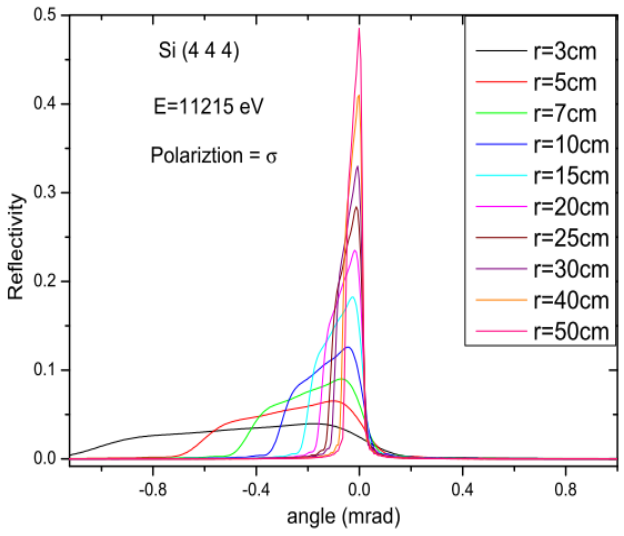

(a)

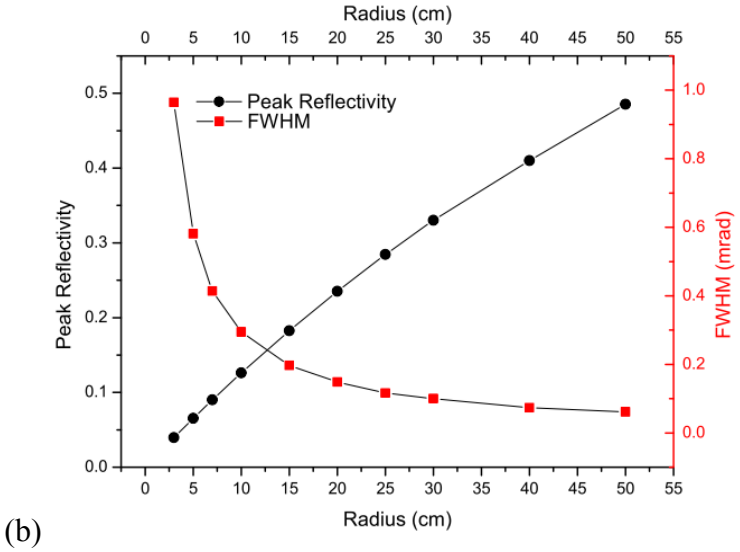

(b)

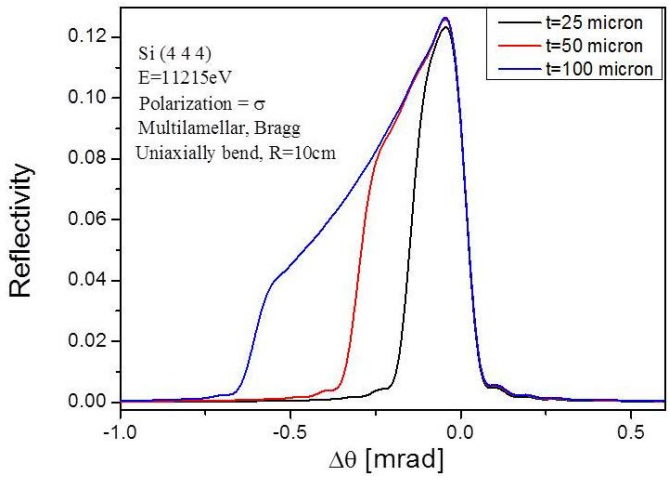

(c)

Figure 3.1 (a) Rocking curves of the bent Si (444), thickness = 50 micron, at different bending radii with the incident energy at Ir *L*-edge. (b) Peak reflectivity and FWHM of the rocking curve at different bending radius. (c) Rocking curves of bent Si with bending radius R=10cm for different thicknesses.

The rocking curve width of perfect Si crystal is typically in the range of a milliradian. As shown in Figure 3.1b, the broader rocking curve width of a bent crystal is in the range of 0.1~1milliradian, which effectively helps to increase the angular acceptance

of the bent polarization analyzer, and accordingly increase the whole analyzer efficiency. Figure 3.1b indicates the reflecitvity might increase by a factor of 10~20 from the HOPG crystal when the bending radius is less than 15 cm. Figure 3.1c shows the diffraction profile of a certain bending radius with different thickness. The peak reflectivity are at same level but the angular width of thicker crystal is much larger which benefits the integreted intensity. The bent Si PA is chosen to be made by 100 μm thickness wafer to gain integrated intensity and better wafer quality than the 50 μm as the first attempt. There is no practical calculation for biaxial bent crystal, but the reflection width is expected to be wider than uniaxial bending since the diffraction planes in the crystal are distorted by the additional mechanical tension applied.

3.2 Prototype of bent Si polarization analyzer

3.2.1 Fabrication of bent Si polarization analyzer

At the near-back scattering configuration, a spherically bent crystal shows the best spatial resolution and can be widely used as x-ray analyzer (Rio *et al.*, 1997). But if not at the near-backscattering configuration, an optic with toroidal shape has the minimum astigmatism when the source-crystal distance and crystal-detector distance is the same (Sinars *et al.*, 2003). Good focusing features of HOPG PA have been explained in previous chapter. Fabrication of bent Si PA is carried out by mechanically pressing the ultrathin (50 μm ~ 100 μm) Si wafer to a toroidal surface.

The conventional fabrication method of spherical analyzers (Blasdell *et al.*, 1995) is to press the Si wafer with a spherical concave lens on the bottom and a spherical convex lens on the top of the Si wafer under a hydraulic pressure on the top lens as shown in Figure 3.2a. For diced crystal analyzer, the diced wafer needs to be

glued onto a polycarbonate substrate in advance. As the first attempt, we followed the same way as the conventional pressing method to press the 50 μm Si wafer to a toroidal concave substrate, but the crystal is too fragile when applying a pressure on the top. The fragment comes from the uneven force applied during the press process due to the asymmetric toroidal shape, small radii of curvature, off axis between the convex and concave lenses. Reduction of pressure can avoid the breaking, but the surface error (basically the radii of curvature) is not acceptable.

These led us to develop a novel method to manufacture the analyzer, using one single lens as the presser rather than two, trying to avoid the constraints from the other lens. The way is to apply an elevating pressure from the bottom with a convex lens pressing the Si wafer to a flexible thin material. When slowly applying the pressure underneath, under the reaction force from top material the thin Si wafer will be gradually bent onto the convex shape until the top material, Si wafer and the convex lens are coincide. The elevation frame and method are shown in Figure 3.2b, compared with the conventional pressing of x-ray analyzer shown in Figure 3.2a.

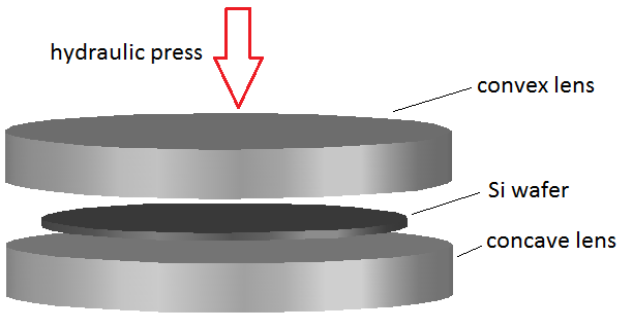

(a)

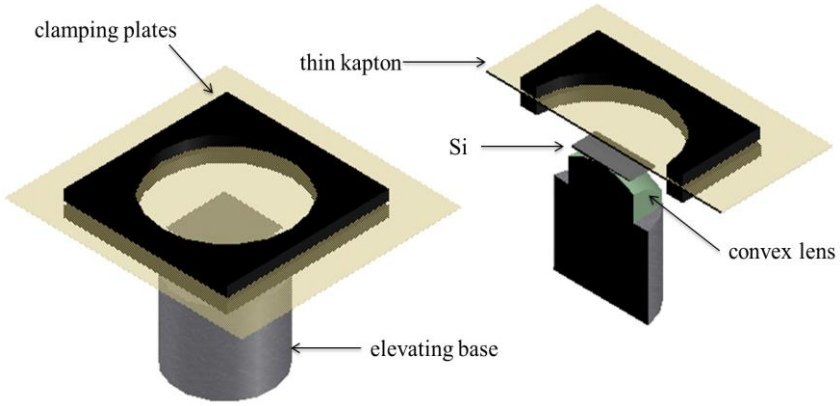

(b)

Figure 3.2 (a) Fabrication method of spherically bent crystal x-ray analyzer. Convex and concave lens on the top and bottom of crystal wafer. (b) Elevation press method for fabricating bent Si PA. Clamping plates hold kapton foil to deform to the toroid shape. Si wafer is between the convex lens and kapton foil.

3.2.2 Process of pressing and molding

The elevating fabrication method had been tested and required several conditions to work: the surface of the Si wafer is small; the crystal wafer is not thicker than 250μm; for the size of our PA, the elevation needs to be at least 6 ~ 7 mm relevant to the flat kapton level.

Fabrication process for bent Si PA are:

1. Prepare the mixing low viscosity expoxy (EPO-TEK® 301-2) in hand.
2. Set up the items in sequence from the bottom to the top: elevating base, convex lens, Si wafer, glue, bottom clamping plate, 60 μm kapton, top clamping plate, repectively. A half drop of glue is enough to spread all over the whole surface of Si.
3. Elevate the lab jack gradually. The kapton deforms and compresses the flat Si

piece to the convex lens.

4. The elastic deformation of the kapton film drives the pressure from the center of cystal to the edge around until kapton foil eventually coinicides with the convex shape. Keep the configuraton for a few days until the glue is totally cured.
5. The last step is to cast a substrate on the top to keep the bent shape still. This step is carried out after the glue is totally dry. I used the 2-ton epoxy (by Devcon). It drys in 24 hours and hardens in 1~2 days. Dow Corning 7 mold release compound between the casting material and mold frame was used to allow removal from the casting materical.

3.2.3 Protype of bent Si polarization analyzer

The prototype of the bent Si PA is a Si (4 4 4) Bragg reflection suitable for the Ir L_3 absorption edge (E = 11.215 keV). The Bragg angle $\theta_B = 44.8448°$. This Bragg reflection is nearly ideal ($2\theta_B = 90°$) for a PA, which a PF = 0.005 that reduces the mixing polarizations by a factor of 12 from the HOPG PA. 99.5% of the in-plane ougoing polarization is eliminated and nearly pure out of-plane polarization is obtained.

PA is fabricated from a 100 μm thickness Si wafer. 100 mm diameter Si wafer was purchased from Addison Engineering, Inc. and cut to ~ 2×2 cm^2 square piece by diamond cutter before pressed. The maximum path length inside the crystal is 66 μm (calculated by the XOP Bent Crystal Module code (Sanchez del Rio *et al.*, 2004)). 100μm wafer is the thinnest comercially avaible with good quailities.

This opics is designed to be placed downstream after the primary focus with both primary focus-PA and PA-detector distance equal to 10 cm. The major radius of curvature R_1 in the meridional plane and the minor radius curvature R_2 in the sagittal

plane are 141.8 mm, 70.5 mm respectively. The relations bewteen the focusing distance and Bragg angle, and the relation bewteen R_1 and R_2 have been described in the design of HOPG PA in Chapter 2. Numerical surface and the manufactured object are shown in Figure 3.3.

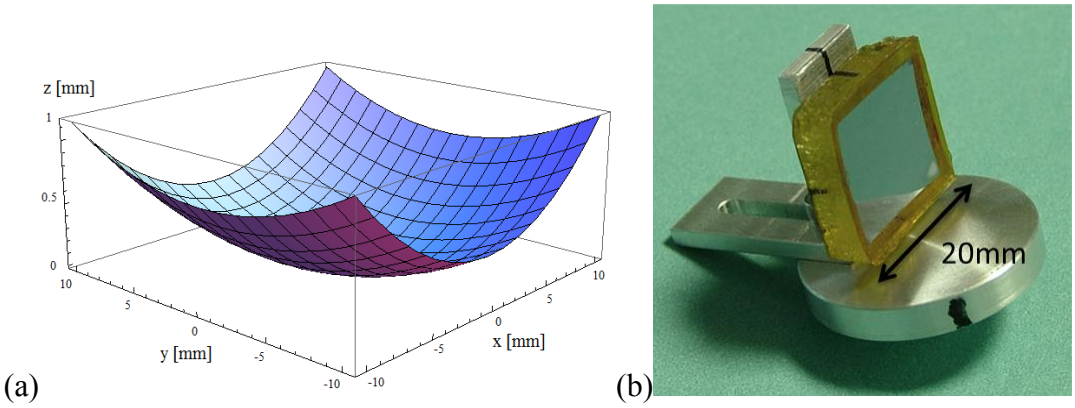

Figure 3.3 (a) Numerical surface of bent Si PA. (b) Prototype of bent Si PA. Dimesion of PA is 20×20 mm^2. Two type of PA with thickness t = 100 μm and 50 μm were fabricated.

3.3 Characterization of bent Si polarization analyzer

We characterized the bent Si analyzer in three different aspects. First, the surface feature which includes the radii of curvature and uniformity of the crystal after bending was measured. The surface profile was measured by the laser interferometer at the Metrology Lab, APS. Second, the distortion of the diffraction planes after bending, which reveals whether there are irregularities, strains or distortions in crystal lattice was measured. The crystal lattice deformations were detected by x-ray topography using 8 keV x-ray tube source with copper as the anode material at Optical Shop, APS. The last is the characterizations of the optics in synchrotron

radiation source, such as reflectivity, energy and spatial resolution at the focus. Reflection features of the optics include the local reflectivity and overall efficiency. The preliminary characterization of bent Si PA in a hard RIXS spectrometer was carried out at 9ID, APS. Energy spectrum of polarization analyzer from a plastic scatterer is presented and the polarization analyzed RIXS spectrum of Sr_2IrO_4 as well.

3.3.1 Metrology measurement

The metrology test of a curved surface is to measure altitudes (z coordinates) of each point ((x, y) coordinates) on the tested surface relevant to the principle surface (a flat surface as the reference). Then a full three dimensional profile of the tested surface is mapped out by stitching the overlapped images of all tested spots. This measurement was carried out by a laser interferometer as shown in Figure 3.4 (Assoufid *et al.*, 2007) in the Metrology Lab, APS.

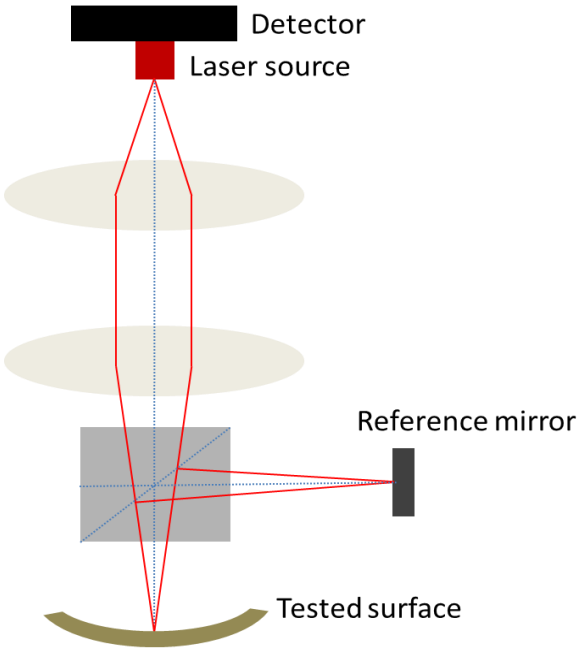

Figure 3.4 Schematic of the interferometer in Metrology lab, APS

The laser interferometer is an optical measuring instrument to obtain surface profile in three dimensional space by the principle of light interference. The incoming beam from the laser source and reflected beam from the tested surface interfere with each other with the same frequency, forming a superposition of combined waves. Each ray travels a certain distance called the light path depending on the height of the point it hits on the curved surface. The differences in traveling path create a wave phase difference between two waves, and these phase differences create an interference pattern which is captured by the detector. The in-phase waves cause constructive interference and out-of-phase waves cause destructive interference, which generate the bright and dark zones in the interference pattern, respectively.

The surface profile is the interferometric stitching of images from every spot tested. The spot size is determined by the focused source aperture on the tested surface. Each two neighboring images overlaps by a constant fraction and are numerically stitched together to generate one image. The surface profile of bent Si analyzer is shown in Figure 3.5a. Only a certain part of the surface around the center can be measured because the tested radius of curvature is small so that the interference fringes beyond the center are too tight to be analyzed by the system.

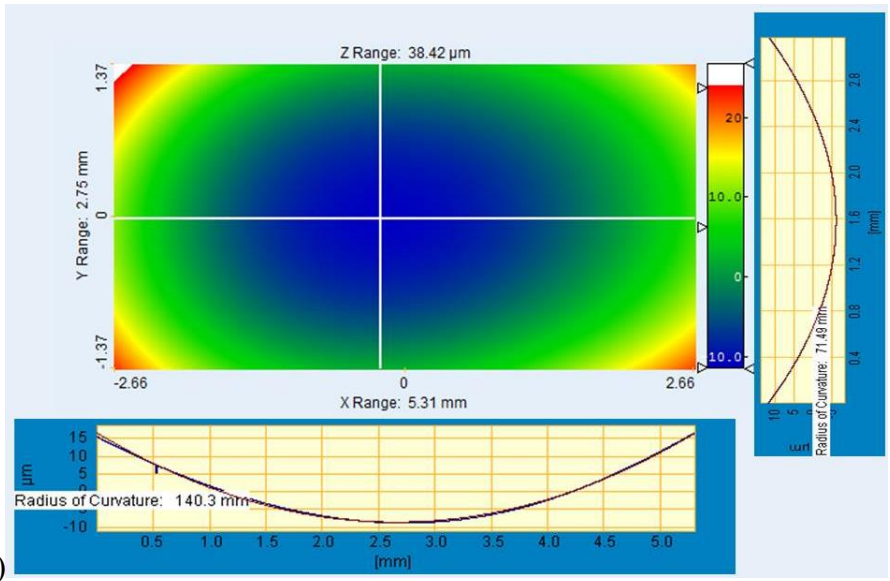

(a)

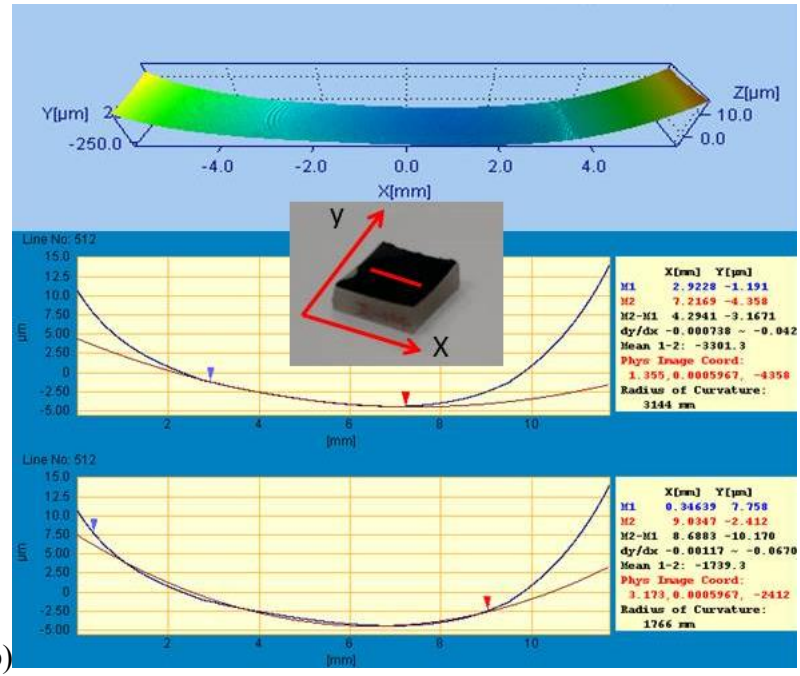

(b)

Figure 3.5 (a) Contour map of double-concave surface of bent Si PA. The tested area is 2.75 mm×5.31 mm. The color intensity represents the ampitude of z coordinates. The map is stitched by 6×12 spots with a laser spot size $(0.61\text{mm})^2$ by 30% overlapping. (b) Profile of bent crystal by conventional

pressing to a lens substrate. Central line profile indicates the radius of curvature is off by at least an order of magnitude.

Crystal surface is in a toroidal shape so the contour graph is ellipse-like. Two orthogonal center lines along the x and y axis can indicate the accuracy of the fabrication which is fitted by a circular function. The designed values for the radii are 70.52 mm and 141.8 mm. The actual radii of curvature are 71.49 mm and 140.3 mm which give an error of 1% off the designed values. This error is within the intrinsic systematic error of the equipment.

3.3.2 X-ray topography

A good quality ultra-thin Si wafer is the foundation for making a bent polarization analyzer. The bent Si analyzer is developed for hard x-ray spectroscopy, thus a measurement of the crystal surface at the atomic level is necessary rather than only restricted at a surface level. X-ray topography (XRT) (Hartmann *et al.*, 1975) is a technique to characterize microstructure of crystals by x-ray diffraction. When the crystal is at the Bragg angle, the monochromatic, parallel incident x-ray hits the sample and the diffracted beam is recorded by a 2D x-ray detector. The diffraction image can give information on crystal structure by the intensity of the diffracted beam on the detector. The image from a perfect crystal is commonly homogeneous since the diffraction profile has a same intensity everywhere on the image for a flat perfect crystal, however, if there are strains, distortions of crystal plane or imperfections inside the crystal, the area surrounding the irregularities are seen in the image with intensity contrast to the perfection diffraction (Schwuttke *et al.*, 1968).

Metrology test of the bent Si has shown a good quality of bending radii of curvature relevant to the expected values. But XRT can provide the extra information

in the lattice inside the crystal thanks to the finite penetration depth of x-rays. The XRT setup is shown in Figure 3.6. A 8 keV collimated beam generated from the asymmetric Si (2 2 0) monochromator covers the whole test surface. For testing a flat crystal, the entire beam is reflected at the Bragg angle and the reflected beam on the detector is an image about the same size of the tested crystal. However, in our case, for a curved crystal, only a tiny vicinity of Bragg angle can be reflected but the other are not reflected since the incident angles are not satisfied with Bragg condition. The topography image is obtained by rotating the crystal along Θ direction. The image is a curved line at the each Θ angle since the crystal is biaxially bent. A straight line is the image of uniaxial bending (cylindrical bending). The image shown in Figure 3.7 is the sum of all scanned Θ values which describes the whole crystal surface. The lines are uniformly contributed except the defects at the edges which mostly result from the cutting procedure.

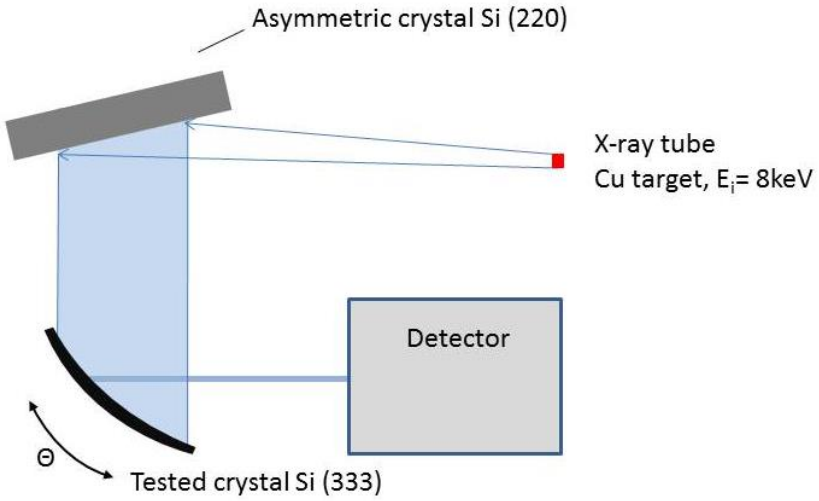

Figure 3.6 Schematic of the top view of x-ray topography with a tube source. The corresponded reflection of tested crystal is Si (3 3 3) for the incident energy of 8keV.

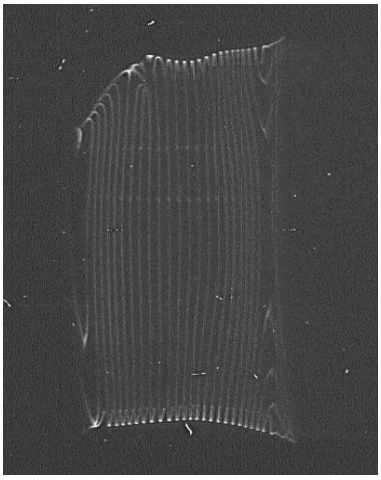

Figure 3.7 Topography image of 100μm thickness curved silicon crystal. Most area is uniformly distributed except the edges. The imperfections on the edges and upper left corner indicate the strains in the crystal due to the cutting and pressing procedures.

3.4 Preliminary test of bent Si polarization analyzer at RIXS beamline

3.4.1 Experimental setup

The RIXS setup with polarization analysis system was described as shown in Figure 2.1 in σ-σ configuration. Bent PA with a double concave shape designed for Ir L_3-edge was tested at the RIXS beamline 9ID at the APS. The experiment was carried out with σ polarization of incident x-ray with E_i = 11.215 keV in vertical scattering geometry. A double bounce Si (1 1 1) is the high heat load main monochromator and Si (3 3 3) is the high resolution secondary monochromator. The main analyzer is a

diced, etched, spherically bent (R = 1m) Si (8 4 4) crystal working at near backscattering condition. The bent Si PA is placed about 10 cm downstream from the primary focus and the detector is placed 10 cm away from the PA as well. Scattering beam from the sample is first reflected by the main analyzer down to the PA at the near backscattering Bragg angle, and then subsequently reflected by the PA with $2\theta \simeq 90°$ down to the detector. The RIXS setup with polarization analysis system is shown in Figure 3.8.

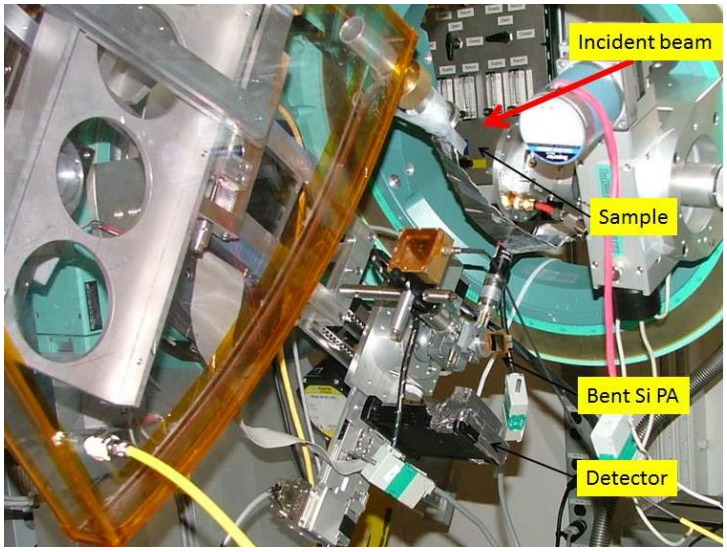

Figure 3.8 Experimental setup of RIXS with polarization analysis system at 9ID in σ-σ configuration. The main analyzer that is not shown on the picture is ~1m away from the sample position. Incident x-ray hits on the sample and scattered beam is reflected by the main analyzer to the PA and finally ends into the detector.

The pin diode detector is placed in front of PA to detect to total intensity before coming into the PA. The polarization analysis system is mounted on the detector arm of RIXS spectrometer. PA is placed on a goniometer with two rotational and two

linear motions. The goniometer is mounted on a rotational stage that aligns the theta angle of PA. There two additional linear motions to align the primary focus-PA and PA-detector distances.

3.4.2 Resolution of elastic scattering

To characterize the overall energy resolution broadening and overall efficiency of PA, one need to measure the resolution function at the primary focus in front of PA with the conventional RIXS setup, and the resolution function at the secondary focus after PA. The resolution function at the primary focus without polarization analysis system has an FWHM of 172 meV shown in blue in Figure 3.9. The FWHM of the spectrum at the secondary focus with σ polarization configuration is 246 meV which broadens the primary focus by 43%.

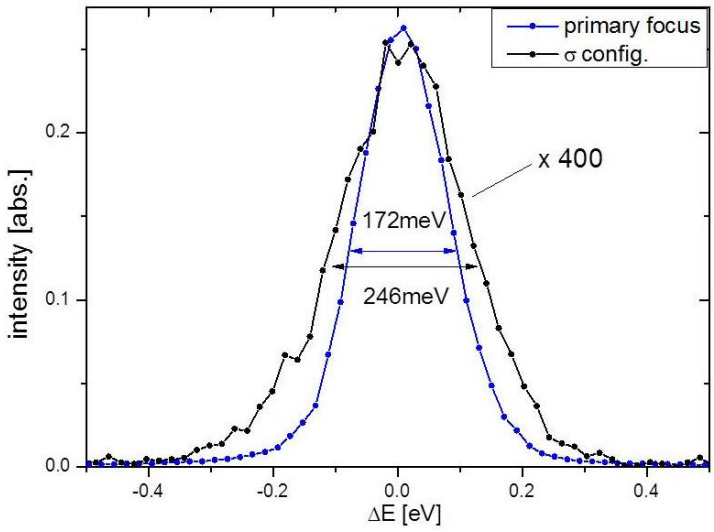

Figure 3.9 Energy resolution function at the primary focus before the PA and secondary focus after PA. Both spectra are taken with σ polarization of incident x-ray in the vertical diffraction geometry.

Overall efficiency can be estimated by the ratio of the integrated intensity at the secondary focus and the primary focus. The overall efficiency turned out to be 0.4% which is lower by an order of magnitude than the expected value. The low efficiency might come from the surface strain of the flat Si wafer due to the lapping from the manufacturer, large strain gradient inside the crystal due to strong deformation, or the intrinsic sharp acceptance due to the critical Bragg conditions ($\theta_B \simeq 45°$) of PA.

3.4.3 Polarization analyzed RIXS of Sr_2IrO_4

Polarization analyzed RIXS of Sr_2IrO_4 was measured as a first attempt. Although the efficiency of PA is not as want we expected, it shows the polarization analysis ability at least at the Ir L_3-edge because to the large elastic signal result from the direct transition at TM *L*-edge RIXS rather than the indirect process at TM *K*-edge RIXS. The energy loss spectrum of Sr_2IrO_4 at the resonant incident energy is shown in Figure 3.10. Resolution function of elastic scattering of PA is shown in black circles to make the low energy excitation outstanding.

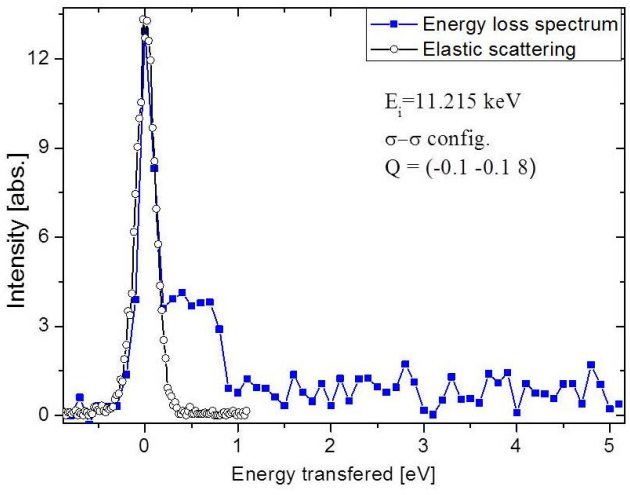

Figure 3.10 Polarization analyzed data of Sr_2IrO_4. The energy transferred spectrum compares the resolution function to elastic scattering of PA. The low energy excitation below 1eV can be detected with enough counting time.

The low energy excitation in this compound is related to exotic magnetic behavior explained by the $J_{eff} = 1/2$ ground state under strong spin-orbital coupling (Kim *et al.*, 2008). The PA shows its potentials to detect and analyze the low energy excitations for the Ir L_3-edge RIXS. More polarization analyzed measurements need to be carried out to deeply study the magnetic excitations such as momentum dispersion, temperature dependence, etc. Complete simulation to analyze the causes of the low efficiency requires information of Bragg condition (strongly depending on the d-spacing variation) at each local reciprocal lattice point which can be solved by finite-element analysis (Sutter *et al.*, 2008) and modified Bragg law from a bent crystal (Tchen, 2003). Improving the bent Si PA to achieve higher efficiency will be carried out in future work.

CHAPTER 4

IRIDIUM COMPOUNDS

In the previous chapter, a polarization analysis system with HOPG PA designed for Cu *K*-edge hard RIXS and bent Si PA designed for Ir L_3-edge RIXS were presented to study the outgoing polarization in correlated systems. *L*-edge hard RIXS is a powerful technique to study the magnetic excitations in the low energy region in contrast with *K*-edge RIXS. The low energy *L*-edge inelastic signal is typically 10~100 times (100~300 c/s) of *K*-edge RIXS which is due to the direct transition of *L*-edge RIXS rather than the indirect RIXS process in *K*-edge RIXS and the small elastic line in the near 90° horizontal scattering configuration (Kim *et al.*, 2012c). The magnetic excitations in the 5*d* system Sr_2IrO_4 were measured by Ir L_3-edge RIXS to have dispersing features spread out the entire Brillouin zone which is explained by the splitting $J_{\text{eff}} = 1/2$ and $J_{\text{eff}} = 3/2$ coupling states under strong spin-orbital coupling (Kim *et al.*, 2009). The effective RIXS matrix for magnetic excitations is strongly polarization dependent (both incident and outgoing polarizations) (Hannon *et al.*, 1988). The interesting physics in iridium systems and the sufficient count rates encouraged us to develop the polarization analysis system.

In this chapter, the physics related to the magnetic excitations in the 5*d* system such as magnon, spin-orbit coupling, crystal field, etc. are presented for understanding the background of the system of interest. 5*d* systems studied by Ir L_3-edge RIXS without polarization analysis, including the 2D layer system Sr_2IrO_4 and the quasi-1D system $BaIrO_3$ are introduced.

4.1 Theoretical basis

In this section, some elementary theoretical terms in solid state physics, magnetism behavior, and interaction between spin and orbital angular momentum, etc. are introduced. Only key items strongly related to the crystals that we focus on are presented, more can be found in the references.

4.1.1 Spin-orbital interaction

The spin–orbit interaction is also called spin–orbit coupling because it involves the electron spin and orbital degrees of freedom. An electron moving in a certain orbital relative to the nucleus creates a magnetic field which couples to the electron's spin. The spin-orbit interaction has the form of $E_{so} = \lambda \mathbf{L} \cdot \mathbf{S}$, which couples the total angular momentum **L** and total spin **S** of the electrons of an atom (Alloul, 2011). It is an important degree of freedom in condensed matter physics, which can cause a lifting of energy levels in atoms of solids, therefore affecting many properties such as metal-insulator phase transition, magnetism and superconductivity, etc.

An electron moving around a nucleus with a charge *Ze* (*e* is positive) would experience an electric potential field described by classical electrodynamics,

$$V(r) = \frac{Ze}{4\pi\varepsilon_0} \cdot \frac{1}{r} \tag{4.1}$$

where *r* is the orbital radius. The associated electric field **E** is the gradient of the electric potential and is spherical symmetric,

$$\mathbf{E} = -\nabla V = -\frac{\partial V}{\partial r} = \frac{Ze}{4\pi\varepsilon_0} \cdot \frac{1}{r^2} \hat{\mathbf{r}} \tag{4.2}$$

The magnetic field generated as the electron travels through the electric field is:

$$\mathbf{B} = \frac{-\mathbf{v} \times \mathbf{E}}{C^2} \tag{4.3}$$

From classical mechanics, the angular momentum is the cross product of position vector and linear momentum of a particle:

$$\mathbf{L} = \mathbf{r} \times m\mathbf{v} \tag{4.4}$$

Substituting the angular momentum and electric field to the magnetic field, the expression of becomes:

$$\mathbf{B} = \frac{Ze}{4\pi\varepsilon_0 mc^2 r^3}\mathbf{L} \tag{4.5}$$

It is easy to see that the magnetic field is in the same direction as the angular momentum and perpendicular to the electron's velocity. The total spin-orbit Hamiltonian is the interaction of the magnetic moment and the magnetic field it lies in:

$$H_{SO} = -\frac{1}{2}\boldsymbol{\mu} \cdot \mathbf{B} \tag{4.6}$$

The factor of 1/2 is known as the Thomas half, which is the reduction of the Larmor interaction energy. The magnetic moment connected with the spin is:

$$\boldsymbol{\mu} = g_e \frac{-e}{2m}\mathbf{S} \cong \frac{-e}{m}\mathbf{S} \tag{4.7}$$

Here the g_e is so called g-factor of electron, $g_e \approx 2$ is a dimensionless constant.

Therefore we obtain the spin-orbit Hamiltonian:

$$H_{SO} = \frac{Ze^2}{8\pi\varepsilon_0 m^2 c^2}\frac{1}{r^3}\mathbf{S} \cdot \mathbf{L} \tag{4.8}$$

The total momentum operator is the sum of angular momentum operator and spin operator $\mathbf{J} = \mathbf{L} + \mathbf{S}$, and $\mathbf{J}^2 = \mathbf{L}^2 + \mathbf{S}^2 + 2\mathbf{L}\cdot\mathbf{S}$ ($\mathbf{L}$ and $\mathbf{S}$ commute). It is known that $\mathbf{J}$,

$\mathbf{J}^2$, $\mathbf{L}^2$, and $\mathbf{S}^2$, commute with each other and all commute with spin-orbit Hamiltonian H_{SO}. The expectation value of $1/r^3$ for the hydrogen wave function is:

$$\left\langle \frac{1}{r^3} \right\rangle = \frac{Z^3}{l\left(l+1/2\right)\left(l+1\right)\mathrm{n}^3\mathrm{a}^3} \tag{4.9}$$

where a is the Bohr radius divided by the atomic number Z. And the expectation value of $\mathbf{L}\cdot\mathbf{S}$ is:

$$\begin{aligned} \langle L\cdot S\rangle &= \frac{1}{2}\left[\left\langle \mathbf{J}^2\right\rangle - \left\langle \mathbf{L}^2\right\rangle - \left\langle \mathbf{S}^2\right\rangle\right] \\ &= \frac{\hbar^2}{2}\left[\, j\left(j+1\right) - l\left(l+1\right) - s\left(s+1\right)\right] \end{aligned} \tag{4.10}$$

Therefore the energy splitting due to the spin-orbital coupling is(Korneta, 2012):

$$\begin{aligned} \mathrm{E_{SO}} &= \frac{\mathrm{Z}e^2}{8\pi\varepsilon_0 m^2c^2}\left\langle \frac{1}{r^3}\right\rangle \langle L\cdot S\rangle \\ &= \frac{\mathrm{Z}^4e^2}{8\pi\varepsilon_0 m^2c^2}\left[\frac{(\hbar^2/2)\left[\, j(j+1) - l(l+1) - s(s+1)\right]}{l(l+1/2)(l+1)n^3a^3}\right] \end{aligned} \tag{4.11}$$

All these are under assumption of only considering the internal magnetic field that is associated to electrons orbitals. When a non-negligible external magnetic field exists, the energy splitting is then explained by the Zeeman effect (Schiff *et al.*, 1939). The Zeeman effect describes the coupling between the electron's angular moment or both angular and spin moment under the weak external magnetic field (if both are considered, it is called the anomalous Zeeman effect). If both orbit and spin are involved, the quantized energy splitting has the form of:

$$\Delta\mathrm{E} = \frac{\mathrm{e}}{\mathrm{m}}\left(\mathbf{L}+\mathbf{S}\right)\cdot\mathbf{B} = g_L\mu_B m_j B \tag{4.12}$$

where B is the external magnetic field, $\mathrm{g_L}$ is the Landé g-factor and $\mathrm{m_j}$ is the z-component of the total momentum of **J**. As a strong field is applied, the angular

momentum and spin moment independently couple to the magnetic field and the spin-orbit coupling is disrupted, which is called Paschen-Back effect.

4.1.2 Hund rules

In a multi-electron atom, when the total number of electrons equals to the available orbit levels which are restricted by the Pauli exclusion principle, all the lowest energy levels are fully filled by the electrons with different spin and orbital magnetic quantum numbers. The total orbital L and spin S are equal to zero. For partially filled shells of multi-electron atoms where the number of electrons are less than the available levels, the atomic ground state are occupied by the electrons by a set of rules which are called Hund Rules (Engel *et al.*, 2006; Miessler *et al.*, 1999).These rules are:

1. The ground states are filled with maximal total spin S.
2. The ground states are filled with maximal orbital angular momentum L.
3. The total angular momentum J depends on how the shell is filled:

   $J = |L - S|$, if the shell is less than half filled.

   $J = |L + S|$, if the shell is more than half filled.

   $J = S$ (L=0), if the shell is half filled

To explain rules 1~3, an example of the case of d shell electrons is shown in Table 4.1. For atomic d orbital, the orbital quantum number l = 2. For different magnetic quantum numbers m_l, l_z ranges from -2 to 2. To satisfy to the 1st rule Hund rules, the electron is put to be spin up ↑ respectively instead of spin down ↓ to reach the maximum of total spin S. After half of the saturated number of electrons, electrons with spin ↓ are allocated from the maximum l_z value to reach the maximal of total orbital momentum L, obeying the 2nd rule of Hund rules. Hund rules indicate that the

total momentum of the half-filled shell is zero and total momentum is purely due to the spin; the total angular and spin momentum are both zero for the fully filled shell.

Table 4.1

Ground state of d shell filled by different number of electrons, n is the total number of electrons, l_z is the z component of the orbital angular momentum of an electron, L is the total orbital momentum, S is the total spin momentum, and J is the total angular momentum (Alloul, 2011).

n	$l_z = 2$	1	0	-1	-2	S	L	J
1	↑					1/2	2	3/2
2	↑	↑				1	3	2
3	↑	↑	↑			3/2	3	3/2
4	↑	↑	↑	↑		2	2	0
5	↑	↑	↑	↑	↑	5/2	0	5/2
6	↑ ↓	↑	↑	↑	↑	2	2	4
7	↑ ↓	↑ ↓	↑	↑	↑	3/2	3	9/2
8	↑ ↓	↑ ↓	↑ ↓	↑	↑	1	3	4
9	↑ ↓	↑ ↓	↑ ↓	↑ ↓	↑	1/2	2	5/2
10	↑ ↓	↑ ↓	↑ ↓	↑ ↓	↑ ↓	0	0	0

Hund Rules are based on the Coulomb interaction between the electrons and the Pauli principle so that two electrons desire to be in different orbits due to Coulomb repulsion and once each orbit are occupied, electrons are in the same orbit with antiparallel spins. This is the case of free ion, and the case of weak field applied by other ligands surrounding ion. In the case of ion under strong crystal field (see 4.1.3), electrons occupancy will not follow Hund Rules, they prefer to doubly occupy the low energy orbitals before filling the higher orbitals.

4.1.3 Crystal field in solids

In transition metal oxides, there are many physics properties, e.g. magnetic

4.1.3 Crystal field in solids

In transition metal oxides, there are many physics properties, e.g. magnetic properties, etc. effected by the crystal field. As its name, the crystal field describes how the energy levels degeneracy of an atom are modified due to the electric field produced by the surrounding environment (anion neighbors, e.g. O^{2-}) in the crystal. In many transition metal oxides, the interaction between electrons in *d*-orbitals of the metal ion and its surrounding electron cloud from *p*-orbitals of the O^{2-}s causes the energy lifting or lowering, thus changes the degenerate energy levels of the cation. Electrons closer to the anions will have higher energy than the ones further to the anions. Figure 4.1 shows the electron d and p orbital distribution symmetry.

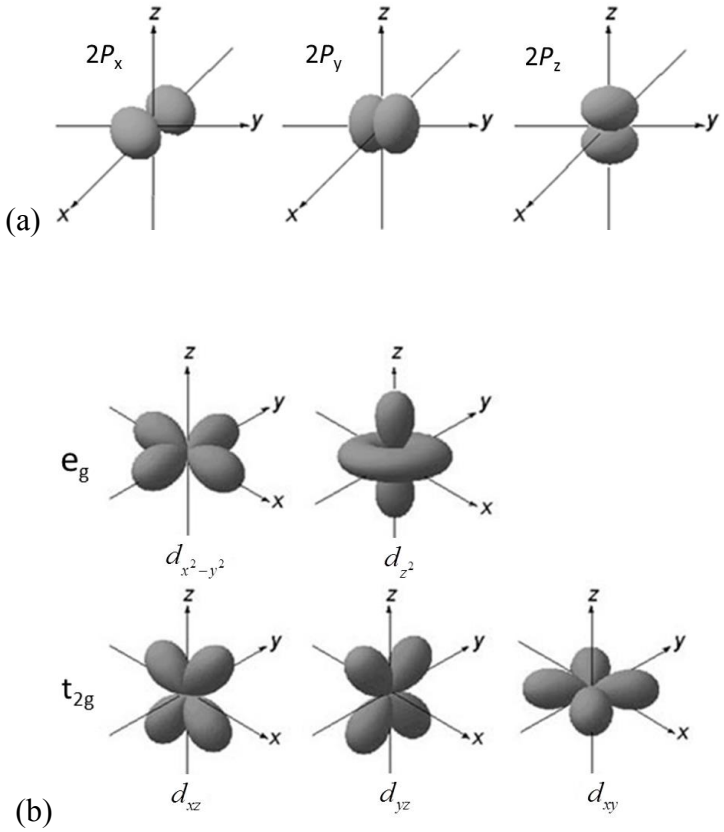

Figure 4.1 (a) 2*p* orbital symmetry. (b) 3*d* orbital symmetry.

A common case is in the octahedral structure (e.g. 2D-layered system Sr_2IrO_4), where the cation is at the center of the octahedron with *d* electrons and surrounded by six anions at each corner with *p* electrons. *d*-orbits of the metal ion split the free ion energy level into two set of degenerate levels called e_g and t_{2g} (defined by the group theory symmetry), respectively. The two levels differ by an energy Δ_o. d_{xy}, d_{xz} and d_{yz} orbitals are lower in energy than the d_z^2 and $d_{x^2-y^2}$ shown in Figure 4.2.

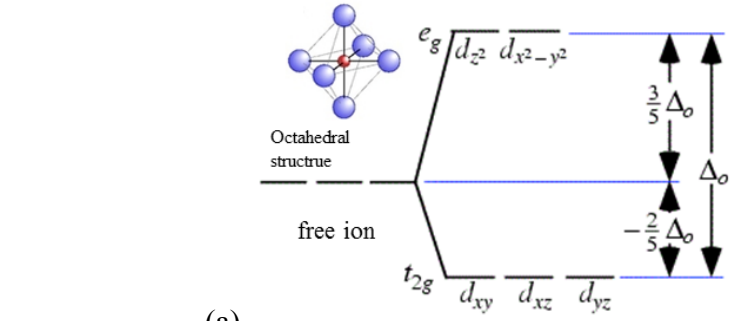

(a)

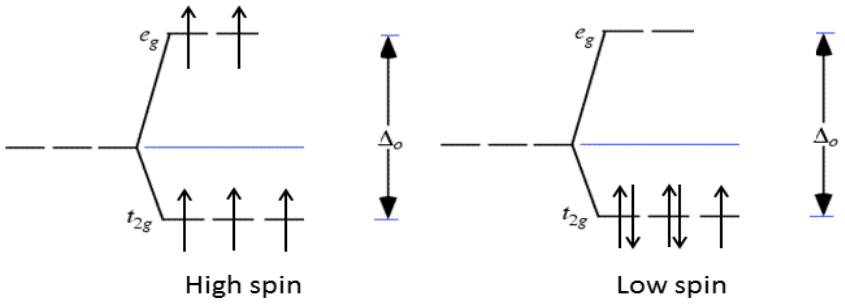

(b)

Figure 4.2 (a) crystal field splitting of octahedral crystal. (b) High spin and low spin diagram, for d^5 state.

The crystal field splitting is strongly related to the local environment of the cation,

e.g. the type of anion, and ionized states, crystal structure of the anion and cation. Different arrangement will cause a different splitting, for instance, the tetrahedral splitting is inverse to the octahedral, leading to a two-fold e_g state with lower energy and three-fold t_{2g} states with higher energy. The arrangement of electrons spins also depends on the effect of the crystal field. Under weak crystal field, electrons occupy the orbitals following the Hund Rules (high spin case, shown in Figure 4.2b); under strong crystal field, electrons are likely to doubly occupy the lowest orbitals instead of reaching high energy orbitals due to the large value of Δ_o (Korneta, 2012). The degeneracies of *d*- orbitals and splitting diagram are not only effected by the crystal field, they are strongly related to the surrounding environment of the metal ion and it can be removed under some external conditions such as pressure, crystal distortion, etc. For instance, when the octahedron is under z-uniaxial compression, the energy level of $d_{x^2-y^2}$ of e_g and d_{xy} of t_{2g} is lowered causing a shortening of the bonds on the xy plane and elongating of the bond along the z-axis, which is called Jahn-Teller distortion or Jahn-Teller effect (Jahn *et al.*, 1937). This effect occurs often in octahedral compound with odd number *d*-electrons on the e_g orbitals.

4.1.4 Exchange interaction

The magnetic properties of material are quantum effects from the interactions between the electron spins which is the origin of the magnetic ordering. The exchange interaction arises due to the Coulomb interactions between electrons from the overlap of their wavefunctions combined with Pauli exclusion principle (Alloul, 2011). The direct exchange interaction from the nearest neighboring magnetic ions can be described by Heisenberg model (Wolfgang Nolting *et al.*, 2010). Two particles are at the coordinates $\mathbf{r}_1$, $\mathbf{r}_2$ with wavefunction $\phi_a(\mathbf{r}_1)$ and $\phi_b(\mathbf{r}_2)$. The total wavefunction ψ_+,

ψ_- with symmetry and antisymmetry is presenting the singlet (total spin S=0) and triplet (S=1), respectively. The singlet ψ_+ and triplet ψ_- are given by:

$$\psi_+ = \frac{1}{\sqrt{2}}\left[\phi_a(\mathbf{r}_1)\phi_b(\mathbf{r}_2) + \phi_a(\mathbf{r}_2)\phi_b(\mathbf{r}_1)\right]$$
$$\psi_- = \frac{1}{\sqrt{2}}\left[\phi_a(\mathbf{r}_1)\phi_b(\mathbf{r}_2) - \phi_a(\mathbf{r}_2)\phi_b(\mathbf{r}_1)\right] \quad (4.13)$$

The eigenvalue of the state are E_+ and E_- and the exchange integral J has the form of:

$$J = \frac{E_+ - E_-}{2} = \int \phi_a^*(\mathbf{r}_1)\phi_b^*(\mathbf{r}_2)\hat{H}\phi_a(\mathbf{r}_2)\phi_b(\mathbf{r}_1)d\mathbf{r}_1 d\mathbf{r}_2 \quad (4.14)$$

Then the Heisenberg exchange interaction Hamiltonian with the spin of two particles $\mathbf{S}_1$ and $\mathbf{S}_2$ can be written as:

$$\mathrm{H}_{\mathrm{Heisen}}^{(\text{single pair})} = -2\mathrm{J}\mathbf{S}_1 \cdot \mathbf{S}_2 \quad (4.15)$$

And the total Heisenberg Hamiltonian is the sum of all pair of magnetic moment:

$$\mathrm{H}_{\mathrm{Heisen}} = -\sum_{\mathrm{i,j}} \mathrm{J}\vec{\mathrm{S}}_{\mathrm{i}} \cdot \vec{\mathrm{S}}_{\mathrm{j}} \quad (4.16)$$

where *J* is the exchange constant between the *i*th and *j*th spins and a factor of 1/2 is in front since each site counted twice in the sum. Positive *J* corresponds to $E_+ > E_-$ where the lower energy E_- triplet state is favored corresponding ferromagnetism (parallel spins), and negative *J* corresponding to the lower energy E_+ singlet state is favored corresponding antiferromagnetism (antiparallel spins). Some cases such as in oxides the coupling is not between the nearest neighboring magnetic ions but bridged through oxygen, forming a "cation-anion-cation" indirect exchange interaction that is called superexchange originated from the overlapping between the cation and anion (Korneta, 2012). For example, in Sr_2IrO_4 the antiferromagnetic ordering is dominated by the Ir-O-Ir superexchange bond. The superexchange strongly depends on the orbitals, bond types and bond angles, itinerant electron environment, etc. of the cation and anion forming complex long-range magnetic orders that can be explained by

different models.

4.2 2D layered system Sr_2IrO_4

4.2.1 Crystal and electron structure of Sr_2IrO_4

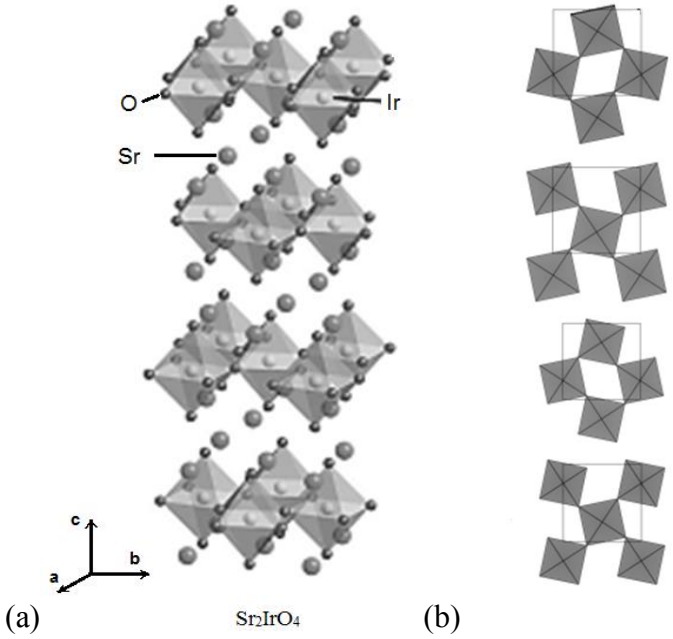

Figure 4.3 (a) Structure of unit cell of Sr_2IrO_4, which includes 4 layers of IrO6 octahedrons due to the elongation along c-axis. (b) IrO_6 octahedra in each layer. The rectangular outline is the unit cell projection on the a-b plane. Shaded areas are IrO_6 octahedrons projections. (Kim *et al.*, 2012b)

Sr_2IrO_4 has a layered perovskite tetragonal crystal structure defined to the space group of $I4_1/acd$ with lattice parameters a = b = 5.4979(2) Å and c = 25.798(1) Å at ambient temperature (Crawford *et al.*, 1994). Each layer consists of IrO_6 octahedrons which rotate about the c-axis by ~11° relevant to the unit cell outline due

to the Jahn-Teller distortion and elongates the unit formula along the c-axis to be about 4 times larger than a-axis as shown in Figure 4.3b, forming a superlattice structure. The Ir^{4+} ions have a $5d^5$ electron configuration with low spin state under the large crystal field and strong spin-orbit coupling. Five electrons in the 5*d* state accommodate the triply degenerated t_{2g} states by the fully occupied d_{yz}, d_{xz} orbitals and the half-filled d_{xy} orbital (Crawford *et al.*, 1994; Kim *et al.*, 2009). Sr_2IrO_4 is unexpectedly an Mott insulator rather than a metallic state as seen in the $4d^5$ compound Sr_2RhO_4 which has the same crystal structure (Kim *et al.*, 2008). This unusual insulating behavior attracted significant attention.

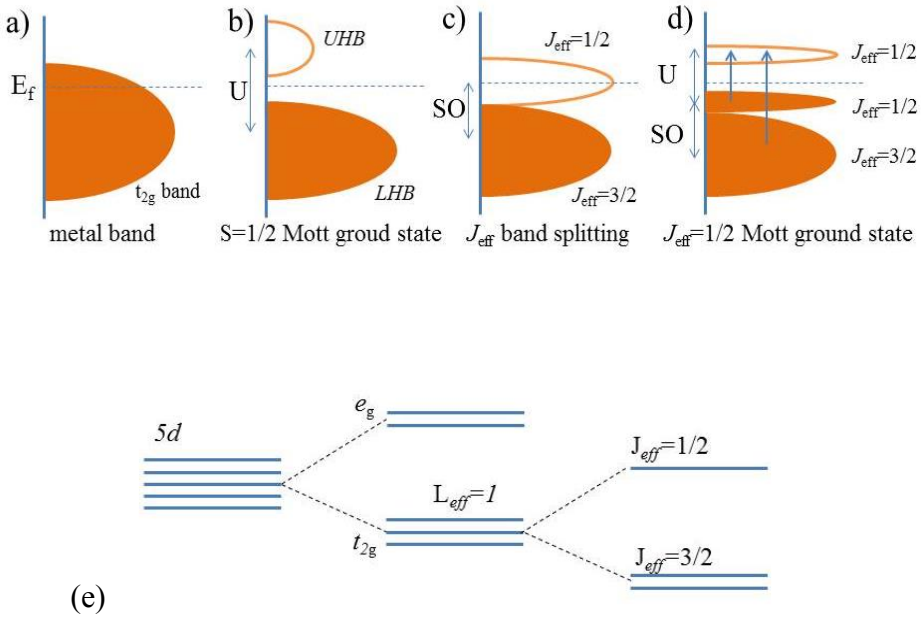

Figure 4.4 t_{2g} band configuration. The Fermi level E_f , Coulomb interaction U, and spin-orbital coupling SO are indicated. (a) Metallic band without U and SO. (b) Mott ground state with only U. (c) J_{eff} band with only SO. (d) J_{eff} band with both U and SO.(e) crystal field splitting under spin-orbital coupling. (Kim *et al.*, 2008)

Considering the strong spin-orbital coupling (~0.4eV) and large crystal field when the spin and orbit are not separately good quantum numbers, the three-folded t_{2g} state is explained by the effective total angular momentum J_{eff}, as shown in Figure 4.4. t_{2g} state corresponds to an effective orbital momentum L_{eff} = 1 with state $\phi_{l=\pm1} = \mp\sqrt{2}^{-1}(|zx\rangle + i|yz\rangle)$ and $\phi_{l=0} = |xy\rangle$ which correspond the effective total angular momentum J_{eff} = 3/2 four-fold degenerated states and J_{eff} = 1/2 two-fold degenerated states shown in Figure 4.4e (Jackeli *et al.*, 2009; Kim *et al.*, 2008). The J_{eff} = 3/2 bands are full filled and the J_{eff} = 1/2 are half filled forming the compound a J_{eff} = 1/2 Mott insulating ground state with a gap opened by a small Coulomb repulsion. In 2D IrO_2 layer, Sr_2IrO_4 shows a weak ferromagnetic behavior (ferromagnetic moments = $0.14\mu_B$/Ir) contributed by the canted antiferromagnetic order due to the in-plane rotation of IrO_6 octahedrons (Crawford *et al.*, 1994) below T_N = 240K (Cao *et al.*, 1998).

4.2.2 RIXS of Sr_2IrO_4

Electronic excitations. RIXS as powerful technique is a direct probe of the 5*d* band structures by giving information on the electronic excitations, and even the magnetic excitations in the lower energy region thanks to the recent improvement of RIXS spectrometers. As shown in Figure 4.5, a RIXS spectrum covering the large energy region shows the interband transition (in t_{2g} states) across the Mott gap to the upper J_{eff} = 1/2 band (0.5, 3.2eV peak), and charge transfer excitations at (6.0eV peak) from the O 2p band to the Ir 5*d* band (e_g $3z^2$-r^2 state) (Cetin, 2012). The modes of the Mott gap excitation show a weak dispersion, which is interpreted by the presence of the narrow 5*d* bands of the novel Mott insulating state of Sr_2IrO_4 induced by the strong spin-orbit interaction (Ishii *et al.*, 2011c).

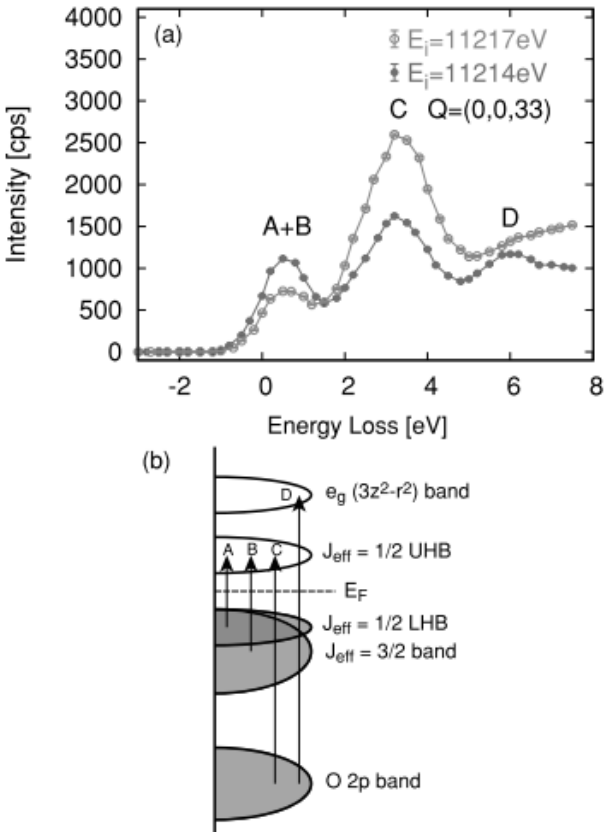

Figure 4.5 (a) RIXS spectra of Sr_2IrO_4 with reduced elastic scattering. (b) Schematic transitions correspond to the inelastic peaks in RIXS spectrum (Ishii *et al.*, 2011c).

4.2.3 Magnetic excitations in Sr_2IrO_4

Magnetic excitations. A recent RIXS study of Sr_2IrO_4 by Kim *et al*. shows low energy excitations (0.2 ~ 0.8eV) with a very strong dispersion, as shown in Figure 4.6. The 0.4~0.8eV excitation with strong momentum dependence is assigned to be a "spin-orbit exciton" in the hole representation propagating (hole hopping between different sites across the spin-orbital splitting) in the antiferromagnetic ordering background, which is consistent with energy scale of the transition across the Mott

gap from optical spectroscopy (Moon *et al.*, 2009). This spin-orbit exciton is not present in cuprates. The low energy excitations at less than 200meV are believed to be single magnon excitations with strong momentum dependence similar to the single magnon dispersion observed in cuprates, which is supported by the theory of superexchange interaction of $J_{\text{eff}} = 1/2$ moments on a corner-shared octahedral in canted antiferromagnetic ordering (Wang *et al.*, 2011). The magnon dispersion is well fitted by a $J - J' - J''$ model (Coldea *et al.*, 2001) considering the higher-order spin exchange couplings in Heisenberg Hamiltonian with $J = 60$ meV, $J' = -20$ meV, $J'' = 15$ meV, where J, J', J'' are the first, second and third nearest magnetic neighboring ions.

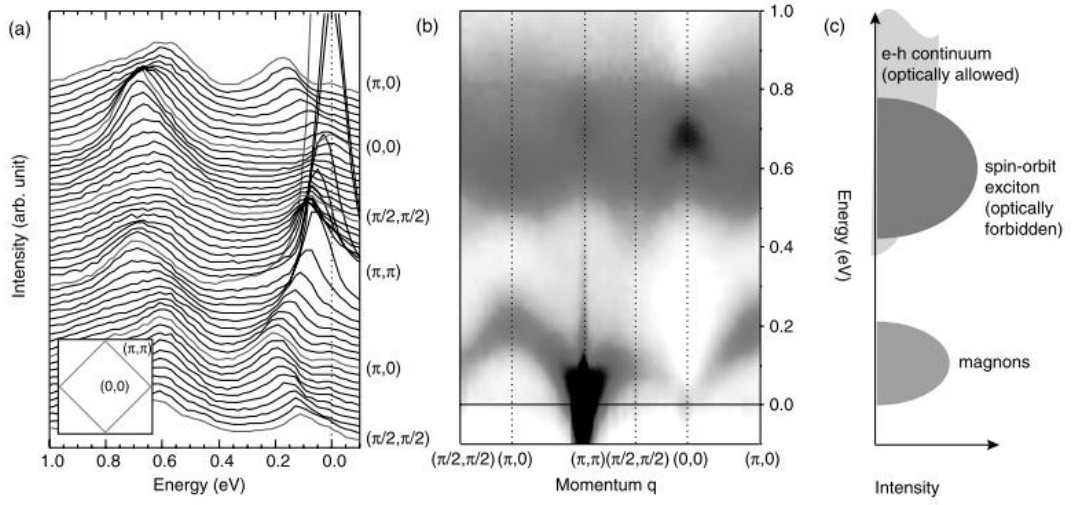

Figure 4.6 (a) Energy loss spectra recorded at T=15 K (b) image plot (c) Schematic of the three representative features in the data. Adopted from (Kim *et al.*, 2012b).

The spin-orbit exciton and magnon with strong dispersion make Sr_2IrO_4 a novel potential candidate as a superconducting parent compound as similar dynamics seen

in cuprates which may be driven to a hole or electron doped mechanism with high temperature superconductivity (HTSC) although superconductivity has not been reported. Some experiments have begun to map the phase diagram of doped Sr_2IrO_4 (Korneta *et al.*, 2010).

The magnetic excitation was proved to be strongly incident and outgoing polarization dependent in Chapter 1, even the inter-band transition (t_{2g} transition, in Sr_2IrO_4) coupled with the electron orbitals can be revealed by the symmetry information gathered from polarization analysis. The polarization analysis system based on the bent Si PA designed for Ir *L*-edge was tested and we obtained one polarization analyzed RIXS spectrum of Sr_2IrO_4 as a first attempt shown in Figure 3.10. Even though the count rate with polarization analysis is low, the inelastic signal in low energy region can be detected. More spectra at different momentum transferred over the Brillouin zone need to be mapped out to present the features of magnon.

4.3 quasi-1D system $BaIrO_3$

4.3.1 Crystal structure of $BaIrO_3$

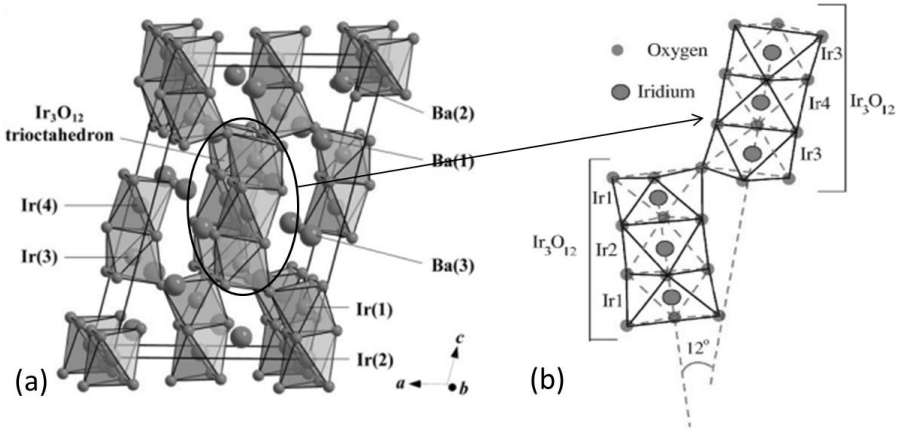

Figure 4.7 (a) schematic unit cell of $BaIrO_3$ (Zhao *et al.*, 2008). (b) Two neighboring Ir_3O_{12} trimers are corner sharing (Maiti, 2006).

Quasi-1D system. In ambient condition, the crystal structure of $BaIrO_3$ is monoclinic with a space group of C2/m. An ordinary perovskite structure is difficult to form in this compound since the large ionic radius of Ba atom makes the tolerance factor (t>1) exceed the perovskite structure boundary in ABO_3 systems (Li *et al.*, 2004). The unit cell parameters are a = 10.005 Å, b = 5.751 Å, c=15.174 Å, and β = 103.274° (Gulino *et al.*, 1995; Powell *et al.*, 1993a; Siegrist *et al.*, 1991). As shown in Fig.7.1b, the low dimensional lattice structure of $BaIrO_3$ is constructed by Ir_3O_{12} trimers. In quasi-1D symmetry, each unit cell consists of two trimers where the two neighboring trimers are tilted by 12° forming so called one-dimensional 'zigzag' chains along the crystal c-axis. There are four types of nonequivalent Ir atoms presented by Ir1, Ir2, Ir3, Ir4, defined by the way each IrO_6 octahedron connects to its neighbors. Each Ir_3O_{12} trimer has three IrO_6 octahedra units and two nonequivalent Ir sites. In one trimer, the central octahedron connects its two neighboring units by face-sharing. Between two Ir_3O_{12} trimers, the bottom octahedron (Ir3 site) and top octahedron (Ir 1 site) connect by face-sharing.

4.3.2 Magnetic and electron structure of $BaIrO_3$

The electronic and magnetic properties of $BaIrO_3$ have been studied by several experimental methods and indicate interesting behavior in the material. The ferromagnetic transition at the Curie Temperature T_c=175K is accompanied by charge density wave formation, which is often observed in 1D crystals (Cao *et al.*, 2000) as shown in Figure 4.8. The magnetic ordering is ferromagnetic below T_c and transforms to paramagnetic order in a metallic phase above T_c (Powell *et al.*, 1993b), but it is

referred to as a "bad metal", behaving like an insulator(Cheng *et al.*, 2009) since the anisotropic resistivity increases as the temperature decreases as shown in Figure 4.8. $BaIrO_3$ is found to be nonmetallic weakly ferromagnetic (Laguna-Marco *et al.*, 2010) but behaves as weakly localized metal above T_c based on the tight bending calculation by Wangbo *et al*. (Whangbo *et al.*, 2001). More recent studies of $BaIrO_3$ pointed out the strong spin-orbit interaction cannot be ignored in Ir 5*d* system as demonstrated by x-ray absorption spectroscopy (XAS) and x-ray magnetic circular dichroism (XMCD) measurements (Laguna-Marco *et al.*, 2010). The quasi-1D 5*d* Ir system is also established to be an exotic spin-orbital Mott insulator with splitting $J_{\text{eff}} = 1/2$ states and $J_{\text{eff}} = 3/2$ states under both spin-orbital coupling and on-site Coulomb interaction, similar to Sr_2IrO_4, but with stronger nearest- and second nearest-neighboring interaction due to the closer Ir-Ir bond between the face-sharing IrO_6 octahedrons rather than the corner-sharing ones in Sr_2IrO_4 (Ju *et al.*, 2013).

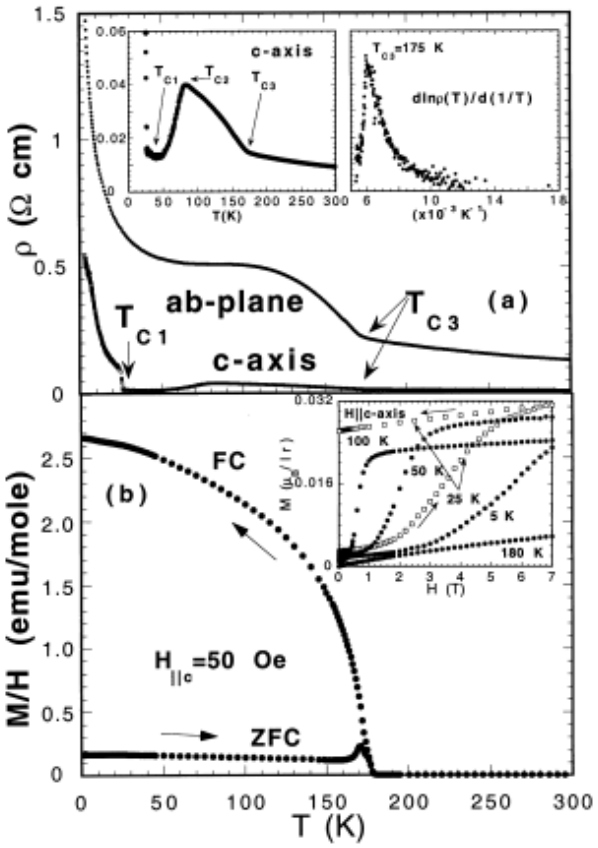

Figure 4.8 Electrical resistivity and magnetization vs temperature of $BaIrO_3$ in crystal ab-plane and along c-axis (Cao *et al.*, 2000).

4.3.3 RIXS of $BaIrO_3$

A RIXS experiment on $BaIrO_3$ was carried out on 9ID at the APS in the near 90° horizontal geometry with the incident polarization in the scattering plane. The size of the incident beam was narrowed by utilizing a secondary focusing mirror system with focused beam spot (15 vertical × 30 horizontal μm^2) on the sample. The overall resolution with a diced, spherically bent Si (8 4 4) analyzer and a strip detector turned out to be ~30 meV, which is sufficient to study the low energy features that are

usually dominated by the tail of the elastic scattering. $BaIrO_3$ was aligned with incident polarization in the crystal ac-plane to conveniently access the chain c-axis. We measured the RIXS spectra of $BaIrO_3$ only focusing on the low energy region due to time limitations and the reduced count rate from focusing mirror system. RIXS data from sample was taken at the room temperature T = 300 K. And the sample temperature was cooled down to T = 100 K across the first critical temperature T_c = 180 K, the excitation at low energy region appeared and softened at the T = 7 K across the second critical temperature (T = 80 K). Lattice parameters shrink as the temperature decreases as well as the angle between crystal a-axis and c-axis, which required realignment of the sample orientation. Then the spectra were taken as the sample temperature was increased back to T = 100 K and room temperature.

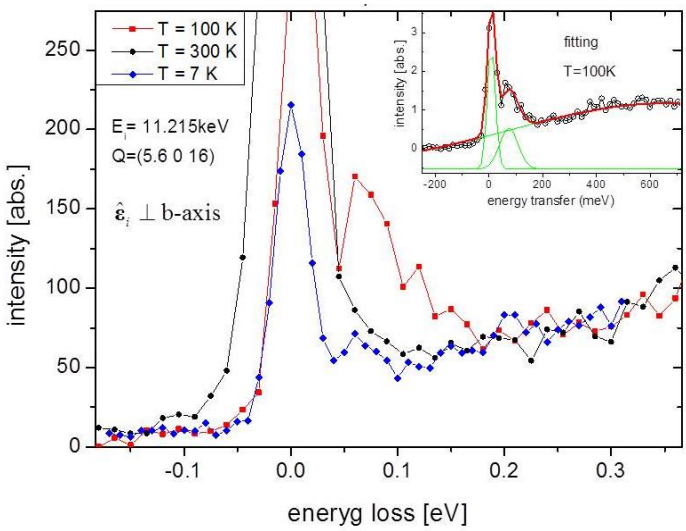

Figure 4.9 RIXS spectra of $BaIrO_3$ taken at T = 300, 100, and 7K. Insertion is the multiple peaks fitting with the elastic peak, 80 meV and 600 meV inelastic peak.

A low energy excitation below 100 meV was detected with highest intensity at T =

100K and soften at T = 7K as shown in Figure 4.9. This energy scale is hard to probe due to the elastic scattering. This 70 meV excitation is close to the soft gap opening (25 ~ 50 meV) at the Fermi level due to the localized electronic states by the lattice distortion described in (Cheng *et al.*, 2009; Maiti *et al.*, 2005). This low energy feature shown in Figure 4.10b and the high energy excitation (0.4 ~ 0.8 eV) shown in Figure 4.10a do not show significant dispersions at different positions in the Brillouin zone. The low energy excitation appeared as the temperature decreased from T = 300 K to T = 100 K, and the spectrum weight reduced at T = 7 K. The excitation did not appear as the temperature increased to T = 100 K from T = 7 K. It is valuable to measure the lattice parameters as a function of temperature by x-ray diffraction since incorrect parameters can cause sample missing orientation. Beam might hit sample on bad area as the temperature changes. About a half of the crystal surface is not in good quality seen in the microscope. A small crystal with good quality can stabilize the experimental conditions.

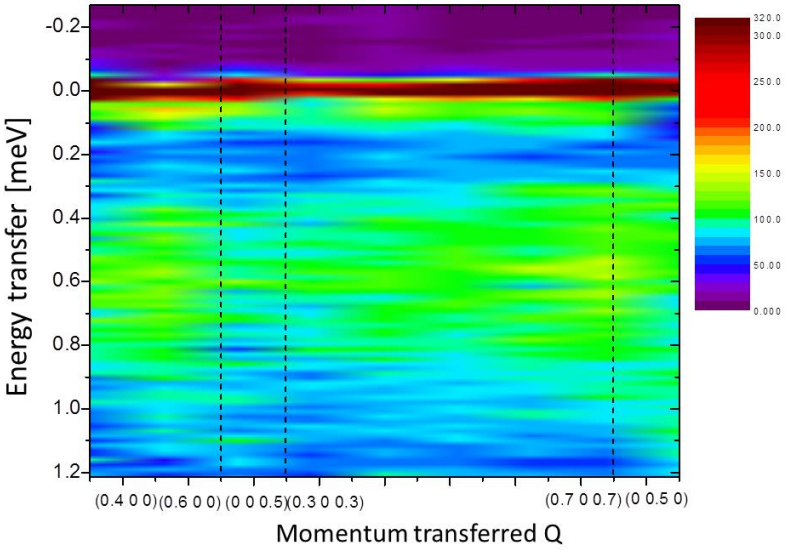

(a)

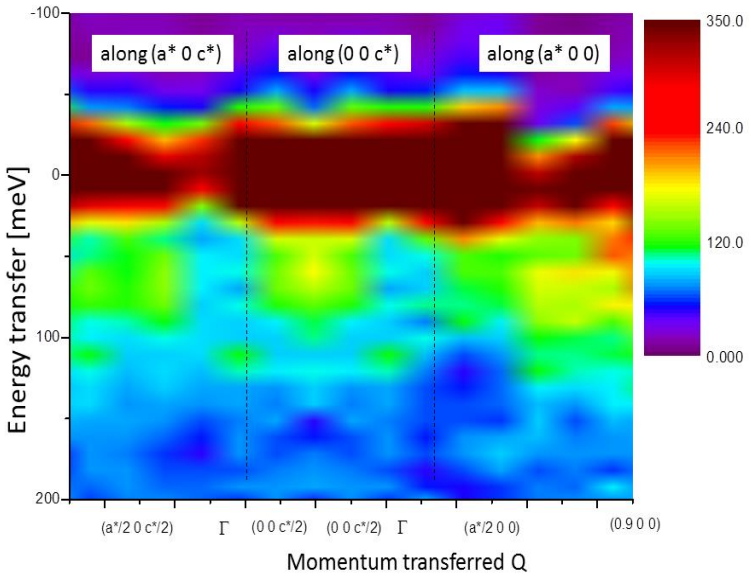

(b)

Figure 4.10 Image plots of RIXS spectra of $BaIrO_3$ at different momentum transfers, at T = 100K. (a) Energy excitations less than 1 eV. (b) Low energy excitation below 100 meV.

The excitations are weakly dispersing and are likely to be the transition between t_{2g} states across the Mott gap. Calculations considering both spin-orbital coupling and on-site Coulomb interactions U in (Ju *et al.*, 2013) show a 50-meV gap between J_{eff}= 1/2 LHB and J_{eff}= 1/2 UHB can be opened when U is set at 3eV, which is close to 70 meV observed. The high energy excitation ~0.6 eV is likely the transition from J_{eff}= 3/2 band to the empty J_{eff}= 1/2 UHB. The weakly dispersing Mott gap transition from J_{eff}= 1/2 LHB to J_{eff}= 1/2 UHB was similarly observed in Sr_2IrO_4 but with larger gap size (~0.5eV) (Ishii *et al.*, 2011c). Spin-orbital coupling is strongly proportional to the number of neighboring Ir atoms. The smaller band gap observed in $BaIrO_3$ is due to the quasi-1D structure, the number of neighboring Ir atoms in $BaIrO_3$ ($z \approx 2$) even less than that of Sr_2IrO_4 ($z \approx 4$), causing narrow bandwidth and thus band gap (Ju *et al.*, 2013).

CHAPTER 5

CONCLUSION AND FUTURE WORK

The work of this dissertation is the development of polarization analysis for hard resonant inelastic x-ray scattering which was carried out at the RIXS beamlines 9ID and 30ID at the APS. The analysis of the polarization of the scattered photon fills a technical void for hard RIXS spectrometers which currently can only measure the energy and momentum transfers. The outgoing polarization of the scattered photons provides symmetry information of the states involved in the scattering which is difficult to determine without polarization analysis. A polarization analyzer is designed to reflect the scattered photons from the main analyzer by about 90 degrees. At this reflecting angle, the in-plane polarization is naturally eliminated by the polarization factor so that the scattered photons perpendicular to the reflection plane are fully obtained. Therefore it can separate the two orthogonal polarizations (named 'π' and 'σ') by rotating the system by 90 degrees.

A polarization analysis system based on a graphite (0 0 6) polarization analyzer has been developed for Cu *K*-edge RIXS with about 1.4% overall efficiency and a factor of 0.3 energy resolution broadening which is a significant improvement of the only work of polarization analysis of hard RIXS utilized by flat graphite analyzer (Ishii *et al.*, 2011a). A preliminary polarization analyzed RIXS spectrum of $CuGeO_3$ carried out presents the potential of the polarization analysis. An improved polarization analyzer based on ultra-thin bent Si (4 4 4) is being developed for iridates at Ir L_3-edge. Although the overall efficiency is low, the bent Si polarization can detect the low energy excitation (below 1 eV) in the preliminary measurements with

Sr_2IrO_4.

For future work, more RIXS spectra need to be taken at various positions in the Brillouin zone to necessarily map the dispersion features of the excitation. More detailed analysis of the bent Si polarization analyzer needs to carry out to improve the optic with higher reflectivity. More polarization analyzers suitable for other transition metal edge will be developed and eventually available for various RIXS experiment as the main analyzer on the shelf.

Appendix

Permissions

Re: permission

From: "Jung Ho Kim" <jhkim@aps.anl.gov>

To: "Xuan Gao" <xuan.gao@wmich.edu>

No problem.

From: Xuan Gao <xuan.gao@wmich.edu>
Date: Friday, November 15, 2013 1:41 AM
To: Jung ho Kim <jhkim@aps.anl.gov>
Subject: permission

Hi Jungho,
May I ask for your permission in email for using the Fig 1 and Fig.3 in PRL 108, 117003, 2012 in my thesis?
Please response on Friday that I have to submit the thesis.

Thank you.

Xuan Gao

LICENSE #: 3270040345735 **Order Date:** 11/15/2013 View printable order	The European Physical Journal - Special Topics **Title:** X-ray polarization: General formalism and polarization analysis **Type of use:** Thesis/Dissertation	**Fee:** $0.00 USD
LICENSE #: 3270030823555 **Order Date:** 11/15/2013 View printable order	Solid State Communications **Title:** Effects of pressure on electrical property of BaIrO3 **Type of use:** reuse in a thesis/dissertation	**Fee:** $0.00 USD
LICENSE #: 3270030121324 **Order Date:** 11/15/2013 View printable order	Solid State Communications **Title:** Charge density wave formation accompanying ferromagnetic ordering in quasi-one-dimensional BaIrO3 **Type of use:** reuse in a thesis/dissertation	**Fee:** $0.00 USD

BIBLIOGRAPHY

Alloul H., *Introduction to the Physics of Electrons in Solids*. (Springer, 2011).

Ament L. J. P., G. Khaliullin, J. van den Brink, *Physical Review B* **84**, 020403 (2011a).

Ament L. J. P., M. van Veenendaal, T. P. Devereaux, J. P. Hill, J. van den Brink, *Reviews of Modern Physics* **83**, 705 (2011b).

Arkadiev V. A., A. A. Bjeoumikhov, M. Haschke, N. Langhoff, H. Legall, H. Stiel, R. Wedell, *Spectrochimica Acta Part B: Atomic Spectroscopy* **62**, 577 (2007).

Assoufid L., J. Qian, C. M. Kewish, C. Liu, R. Conley, A. T. Macrander, D. Lindley, C. Saxer. (2007), vol. 6704, pp. 670406-670406-11.

Beaurepaire E., H. Bulou, F. Scheurer, K. Jean-Paul, *Magnetism and Synchrotron Radiation*. Springer Proceedings in Physics (Springer, 2010).

Blasdell R. C., A. T. Macrander, *Review of Scientific Instruments* **66**, 2075 (1995).

Blume M., D. Gibbs, *Physical Review B* **37**, 1779 (1988).

Boseggia S., R. Springell, H. C. Walker, H. M. Rønnow, C. Rüegg, H. Okabe, M. Isobe, R. S. Perry, S. P. Collins, D. F. McMorrow, *Physical Review Letters* **110**, 117207 (2013).

Braicovich L., M. Moretti Sala, L. J. P. Ament, V. Bisogni, M. Minola, G. Balestrino, D. Di Castro, G. M. De Luca, M. Salluzzo, G. Ghiringhelli, J. van den Brink, *Physical Review B* **81**, 174533 (2010a).

Braicovich L., J. van den Brink, V. Bisogni, M. M. Sala, L. J. P. Ament, N. B. Brookes, G. M. De Luca, M. Salluzzo, T. Schmitt, V. N. Strocov, G. Ghiringhelli, *Physical Review Letters* **104**, 077002 (2010b).

Brink J. v. d., *EPL (Europhysics Letters)* **80**, 47003 (2007).

Caciuffo R., C. Ferrero, O. Francescangeli, S. Melone, *Review of Scientific Instruments* **61**, 3467 (1990).

Cao G., J. Bolivar, S. McCall, J. E. Crow, R. P. Guertin, *Physical Review B* **57**, R11039 (1998).

Cao G., J. Crow, R. Guertin, P. Henning, C. Homes, M. Strongin, D. Basov, E. Lochner, *Solid State Communications* **113**, 657 (2000).

Cetin M. F., "Light scattering in spin orbit coupling dominated systems". Theses and Dissertations, (2012).

Cheng J. G., J. S. Zhou, J. A. Alonso, J. B. Goodenough, Y. Sui, K. Matsubayashi, Y. Uwatoko, *Physical Review B* **80**, 104430 (2009).

Coldea R., S. M. Hayden, G. Aeppli, T. G. Perring, C. D. Frost, T. E. Mason, S. W. Cheong, Z. Fisk, *Physical Review Letters* **86**, 5377 (2001).

Collart E., A. Shukla, F. Gé é bart, M. Morand, C. Malgrange, N. Bardou, A. Madouri, J.-L. Pelouard, *Journal of Synchrotron Radiation* **12**, 473 (2005).

Crawford M. K., M. A. Subramanian, R. L. Harlow, J. A. Fernandez-Baca, Z. R. Wang, D. C. Johnston, *Physical Review B* **49**, 9198 (1994).

del Rio M. S., S. Bernstorff, A. Savoia, F. Cerrina, *Review of Scientific Instruments* **63**, 932 (1992).

Detlefs C., M. Sanchez del Rio, C. Mazzoli, *Eur. Phys. J. Spec. Top.* **208**, 359 (2012/06/01, 2012).

Elsa Abbena S. S., Alfred Gray, *Modern Differential Geometry of Curves and Surfaces with Mathematica*. (Chapman and Hall/CRC, ed. 3, 2006).

Engel T., P. Reid, *Physical Chemistry* (Pearson Benjamin-Cummings, 2006).

Erola E., V. Etelaniemi, P. Suortti, P. Pattison, W. Thomlinson, *Journal of Applied Crystallography* **23**, 35 (1990).

Gao X., C. Burns, D. Casa, M. Upton, T. Gog, J. Kim, C. Li, *Review of Scientific Instruments* **82**, 113108 (2011).

Ghiringhelli G., M. Matsubara, C. Dallera, F. Fracassi, R. Gusmeroli, A. Piazzalunga, A. Tagliaferri, N. B. Brookes, A. Kotani, L. Braicovich, *Journal of Physics: Condensed Matter* **17**, 5397 (2005).

Gog T., D. M. Casa, A. H. Said, M. H. Upton, J. Kim, I. Kuzmenko, X.

Huang, R. Khachatryan, *Journal of Synchrotron Radiation* **20**, 74 (2012).

Gog T., G. T. Seidler, D. M. Casa, M. H. Upton, J. Kim, S. Stoupin, K. P. Nagle, M. Balasubramanian, R. A. Gordon, T. T. Fister, S. M. Heald, T. Toellner, J. P. Hill, D. S. Coburn, Y.-J. Kim, A. H. Said, E. E. Alp, W. Sturhahn, H. Yavas, C. A. Burns, H. Sinn, *Synchrotron Radiation News* **22**, 12 (2009/11/30, 2009).

Grenier S., J. P. Hill, V. Kiryukhin, W. Ku, Y. J. Kim, K. J. Thomas, S. W. Cheong, Y. Tokura, Y. Tomioka, D. Casa, T. Gog, *Physical Review Letters* **94**, 047203 (2005).

Grigorieva I. G., A. A. Antonov, *X-Ray Spectrometry* **32**, 64 (2003).

Guarise M., B. Dalla Piazza, M. Moretti Sala, G. Ghiringhelli, L. Braicovich, H. Berger, J. N. Hancock, D. van der Marel, T. Schmitt, V. N. Strocov, L. J. P. Ament, J. van den Brink, P. H. Lin, P. Xu, H. M. Rønnow, M. Grioni, *Physical Review Letters* **105**, 157006 (2010).

Gulino A., R. G. Egdell, P. D. Battle, S. H. Kim, *Physical Review B* **51**, 6827 (1995).

Hannon J. P., G. T. Trammell, M. Blume, D. Gibbs, *Physical Review Letters* **61**, 1245 (1988).

Hartmann W., G. Markewitz, U. Rettenmaier, H. J. Queisser, *Applied Physics Letters* **27**, 308 (1975).

Haverkort M. W., *Physical Review Letters* **105**, 167404 (2010).

Hemenway P., *Divine Proportion: Φ Phi in Art, Nature, and Science.*, (Sterling Publishing Co., 2005).

Hirata Y., K. Ohgushi, J.-i. Yamaura, H. Ohsumi, S. Takeshita, M. Takata, T.-h. Arima, *Physical Review B* **87**, 161111 (2013).

Hubbard J., *Proceedings of the Royal Society of London. Series A. Mathematical and Physical Sciences* **281**, 401 (1964).

Huotari S., F. Albergamo, G. Vankó, R. Verbeni, G. Monaco, *Review of Scientific Instruments* **77**, 053102 (2006).

Huotari S., T. Pylkkänen, G. Vankó, R. Verbeni, P. Glatzel, G. Monaco,

Physical Review B **78**, 041102 (2008).

Huotari S., G. Vanko, F. Albergamo, C. Ponchut, H. Graafsma, C. Henriquet, R. Verbeni, G. Monaco, *Journal of Synchrotron Radiation* **12**, 467 (2005).

Ishihara S., S. Ihara, *Journal of Physics and Chemistry of Solids* **69**, 3184 (2008).

Ishii K., S. Ishihara, Y. Murakami, K. Ikeuchi, K. Kuzushita, T. Inami, K. Ohwada, M. Yoshida, I. Jarrige, N. Tatami, S. Niioka, D. Bizen, Y. Ando, J. Mizuki, S. Maekawa, Y. Endoh, *Physical Review B* **83**, 241101 (2011a).

Ishii K., S. Ishihara, Y. Murakami, K. Ikeuchi, K. Kuzushita, T. Inami, K. Ohwada, M. Yoshida, I. Jarrige, N. Tatami, S. Niioka, D. Bizen, Y. Ando, J. Mizuki, S. Maekawa, Y. Endoh, *Physical Review B* **83**, 241101 (2011b).

Ishii K., I. Jarrige, M. Yoshida, K. Ikeuchi, J. Mizuki, K. Ohashi, T. Takayama, J. Matsuno, H. Takagi, *Physical Review B* **83**, 115121 (2011c).

Jackeli G., G. Khaliullin, *Physical Review Letters* **102**, 017205 (2009).

Jahn H. A., E. Teller, *Proceedings of the Royal Society of London. Series A - Mathematical and Physical Sciences* **161**, 220 (July 15, 1937, 1937).

Jens Als-Nielsen D. M., *Elements of Modern X-ray Physics*. (Wiley, ed. 1, 2001).

Ju W., G.-Q. Liu, Z. Yang, *Physical Review B* **87**, 075112 (2013).

Kim B. J., H. Jin, S. J. Moon, J. Y. Kim, B. G. Park, C. S. Leem, J. Yu, T. W. Noh, C. Kim, S. J. Oh, J. H. Park, V. Durairaj, G. Cao, E. Rotenberg, *Physical Review Letters* **101**, 076402 (2008).

Kim B. J., H. Ohsumi, T. Komesu, S. Sakai, T. Morita, H. Takagi, T. Arima, *Science* **323**, 1329 (March 6, 2009, 2009).

Kim J., D. Casa, M. H. Upton, T. Gog, Y.-J. Kim, J. F. Mitchell, M. van Veenendaal, M. Daghofer, J. van den Brink, G. Khaliullin, B. J. Kim, *Physical Review Letters* **108**, (2012a).

Kim J., D. Casa, M. H. Upton, T. Gog, Y.-J. Kim, J. F. Mitchell, M. van Veenendaal, M. Daghofer, J. van den Brink, G. Khaliullin, B. J. Kim, *Physical Review Letters* **108**, 117003 (2012b).

Kim Y.-J., J. P. Hill, H. Benthien, F. H. L. Essler, E. Jeckelmann, H. S. Choi, T. W. Noh, N. Motoyama, K. M. Kojima, S. Uchida, D. Casa, T. Gog, *Physical Review Letters* **92**, 137402 (2004a).

Kim Y.-J., J. P. Hill, F. C. Chou, D. Casa, T. Gog, C. T. Venkataraman, *Physical Review B* **69**, 155105 (2004b).

Kim Y.-J., J. P. Hill, J. Kim, D. Casa, *Synchrotron Radiation News* **25**, 3 (2012/07/30, 2012c).

Korneta O. B., "A systematic study of transport, magnetic and thermal properties of layered iridates". Theses and Dissertations, (2012).

Korneta O. B., T. Qi, S. Chikara, S. Parkin, L. E. De Long, P. Schlottmann, G. Cao, *Physical Review B* **82**, 115117 (2010).

Kramers H. A., W. Heisenberg, *Z. Physik* **31**, 681 (1925).

Krisch M., A. Freund, G. Marot, L. Zhang, *Nuclear Instruments and Methods in Physics Research Section A: Accelerators, Spectrometers, Detectors and Associated Equipment* **308**, 378 (1991).

Laguna-Marco M. A., D. Haskel, N. Souza-Neto, J. C. Lang, V. V. Krishnamurthy, S. Chikara, G. Cao, M. van Veenendaal, *Physical Review Letters* **105**, 216407 (2010).

Lang J. C., G. Srajer, *Rev. Sci. Instrum.* **66**, 1540 (1995).

Li C., K. C. K. Soh, P. Wu, *Journal of Alloys and Compounds* **372**, 40 (2004).

Luo J., G. Trammell, J. Hannon, *Physical Review Letters* **71**, 287 (1993).

Maiti K., *Physical Review B* **73**, 115119 (2006).

Maiti K., R. S. Singh, V. R. R. Medicherla, S. Rayaprol, E. V. Sampathkumaran, *Physical Review Letters* **95**, 016404 (2005).

Miessler G. L., D. A. Tarr, *Inorganic Chemistry*. (Prentice-Hall, ed. 2nd, 1999).

Moon S. J., H. Jin, W. S. Choi, J. S. Lee, S. S. A. Seo, J. Yu, G. Cao, T. W. Noh, Y. S. Lee, *Physical Review B* **80**, 195110 (2009).

Plakida N. M., *Spectroscopy of High-Tc Superconductors: A Theoretical View*. (CRC Press, 2003).

Powell A. V., P. D. Battle, *Journal of Alloys and Compounds* **191**, 313 (1993a).

Powell A. V., P. D. Battle, *Journal of Alloys and Compounds* **191**, 313 (1993b).

Rio M. S. d., A. Y. Faenov, V. M. Dyakin, T. A. Pikuz, S. A. Pikuz, V. M. Romanova, T. A. Shelkovenko, *Physica Scripta* **55**, 735 (1997).

Rueff J.-P., A. Shukla, *Reviews of Modern Physics* **82**, 847 (2010).

Rueff J. P., in *Magnetism and Synchrotron Radiation*, E. Beaurepaire, H. Bulou, F. Scheurer, K. Jean-Paul, Eds. (Springer Berlin Heidelberg, 2010), vol. 133, pp. 263-277.

Saitoh E., S. Okamoto, K. T. Takahashi, K. Tobe, K. Yamamoto, T. Kimura, S. Ishihara, S. Maekawa, Y. Tokura, *Nature* **410**, 180 (2001).

Sanchez del Rio M., N. Canestrari, F. Jiang, F. Cerrina, *Journal of Synchrotron Radiation* **18**, 708 (2011).

Sanchez del Rio M., R. J. Dejus, in *Proc. SPIE* (2004), vol. 5536, pp. 171-174.

Sanchez del Rio M., C. Ferrero, V. Mocella. (1997), vol. 3151, pp. 312-323.

Schülke W., *Electron Dynamics by Inelastic X-Ray Scattering*. Oxford Series on Synchrotron Radiation (Oxford University Press, USA, 2007).

Schiff L., H. Snyder, *Physical Review* **55**, 59 (1939).

Schlappa J., T. Schmitt, F. Vernay, V. N. Strocov, V. Ilakovac, B. Thielemann, H. M. Rønnow, S. Vanishri, A. Piazzalunga, X. Wang, L. Braicovich, G. Ghiringhelli, C. Marin, J. Mesot, B. Delley, L. Patthey, *Physical Review Letters* **103**, 047401 (2009).

Schwuttke G. H., J. K. Howard, *Journal of Applied Physics* **39**, 1581 (1968).

Shen Q., K. D. Finkelstein, *Review of Scientific Instruments* **64**, 3451 (1993).

Siegrist T., B. L. Chamberland, *Journal of the Less Common Metals* **170**, 93 (1991).

Sinars D. B., G. R. Bennett, D. F. Wenger, M. E. Cuneo, J. L. Porter, *Appl. Opt.* **42**, 4059 (2003).

Suga S., S. Imada, A. Higashiya, A. Shigemoto, S. Kasai, M. Sing, H. Fujiwara, A. Sekiyama, A. Yamasaki, C. Kim, T. Nomura, J. Igarashi, M. Yabashi, T. Ishikawa, *Physical Review B* **72**, 081101 (2005).

Suortti P., P. Pattison, W. Weyrich, *Journal of Applied Crystallography* **19**, 336 (1986a).

Suortti P., P. Pattison, W. Weyrich, *Journal of Applied Crystallography* **19**, 343 (1986b).

Sutter J. P., T. Connolley, T. P. Hill, H. Huang, D. W. Sharp, M. Drakopoulos, *Journal of Synchrotron Radiation* **15**, 584 (2008).

Takagi S., *J. Phys. Soc. Jpn.* **26**, 1239 (1969).

Taupin D., *Bull. Soc. Fr. Mineral. Crystallogr.* **87**, 469 (1964).

Tchen T., *Tech. Phys. Lett.* **29**, 235 (2003/03/01, 2003).

Tokura Y., N. Nagaosa, *Science* **288**, 462 (April 21, 2000, 2000).

Tuffanelli A., M. Sanchez del Rio, G. Pareschi, M. Gambaccini, A. Taibi, A. Fantini, M. Ohler, in *Proc. SPIE*. (1999), vol. 3773, pp. 192-198.

van Veenendaal M., *Physical Review Letters* **96**, 117404 (2006).

Verbeni R., M. Kocsis, S. Huotari, M. Krisch, G. Monaco, F. Sette, G. Vanko, *Journal of Physics and Chemistry of Solids* **66**, 2299 (2005).

W. H. Zachariasen, *Theory of X-ray Diffraction in Crystals*. (Dover, New York, 1967).

Wakimoto S., H. Kimura, K. Ishii, K. Ikeuchi, T. Adachi, M. Fujita, K. Kakurai, Y. Koike, J. Mizuki, Y. Noda, K. Yamada, A. H. Said, Y. Shvyd'ko, *Physical Review Letters* **102**, 157001 (2009).

Wang F., T. Senthil, *Physical Review Letters* **106**, 136402 (2011).

Weber F., S. Rosenkranz, J. P. Castellan, R. Osborn, J. F. Mitchell, H. Zheng, D. Casa, J. H. Kim, T. Gog, *Physical Review B* **82**, 085105 (2010).

Whangbo M. H., H. J. Koo, *Solid State Communications* **118**, 491 (2001).

White J. E., *Journal of Applied Physics* **21**, 855 (1950).

Wittry D. B., W. Z. Chang, R. Y. Li, *J. Appl. Phys.* **74**, 3534 (1993).

Wittry D. B., S. Sun, *J. Appl. Phys.* **68**, 387 (1990).

Wolfgang Nolting, A. Ramakanth, *Quantum Theory of Magnetism*. (Springer, 2010).

Wolfram, *Mathematica, Version 7.0.1*. (Wolfram Research Inc., Champaign, IL, USA, 2009).

Zaanen J., G. A. Sawatzky, J. W. Allen, *Physical Review Letters* **55**, 418 (1985).

Zhao J., L. Yang, K. Mydeen, F. Li, R. Yu, C. Jin, *Solid State Communications* **148**, 361 (2008).